Finite-element modelling based on optical coherence tomography and corresponding X-ray microCT data for normal and pathological middle ears

Graduate Program in Biological and Biomedical Engineering

McGill University, Montréal

December 2023

A thesis submitted to McGill University
in partial fulfillment of the requirements of the degree of
Doctor of Philosophy

To my mother Mahbubeh

and my father Bahram

for fostering a love for exploring within me

Table of contents

List of figures

List of tables

List of abbreviations

ABG	Air-bone gap
AML	Anterior mallear ligament
APT	Anterior pars tensa
FE	Finite-element
FPS	Frames per second
IMJ	Incudomallear joint
ISJ	Incudostapedial joint
LDV	Laser Doppler vibrography
MRM	Magnetic resonance microscopy
OCT	Optical coherence tomography
OCT-DV	OCT Doppler vibrometry
OPFOS	Orthogonal-plane fluorescence optical sectioning
PF	Pars flaccida
PIL	Posterior incudal ligament
PPT	Posterior pars tensa
PT	Pars tensa
ROC	Receiver operating characteristic
SAL	Stapedial annular ligament
TM	Tympanic membrane
TMMC	TM-malleus connection

Abstract

Optical coherence tomography (OCT) vibrometry is a noninvasive tool which can be employed *in vivo* for functional imaging of the middle ear. It provides spatially resolved vibrational responses and also anatomical images of the same ear. Our objective here was to explore the application of finite-element (FE) modelling to OCT data in normal and pathological middle ears.

We used OCT vibration measurements for three human cadaver middle ears and X-ray microCT images from the same ears to build three distinct FE models. The material properties and boundary conditions of the models were obtained from previously reported studies.

The FE model displacements were compared with OCT measurements and with the literature in terms of tympanic-membrane (TM) vibration patterns and also the frequency responses at several locations in the middle ear. The simulated TM displacement patterns were qualitatively similar to the OCT results. The three models were compared with each other in terms of geometry and function. Parameter sensitivity analyses were done and the results were compared among the models and with the literature.

We then built FE models of pathological ears and generated large amounts of normal and pathological synthetic data. We were able to classify the simulated data into normal and pathological groups based on features extracted from simulated vibration magnitudes, using the ratio of the vibration magnitude at the incus to that at the umbo at different frequencies in a decision tree. The sensitivities and specificities of the classifications were all greater than 0.88. For less extreme simulated pathologies, the sensitivities were higher while the specificities were lower.

This study provided an initial look at the combined use of OCT measurements and FE modelling based on subject-specific anatomy. The geometries and parameters of the existing FE models could be modified for individual patients in the future to help identify abnormalities in the middle ear. The results suggest that the vibration measurements within the middle ear that can be provided by OCT (e.g., at the incus) will be very valuable for diagnosis.

Résumé

La vibrométrie par tomographie par cohérence optique (TCO) est un outil non invasif qui peut être utilisé *in vivo* pour l'imagerie fonctionnelle de l'oreille moyenne. Elle fournit des réponses vibratoires spatialement résolues ainsi que des images anatomiques de la même oreille. Notre objectif ici était d'explorer l'application de la modélisation par éléments finis (EF) aux données TCO dans l'oreille moyenne normale et pathologique.

Nous avons utilisé des mesures de vibration TCO pour trois oreilles moyennes de cadavres humains et des images microCT à rayons X de ces mêmes oreilles pour construire trois modèles à EF distincts. Les propriétés des matériaux et les conditions limites des modèles ont été obtenues à partir d'études antérieures.

Les déplacements des modèles à EF ont été comparés aux mesures TCO et à la littérature en termes de modes de vibration de la membrane tympanique (MT) et de réponses en fréquence à plusieurs endroits de l'oreille moyenne. Les modes de déplacement simulés de la membrane tympanique étaient qualitativement similaires aux résultats de la TCO . Les trois modèles ont été comparés entre eux en termes de géométrie et de fonction. Des analyses de sensibilité des paramètres ont été effectuées et les résultats ont été comparés entre les modèles et avec la littérature.

Nous avons ensuite construit des modèles à EF d'oreilles pathologiques et généré de grandes quantités de données synthétiques normales et pathologiques. Nous avons pu classer les données simulées en groupes normaux et pathologiques sur la base de caractéristiques extraites des amplitudes vibratoires simulées, en utilisant le rapport de l'amplitude vibratoire à l'incus sur celle à l'umbo à différentes fréquences dans un arbre de décision. Les sensibilités et les

spécificités des classifications étaient toutes supérieures à 0,88. Pour les pathologies simulées moins extrêmes, les sensibilités étaient plus élevées alors que les spécificités étaient plus faibles.

Cette étude a fourni un premier aperçu de l'utilisation combinée des mesures TCO et de la modélisation par EF basée sur l'anatomie spécifique du sujet. Les géométries et les paramètres des modèles à EF existants pourraient être modifiés à l'avenir pour des patients individuels afin d'aider à identifier les anomalies de l'oreille moyenne. Les résultats suggèrent que les mesures de vibration dans l'oreille moyenne qui peuvent être fournies par la TCO (par exemple, au niveau de l'incus) seront très utiles pour le diagnostic.

Acknowledgements

I would like to take this opportunity to express my deepest gratitude and appreciation to all those who have supported and guided me throughout my doctoral research journey. Their invaluable contributions have played a significant role in shaping this thesis and my personal growth as a researcher.

First and foremost, I am profoundly grateful to my supervisor, Dr W. Robert J. Funnell, for his unwavering support, expertise, and mentorship. His guidance, patience and insightful feedback have been instrumental in the successful completion of this research. I am truly fortunate to have had the opportunity to work under his supervision.

I am also indebted to the members of my thesis committee, Dr Sylvain Baillet and Dr Ahmad Haidar. Their expertise, constructive criticism, and valuable suggestions have immensely contributed to the refinement and improvement of this work. I am grateful for their time, commitment, and willingness to share their knowledge.

I express my gratitude to Dr Robert Adamson, Dan MacDougall, Joshua Farrell and Thomas Landry, our collaborators from Dalhousie University, for providing invaluable data resources.

I extend my sincere appreciation to the staff and faculty at McGill University, who provided a supportive academic environment and valuable resources throughout my doctoral studies. Their dedication to education and research has played a crucial role in my intellectual development.

I would like to express my gratitude to my colleagues and fellow researchers at AudiLab, Dr Hamid Motallebzadeh, Orhun Kose and Xuan Wang, for their academic mentorship, stimulating discussions, and collaborative efforts. Their insights and assistance have significantly enriched my research experience.

Furthermore, I am deeply thankful to my friends and family for their constant support, understanding and encouragement. Their love, patience, and belief in my abilities have been a source of motivation.

Lastly, I would like to acknowledge the financial support provided by the Canadian Institutes of Health Research, the Natural Sciences and Engineering Research Council of Canada, and the Faculty of Medicine and Health Sciences of McGill University. Their funding has not only facilitated my research but also allowed me to attend conferences, workshops, and training programs that broadened my knowledge and network.

Original contributions

1. For the first time, finite-element models of multiple human middle ears were built based on geometries obtained from microCT images and then simulation results were compared with optical coherence tomography (OCT) vibration measurements in the same ears (Chapter 4). The major findings were that the simulated tympanic-membrane (TM) vibration patterns were qualitatively similar to the OCT measurement data; the frequency responses were qualitatively similar to data from the literature for frequencies up to 3 kHz; the frequency responses for the models from the two ears of the same individual were more similar to each other than to those of the third ear; and the results of the parameter sensitivity analysis were similar across all three ears, except for one ear in which the stapes had a different orientation. Variations in the Young's modulus of the incudomallear joint (IMJ) had small effects on the model behaviour up to 2 kHz. Unrealistically low values of viscous cochlear damping increased the number of resonances seen on the TM, umbo and stapes, presumably corresponding to individual substructure resonances that are normally hidden.

2. Large sets of synthetic data for models of normal ears and pathological ears (stapes fixation, IMJ disarticulation and incudostapedial joint (ISJ) disarticulation) were created, with inter-ear variability incorporated by changing the model parameters randomly (Chapter 5). The major finding was that the changes due to the simulated pathologies were in qualitative agreement with experimental laser Doppler vibrometry measurements from normal subjects and patients.

3. A decision tree was designed. It could distinguish among normal ears, IMJ disarticulation, ISJ disarticulation and stapes fixation, with sensitivities and specificities greater than 0.78.

Two partial pathologies were also simulated and in both cases the specificity of the decision tree decreased while the sensitivity increased.

4. Our results suggest that the vibration measurements within the middle ear that can be provided by OCT (e.g., at the incus) may be very valuable for diagnosis, and that umbo and incus vibrations should be measured at both low and high frequencies (e.g., 500 Hz and 3 kHz) in order to distinguish among the disorders considered here.

Contributions of authors

Chapter 4. Finite-element modelling based on optical coherence tomography and corresponding X-ray microCT data for three human middle ears

Journal of the Association for Research in Otolaryngology 24(3): 339–363 (2023)

First author: Marzieh Golabbakhsh
Built models, analyzed and interpreted the results; wrote the manuscript

Second author: Xuan Wang
Built one model, interpreted preliminary results

Third author: Dan MacDougall
Was involved in designing the experimental protocol and the setup

Fourth author: Joshua Farrell
Was involved in design implementation and validation of data

Fifth author: Thomas Landry
Guided the experimental design

Sixth author: W. Robert J. Funnell
Conceived the modelling study, supervised the research and writing

Seventh author: Robert Adamson
Conceived the experimental study, provided the experimental data, provided comments and suggestions, reviewed the manuscripts

Chapter 5. Use of simulated data to explore the application of optical coherence tomography for classifying middle-ear pathologies

Journal of the Acoustical Society of America 154 (5): 2790–2799 (2023)

First author: Marzieh Golabbakhsh
Designed the study, analyzed and interpreted the results; wrote the manuscript

Second author: W. Robert J. Funnell
Supervised the research and writing

Chapter 1. Introduction

Hearing loss is very prevalent, affecting more than 1.5 billion people globally, including almost two thirds of persons over the age of sixty (World Health Organization 2021). Unaddressed hearing loss has many negative effects, and leads to high costs for health-care systems. With the aging population, the number of hearing-impairment diagnoses is also quickly rising.

Hearing loss can be sensorineural, affecting the inner ear, auditory nerve and brain; or conductive, affecting the outer and/or middle ear; or a combination of the two types. Optical coherence tomography (OCT) vibrometry is a non-invasive means of obtaining spatially resolved vibrational responses and also anatomical images. It can be used *in vivo* and provides vibration measurements beyond the tympanic membrane (TM), including at the incus. Such information can potentially improve diagnostic sensitivity and specificity as compared to other available methods.

Computational models, such as finite-element (FE) models, have been widely used to study middle-ear mechanics. The purpose here is to explore the application of FE modelling to OCT data.

The first objective of this work was to generate FE models based on geometries obtained from microCT images of multiple normal middle ears and validate them against OCT vibration measurements in the same ears. The second objective was to use one of those models to explore the feasibility of using OCT vibration measurements at the umbo and incus to distinguish among various disorders.

The anatomy of the middle ear and the fundamentals of middle-ear mechanics are reviewed in Chapter 2. Chapter 3 then provides a brief introduction to the FE method and to OCT

measurement, along with a review of previous middle-ear models and experimental measurements. Chapter 4 presents FE modelling of three human middle ears based on OCT and corresponding microCT images. Chapter 5 presents the use of simulated data to explore the application of optical coherence tomography for classifying middle-ear pathologies. Chapter 6 includes a summary of our results and original contributions, as well as discussions of possible future directions and of the significance of the work.

Chapter 2. Anatomy and mechanics of the human middle ear

2.1 Introduction

The human ear has three parts, the outer ear, middle ear and inner ear. The outer ear includes the pinna (or auricle), concha, and external auditory canal. The middle ear includes the TM plus three ossicles (malleus, incus and stapes) and their ligaments, all housed in a cavity filled with air. The TM separates the outer ear from the middle ear. The middle ear conducts sound waves into the inner ear through the TM and ossicles. The inner ear is filled with liquid and is connected to the middle ear via two openings, the oval window and round window. It includes the vestibule, cochlea and semicircular canals, seen in Figure 2.1. It converts the mechanical vibrations into electrical signals.

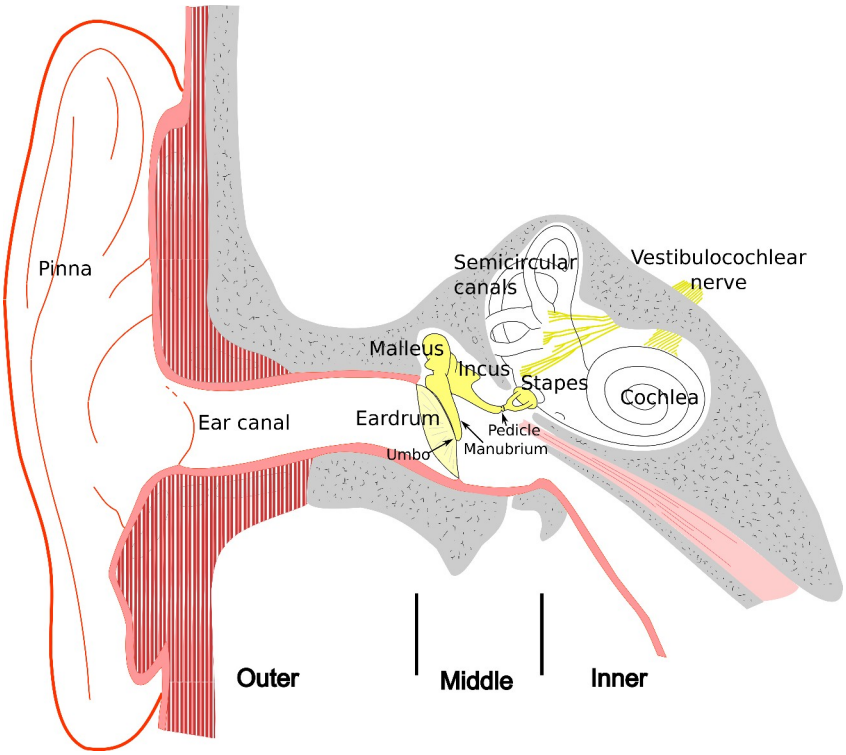

Figure 2.1. Schematic diagram of the human ear, including the outer, middle and inner ear (After http://audilab.bme.mcgill.ca/teach/me_saf/)

Since our project is focused on the middle ear, in section 2.2 human middle-ear anatomy is presented briefly. In section 2.3 a brief review of some aspects of middle-ear mechanics will be presented. As we are focused on OCT measurements in this thesis, a review of OCT measurements of the human middle ear will be given in section 2.4

2.2 Anatomy

2.2.1 Tympanic membrane

The TM is a thin cone-shaped structure with its apex pointing inwards. Figure 2.2 shows the shape of the TM. The apex of the cone is called the umbo and is where the tip of the manubrium is located. The whole length of the manubrium is visible through the TM and the TM-malleus connection (TMMC) runs along the entire length of the manubrium. The manubrium is firmly attached to the TM at the lateral

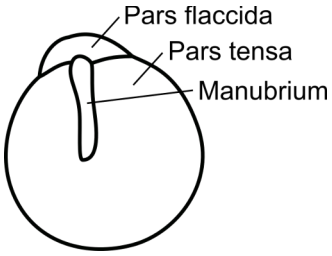

Figure 2.2. Anatomy of TM (http://audilab.bme.mcgill.ca/teach/me_saf/)

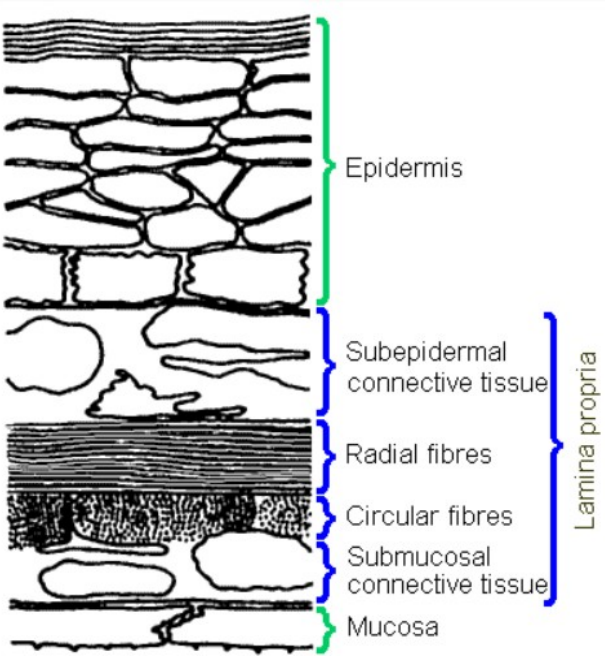

Figure 2.3. Layers of TM (http://audilab.bme.mcgill.ca/teach/me_saf/)

process and at the umbo with fibrous tissue, but between those locations it is more separate from the TM (Graham et al. 1978). The width and thickness of the TMMC vary among individuals by almost an order of magnitude (De Greef et al. 2017). The tympanic membrane is divided into a larger pars tensa below and a triangular smaller pars flaccida. The periphery of the pars tensa is thickened (forming the fibrocartilaginous ring) and anchors the tympanic membrane to a groove called the tympanic sulcus.

The pars flaccida is thicker than the pars tensa. They both consist of a lateral epidermal layer, a medial mucosal layer, and an intermediate fibrous layer which is called the lamina propria. The fibrous layer is made up of four layers, subepidermal connective tissue, radial fibres, circular fibres and submucosal connective tissue (Figure 2.3). The stiffness of the TM is mainly due to these radial and circular fibres.

2.2.2 Ossicles

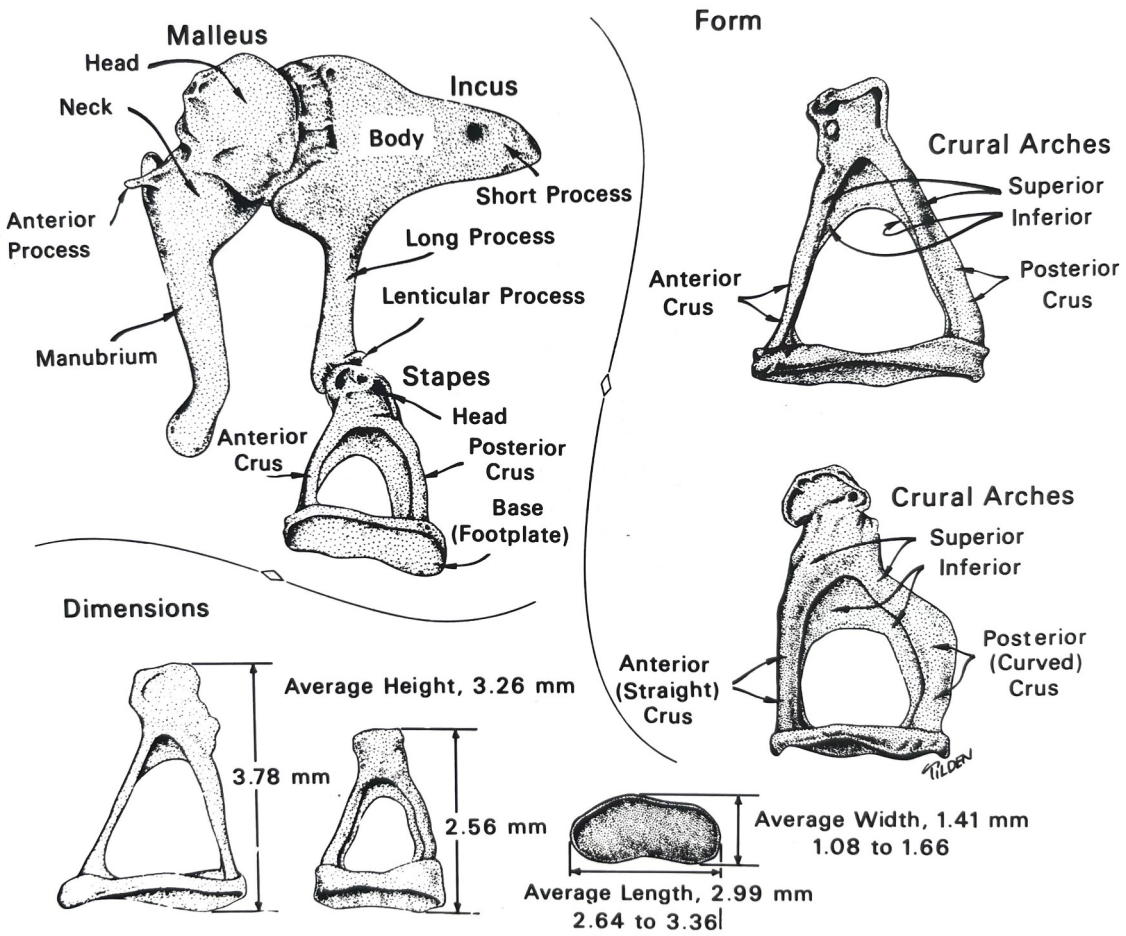

Figure 2.4. Sketch of ossicles and form and dimensions of the stapes (Gulya and Schuknecht 1994)

The middle-ear ossicles are the smallest bones in the human body. They include the malleus, incus and stapes (Figure 2.4). The malleus (Latin for “hammer”, because of its shape) is the most lateral bone of the ossicular chain. It consists of a head, neck, lateral process, anterior process, and manubrium. It is connected to the TM along the lateral side of the manubrium by the TMMC. The malleus head is connected to the incus body by the incudomallear joint.

The second bone in the ossicular chain is the incus (Latin for “anvil”, because of its relationship to the malleus) which is situated between the malleus and stapes. It articulates through two synovial joints known as the incudomallear and incudostapedial joints, respectively. The incus

consists of a body and the short, long, and lenticular processes. The lenticular process is located at the end of the long process and is composed of a very thin pedicle and the lenticular plate (e.g. Funnell et al. 2005). The short process is attached to the posterior wall by the posterior incudal ligament.

The stapes (Latin for “stirrup”, for its shape) is the most medial bone of the ossicular chain. It includes a head, two crura (anterior crus and posterior crus) and a footplate. The head is connected to the lenticular plate of the incus by the incudostapedial joint, while the footplate is attached to the oval window by an annular ligament. The anterior crus is in general straighter than the posterior crus, but both vary in shape and size among individuals. Likewise, various thicknesses, shapes and curvatures have been observed for the footplate (Gulya and Schuknecht 1994, page 50)

2.2.3 Ossicular joints

The incudomallear and incudostapedial joints of the middle ear both have a capsule composed of ligamentous fibers and are filled with synovial fluid. The capsule wraps around the ends of the bones, and joins the periosteum of each bone to that of the other (Gulya and Schuknecht 1994, page 71).

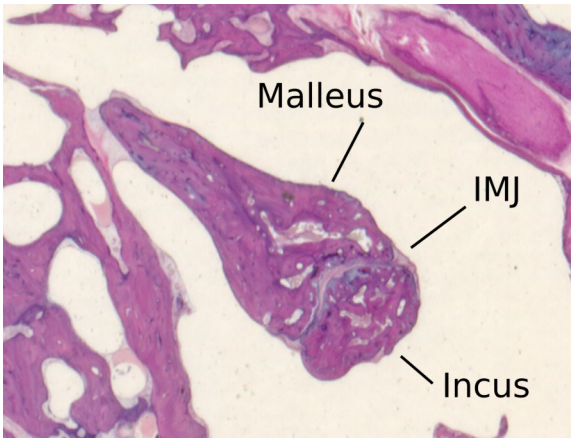

Figure 2.5. Incudomallear joint (IMJ) (Courtesy of Y. Clermont)

The incudomallear joint is generally described as saddle-shaped and (Wolff and Bellucci 1956) note that the opposing joint surfaces present jaw-like appearances in vertical sections (Gulya and Schuknecht 1994).

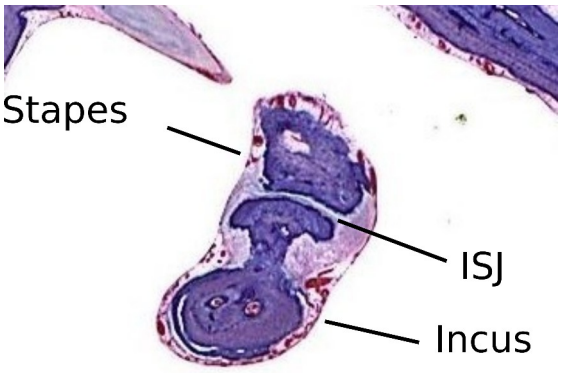

Figure 2.6. Incudostapedial joint (ISJ)
(Courtesy of C. Northrop)

The incudostapedial joint connects the slightly convex lenticular process of the incus with the slightly concave surface of the head of the stapes. It represents the place where the rotational motions of the malleus and incus are converted into the translational motion of the stapes (Gulya and Schuknecht 1994).

2.2.4 Ligaments

Five ligaments help to hold the malleus in place. The anterior suspensory ligament connects the head of the malleus to the anterior wall of the epitympanom; the lateral suspensory ligament connects the neck of the malleus to the tympanic cavity wall; and the superior suspensory ligament (not recognized as a ligament by all authors) connects the head of the malleus to the epitympanum wall. The anterior mallear ligament (AML), which connects the anterior process of the malleus to the petrotympanic fissure, is in the classical axis of ossicular rotation. The posterior mallear ligament connects the neck of the malleus to the pretympanic spine.(Gulya and Schuknecht 1994, page 56).

The posterior incudal ligament (PIL) anchors the short process and is in the classic axis of rotation. It consists of two portions, anterior and posterior (Wolff and Bellucci 1956).The stapedial annular ligament (SAL) is located between the boundary of the oval window and the stapes footplate. The SAL provides a sealed but mobile boundary for transmitting ossicular

movement into the cochlear liquid (Wolff and Bellucci 1956). Transmission electron microscopy has shown that the SAL consists of thinner transverse micro-fibrils and thicker elastic fibers (Ohashi et al. 2006).

2.2.5 Muscles

The stapedius muscle lies in the posterior wall of the tympanic cavity and is connected to the head and/or posterior crus of the stapes (Anson and Donaldson 1981). Its contraction tilts the stapes footplate and causes stretching of the annular ligament, to reduce the response of the middle ear to acoustic stimulation. This muscle is innervated from the facial nerve and its fibres converge into a tendon connected to the tympanic cavity wall.

The tensor tympani muscle is about 2 cm in length and is surrounded by a bony sheath. Its fibres converge and eventually form the tendons of the muscle. When the tensor tympani muscle functions, it draws the manubrium medially to make the tympanic membrane tenser (Gulya and Schuknecht 1994).

These two muscles act together to modify the motions of the ossicular chain.

2.2.6 Middle-ear air spaces

The tympanic cavity is a division of the middle-ear air spaces that measures about 15 mm in the vertical and anteroposterior dimensions, while in its transverse dimension it spreads out superiorly to 6 mm and inferiorly to 4 mm from a central bottleneck of 2 mm (Gulya and Schuknecht 1994, Fig 3-82). This cavity has three parts: (1) the mesotympanum, the area located medial to the tympanic membrane and the bony tympanic annulus; (2) the epitympanum, the area which lies superior to the tympanic membrane and houses the head of the malleus as well as the body and short process of the incus; and (3) the hypotympanum, the part located inferior to the lowest part of the tympanic annulus (Figure 2.7). The tympanic cavity is connected to the

nasopharynx via the Eustachian tube, which keeps it ventilated, and to the mastoid air cells posteriorly via the mastoid antrum. The tympanic cavity contains the ossicular chain and its walls are lined by mucous membrane.

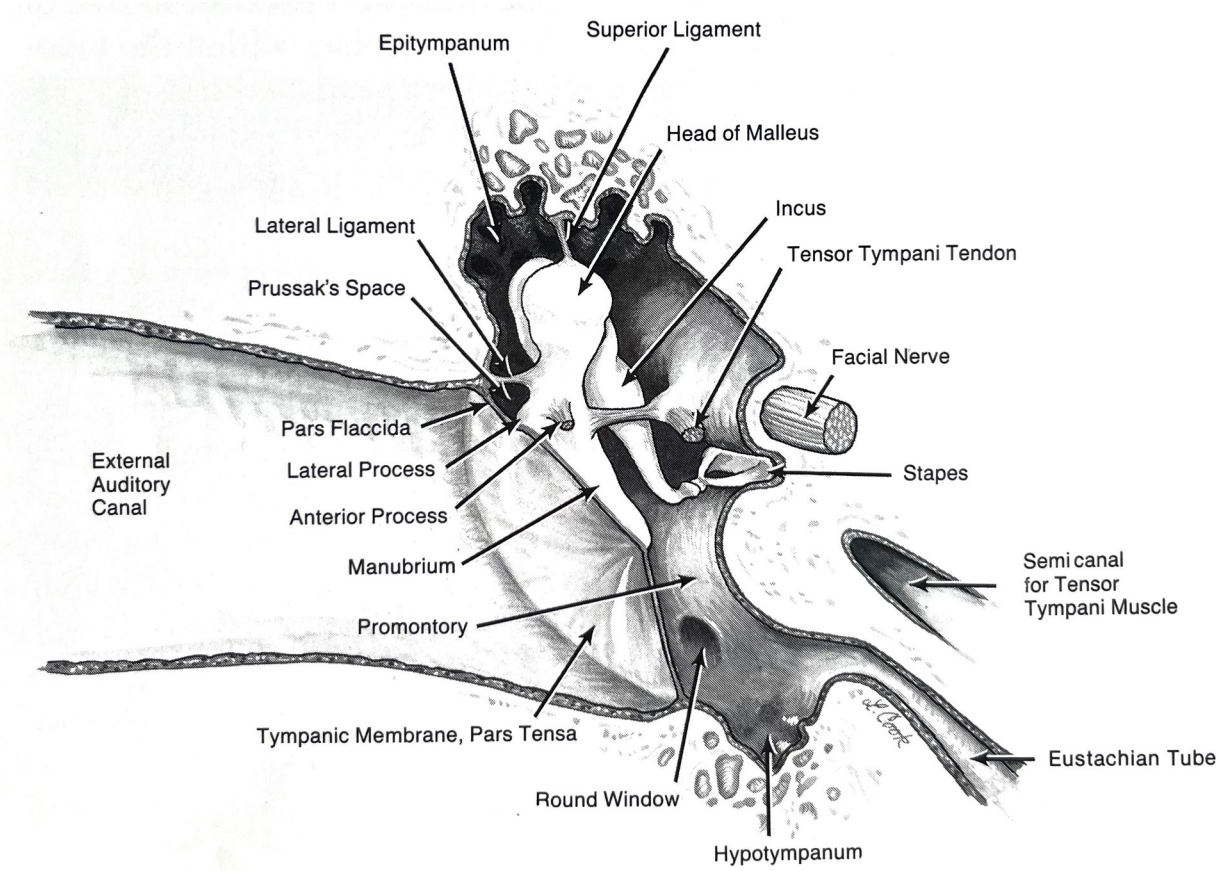

Figure 2.7. Middle-ear cavity, with the epitympanum and hypotympanum labelled (Anson and Donaldson 1981)

The compliance of an enclosed volume of air is proportional to its volume, and the volume of air trapped in the middle-ear cavity has a large impact on the input admittance of the middle ear (e.g., Funnell and Laszlo 1978; Stepp and Voss 2005). Some groups have considered this effect in their finite-element models (e.g. Gan et al. 2004). There is great variability in the volume in different ears (e.g., values between 0.4 and 1.24 cm^3 in Stepp and Voss 2005).

2.3 Mechanics

In this section we will introduce the mechanics of sound transmission through the middle ear. First we will define the concepts of a transformer mechanism in section 2.3.1 and of cochlear impedance in section 2.3.2. Then we will talk about measurements of vibrations of the TM in section 2.3.3 and of the ossicles in section 2.3.4.

2.3.1 Transformer mechanism

An important function of the middle ear is to work as an impedance-matching transformer between the low-impedance air in the outer ear and the high-impedance liquid in the inner ear. This transformation is considered to be implemented in three ways: (1) the ratio of the TM surface area to that of the stapes footplate; (2) the ratio of the lever arm of the manubrium to that of the long process of the incus; and (3) the eardrum's curvature.

1) The surface area of the TM is larger than that of the footplate. Therefore the pressure at the footplate will be greater in proportion to the ratio of the effective areas of the TM and footplate. The TM and stapes areas have been estimated to be 55 mm^2 and 3.2 mm^2 respectively (Wever and Lawrence 1954), so the pressure would become larger by a factor of about 17. However, this factor is valid only with the assumptions that the TM vibrates as a stiff surface about a fixed hinge, and that the stapes behaviour is piston-like (Békésy 1941).

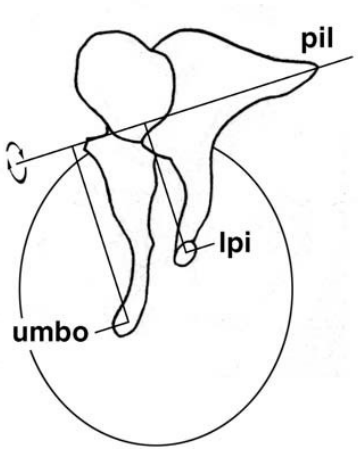

Figure 2.8. Rotation axis and lever arms of the ossicular lever (After Dahmann, 1930)

2) Assuming a fixed axis of rotation for the ossicles which runs through the anterior process of the malleus and the posterior incudal ligament, an ossicular-lever mechanism can be defined. The lever ratio then will be the length of the malleus (perpendicularly from the axis of rotation to the umbo) divided by the

length of the incus (perpendicularly from the axis of rotation to the tip of the long process of the incus). This ratio is reported to be approximately 1.3 (Wever and Lawrence 1954, p. 95).

3) The effect of TM curvature on the transformation mechanism was first noted in 1869 by Helmholtz: “Helmholtz thought of the eardrum as a membrane whose curvature, in the absence of significant inherent bending stiffness, would be determined purely by the interaction of the tension with the three-dimensional geometry and with the longitudinal stiffnesses of the membrane’s fibers” (Funnell 1996). The concept was later supported by Tonndorf and Khanna (1972). Funnell (1996) did finite-element simulations and concluded that some regions of the TM have enhanced coupling to the manubrium which is related to the TM curvature.

It may be helpful to think in terms of the three different mechanisms mentioned above, but it is difficult to meaningfully separate the middle-ear behaviour into these distinct mechanisms (Funnell 1996).

2.3.2 Cochlear impedance

An important variable in our understanding of sound-energy transfer through the middle ear into the cochlea is the complex acoustic input impedance of the cochlea, Z_c. It is defined as the sound pressure in the scala vestibuli at the stapes footplate divided by the volume velocity of the footplate. Direct measurements of Z_c in human ears are available in some studies (e.g., Huttenbrink and Hudde 1994; Merchant et al. 1996; Puria et al. 1997; Aibara et al. 2001). The concept of Z_c has often been used in modelling the cochlear load with discrete element (e.g., Motallebzadeh et al. 2017). On the other hand, some people have explicitly modelled the cochlea coupled to the middle ear (e.g., Gan et al. 2007).

2.3.3 Measurements of vibrations of the tympanic membrane

There have been few studies of the full-field vibration patterns of the TM in human ears, as distinct from measurements at one or a few points. Various methods have been used for this purpose (e.g., Kessel 1874; Békésy 1941; Kobrak 1948). Tonndorf and Khanna (1972) used time-averaged holography in human cadaver ears for the first time, and much later stroboscopic holography was used (Cheng et al. 2010; Rosowski et al. 2011).

Laser Doppler vibrometry (LDV) is a surface velocity measurement technique that employs the Doppler effect on the laser beam when it is reflected to measure the displacement amplitude of TM vibrations. LDV techniques have been employed both in cadaver ears (Gyo et al. 1987; Eiber et al. 2000; Gan et al. 2004; Cheng et al. 2021) and *in vivo* (Huber et al. 2001; Whittemore et al. 2004; Rosowski et al. 2008). Although studying TM motion by LDV mostly has been done through measurements of umbo displacement in the piston-like direction, LDV measurements of multiple points on the TM have been done in our lab (Maftoon et al. 2015; Kose et al. 2020). Scanning laser Doppler vibrometry has been used (Wang and Gan 2018) to do measurements of the full-field TM surface vibration. Recently, Tang et al. (2021) used a high-speed digital holography system to measure both the shape and the displacements of the TM. These studies all described simple patterns of the TM surface displacement occurring at frequencies below 2 kHz, where the different parts of the TM move in-phase, with one to three maxima on the TM. At frequencies above about 2 kHz, the pattern of the displacement becomes more complicated; the number of local maxima increases, and the different maxima are not in phase.

2.3.4 Measurements of vibrations of the ossicles

Kirikae (1960, Chapter 3) did experiments with sound that ‘was close to the sine wave’ (120-1000 Hz, 110-140 dB) and using microscopic stroboscopy of the footplate. Kirikae’s measurements showed that the malleus and incus moved together and concluded that they vibrate

as a rigid body. Gyo (1987) measured the ossicular motion visually with a video measuring device under a microscope. They studied vibration modes of the ossicles and the lever function in human temporal bones and reported that the axis of rotation of the ossicles would change depending on the frequency. Later Decraemer and Khanna (2004) used interferometry and microscopic X-ray computed tomography (microCT) in combination to animate 3D models of the vibrating ossicles. They reported that the motion of the ossicular chain is frequency dependent and becomes complex with increasing frequency. They also mentioned seeing a slippage between the malleus and incus even at low frequencies. The stapes showed a piston-like motion and also a tilting motion even at 1 kHz in some ears. The studies above are in general agreement with each other, the more recent studies providing more and better information because they used more sensitive instruments, measured more points and higher frequencies, and were able to use lower sound pressures.

2.4 Optical coherence tomography

OCT is a new interferometric way to study TM vibration patterns (MacDougall et al. 2016). In addition to simultaneously imaging the anatomy of the middle ear, OCT vibrometry gives us the opportunity to noninvasively observe the displacement patterns of the deep parts of the middle ear, including both the TM and the ossicles.

A recent technical review by Ramier at el. (2018) describes the history of OCT for imaging the middle ear and inner ear. That review was used as the basis of the present review of OCT. First structural imaging with OCT is discussed, followed by how OCT is used for functional imaging of different structures.

Pitris et al. (2001) were among the first who studied OCT for middle-ear imaging. They imaged the middle-ear cavity through the TM in four excised, unfixed, human temporal bones with time-

domain OCT. Shortly after that, Heermann et al. (2002) tested the use of OCT *in vivo* to determine the proper length of the prosthesis to be used in reconstructive surgery. OCT imaging was used as a diagnostic tool for human middle-ear pathologies by Djalilian (2008). They claimed that OCT is useful to monitor post-surgical changes and also the response to pharmacological therapy. OCT has also been used to image the oval window niche during middle-ear reconstruction surgery and to assess the thickness of the stapes footplate in cases of otosclerosis and tympanosclerosis (Just et al. 2009). Similarly, the full-field thickness distribution of the human TM was measured with OCT for individual membranes by Van der Jeught et al (2013).

There have been efforts to build a hand-held OCT probe for otoscopic examination to diagnose otitis media by the Boppart group (Jung et al. 2011; Won et al. 2021). They have studied differences in TM and biofilm thicknesses in normal ears and in ears with chronic and acute otitis media (Monroy et al. 2015). They recently built a multimodal handheld probe integrating Raman spectroscopy and an OCT system for characterizing otitis media (Monroy et al. 2022, 2023). In another study they reported real-time automated thickness measurement of the *in vivo* human TM using OCT (Hubler et al. 2015). Their data included both patients and healthy ears.

Structural imaging of the middle ear is implemented with conventional spectral-domain or time domain OCT. An important recent development is the application of phase-sensitive OCT, also termed Doppler OCT or OCT Doppler vibrometry (OCT-DV), to study the vibration of middle-ear elements in response to sound. Swept-source-based OCT is a kind of spectral domain Doppler OCT with a tunable laser. This system offers fast acquisition, deep penetration and high signal-to-noise ratio (Bonesi et al. 2014; Park et al. 2014). This opens new diagnostic opportunities.

Applegate et al. (2011) recorded mouse TM vibrations with OCT. Subhash (2012) performed the first OCT vibrometry measurements on the ossicular chain. (Chang et al. 2013) showed that an OCT system was capable of visualizing and quantifying acoustic vibrations at several kilohertz. They showed that OCT vibrography using a wavelength-swept laser source could achieve subnanometer amplitude sensitivity with an artificial target. They captured 3D motion of the intact TM and ossicles of the cadaver chinchilla ear over a wider frequency range (0.5 to 5 kHz) and made measurements in simulated pathological conditions (Chang et al. 2013). The sensitivity of TM motion data combined with ossicular motion data to distinguish simulated pathologies (stapes fixation and incus-stapes joint interruption) was reported to be high. A number of OCT vibrometry studies on the human middle ear *ex vivo* were done by a group in Dresden. First they recorded details of TM displacements at different locations and frequencies in a human temporal bone (Burkhardt et al. 2014). Later they studied TM movements during a simulated Eustachian blockage to determine possible clinical applications of middle-ear vibrometry (Kirsten et al. 2015). They also analyzed the use of Doppler OCT for detection of fluid in the patient middle ear, to detect and classify middle-ear effusions related to otitis media (Kirsten et al. 2016), and later developed endoscopic OCT with a wide field-of-view for the morphological and functional assessment of the human TM (Kirsten et al. 2019).

MacDougall et al. (2016) at Dalhousie University performed the first *in vivo* OCT vibrometry measurements in humans. Their system is built around an akinetic swept laser. They used OCT-DV for measurement of stapes vibration in patients with stapes fixation and normal controls (MacDougall et al. 2019). They concluded that OCT-DV is a promising way to assess ossicular mobility before operation. More recently they have built a geometrically accurate real-time volumetric visualization of the middle ear with a handheld probe using OCT. The geometric

accuracy of the resulting images was validated through comparison with co-registered microCT volumes of a phantom target and a cadaveric middle ear (Farrell et al. 2023).

Chapter 3. Finite-element analysis

3.1 Introduction

Quantitative middle-ear modelling has been done in different ways. Two-port models and circuit models have often been used (Funnell et al. 2012). Two-port models are black-box linear models that do not reflect the structure of the system at all. Circuit models are lumped-parameter white-box models that lack a direct connection between their parameter values and the anatomical or physiological properties of the system. The finite-element (FE) method is a numerical method for solving partial differential equations that determine a physical system. In this method, the physical system is subdivided into small parts, called elements, where simple equations can describe the behaviour of each element. These solutions when combined together can describe the complex behaviour of the whole system. The first development of the FE method was in the early 1940s with the work of McHenry, Hrenikoof and Newmark (Zienkiewicz et al. 2013, p. 1) . With the recent advances in digital computers, we are now able to solve systems with large numbers of elements.

In this chapter we discuss fundamentals of FE analysis in section 3.2, and how it has been used in middle-ear modelling in section 3.3.

3.2 Overview of finite-element method

In the FE method, once the physical structure is divided into elements, the mechanical behaviour of each element is analyzed, and its response to applied loads is expressed in terms of the displacements of its nodes. The behaviours of elements can be described by simple systems of equations that are easily solvable, and combining the element matrix equations leads to one overall system matrix equation that represents the complex behaviour of the physical system.

The details of the assembly and analysis of FE models have been discussed in many textbooks (e.g., Zienkiewicz et al. 2013).

As an example, Equation (3.1) defines the relationship between forces and displacements when the behaviour of an element is considered to be static and linear elastic:

$$K_e w = f \tag{3.1}$$

where K_e is the element stiffness matrix, w is the vector of the nodal displacements and f is the vector of nodal forces. The matrices and vectors of equation 3.1 are expanded in equation (3.2) to show the relationship between forces and displacements for an element (Figure 3.1) with nodes 1, 2 and 3:

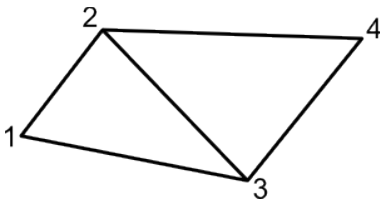

Figure 3.1. Two triangular elements (http://audilab.bme.mcgill.ca/mammie/mammie.pdf)

$$\begin{bmatrix} a_{11} & a_{12} & a_{13} \\ a_{21} & a_{22} & a_{23} \\ a_{31} & a_{32} & a_{33} \end{bmatrix} \begin{pmatrix} w_1 \\ w_2 \\ w_3 \end{pmatrix} = \begin{pmatrix} f_1 \\ f_2 \\ f_3 \end{pmatrix} \tag{3.2}$$

where a_{ij} are the stiffness matrix components, w_i are the nodal displacements and f_i are the nodal forces.

Similarly, for the second element we have the following equation:

$$\begin{bmatrix} b_{11} & b_{12} & b_{13} \\ b_{21} & b_{22} & b_{23} \\ b_{31} & b_{32} & b_{33} \end{bmatrix} \begin{pmatrix} w_1 \\ w_2 \\ w_3 \end{pmatrix} = \begin{pmatrix} g_2 \\ g_3 \\ g_4 \end{pmatrix} \tag{3.3}$$

where b_{ij} are the stiffness matrix components, w_i are the nodal displacements and g_i are the nodal forces.

Now, since the elements are connected at nodes 2 and 3, the w_2 and w_3 in equations 3.2 and 3.3 are the same. Therefore one can combine the two equations as follows:

$$\begin{bmatrix} a_{11} & a_{12} & a_{13} & 0 \\ a_{21} & a_{22}+b_{11} & a_{23}+b_{12} & b_{13} \\ a_{31} & a_{32}+b_{21} & a_{33}+b_{22} & b_{23} \\ 0 & b_{31} & b_{32} & b_{33} \end{bmatrix} \begin{pmatrix} w_1 \\ w_2 \\ w_3 \\ w_4 \end{pmatrix} = \begin{pmatrix} f_1 \\ f_2+g_2 \\ f_3+g_3 \\ g_4 \end{pmatrix}. \quad (3.4)$$

This can be done for thousands or millions of elements in practice. The result is analogous to equation 3.1:

$$Kw = f \quad (3.5)$$

where the system stiffness matrix K is much bigger.

3.3 Procedures for finite-element modelling

FE analysis consists of three parts which will be described in this section. In section 3.3.1 we will describe the first step, the pre-processor; in section 3.3.2 we will explain the second step, the solver; and the third step, the post-processor, will be presented in section 3.3.3. Model validation will be discussed in section 3.3.4.

3.3.1 Pre-processor

To build a good FE model, the following factors should be specified carefully: (1) coordinates of the nodes; (2) the element form and list of nodal connections for each element; (3) boundary conditions and loads; and (4) material properties of the elements.

3.3.1.1 Sources of shape data

There are different approaches to creating the geometry for FE models of the middle ear. Funnell and Laszlo (1978) and Funnell (1983) represented the TM shape parametrically. Rabbitt and Holmes (1986) represented the TM shape with a function that describes the deviation from a conical shape. The geometry of the FE model of Wada et al. (1992) was determined on the basis of published anatomical observations and their own direct measurements of the dimensions of the middle-ear components, without the benefit of imaging technology. Some techniques use

shape from surface measurements. For example, Funnell and Decraemer (1996) described moiré topographic shape measurements for TM FE modelling. Beer et al. (1999) used laser-scanning microscopy to measure the shape of the eardrum surface.

Most middle-ear modelling has been done using techniques involving cross-sectional images. Funnell and Phelan (1981) and Funnell et al. (1992) did FE modelling of the cat middle ear based on serial histological sections. Gan et al. (2004) also later developed a FE human middle-ear model based on histological sections. Others used histological sections as a supplement (e.g., Mikhael et al. 2004; Motallebzadeh et al. 2017). Histological sectioning takes a long time and the specimen preparation is difficult. Moreover, histology sections suffer from image distortion and also have alignment problems.

Orthogonal-plane fluorescence optical sectioning (OPFOS) was used for imaging of intact mammalian samples, first for the cochlea (Voie and Spelman 1995) and then for the tympanic bulla (Voie 2002). Buytaert and Dirckx (2009) also used OPFOS on the gerbil middle ear. This method requires that the specimen be decalcified and cleared (to have the same refractive index throughout its entire volume) and it is often impregnated with a fluorescent dye.

Magnetic resonance microscopy (MRM) was introduced by (Henson et al. 1994), who imaged the cochlea. MRM images were used for FE modelling of the middle ear by Van Wijhe and Funnell (2000) and Daniel et al. (2001). MRM represents soft tissues well, but it offers no contrast between bone and air unless the air cavity is filled with a contrast agent.

The use of X-ray microCT for the middle ear was introduced by two different groups (Vogel and Schmitt 1998; Vogel 1999; Decraemer et al. 2003) and it has been widely used since then. MicroCT avoids many of the disadvantages of other methods and it provides images with voxel

sizes down to a few micrometers. NanoCT was used for measuring the microstructure of the incudostapedial joint in gerbil ears by Feizollah (2019). NanoCT has the ability to provide images with voxel sizes down to a few nanometers, but the sample size that can be used is smaller than with microCT. The use of synchrotron radiation for imaging the ear was introduced by Vogel (1999), providing images of the middle ear with a spatial resolution of about 11 μm. Synchrotron radiation is a very intense, collimated, narrow-bandwidth and tunable photon beam and so offers shorter scan times, no beam-hardening artifacts, higher spatial resolution, and reduced background signal (Thompson et al. 1984). Synchrotron radiation can be used with phase contrast (Elfarnawany et al. 2017; Thompson et al. 2023) which leads to higher contrast for soft tissues since the boundaries of the soft tissues cause a phase shift in the X-rays. The main disadvantage of synchrotron X-ray CT is that access to these sources is very limited.

3.3.1.2 Model geometry

In image-based modelling, the desired structures are segmented from a stack of images (e.g., microCT, OCT, histology sections). Tools for such segmentation are available in many software packages and the segmentation can be done manually, semi-automatically or automatically. In this study we used our locally developed software Fie, Tr3, Fad and Thrup'ny (http://audilab.bme.mcgill.ca/sw/) for modelling. Segmentation and smoothing, topological consistency and connectivity were all established with Fie. After segmentation we defined different subsets, each referring to one particular structure of the middle ear with its own material properties. We made a separate FE mesh for each subset, and connected subsets will have shared surfaces. Tr3 was used for triangulation of the vector-based contours of the segmented structures in different slices to create surface meshes. Cost functions in Tr3 were used to optimize the quality of the triangulation. Fad was used to check the quality of the surface mesh. Volume mesh

generation was done next using Gmsh (http://gmsh.info/). Fad was used to join the different subsets to produce one final mesh that contains all parts of the model, and Thrup'ny was used to view the 3D models. The voxel size of the microCT images was 80 micrometers.

3.3.1.3 Mesh elements

FE elements may be 1-D, 2-D (triangular or quadrilateral), or 3-D (tetrahedral or hexahedral); and may be linear or higher-order. The elements can model different fields, (e.g., mechanical, acoustical, thermal, electromagnetic), or coupled problems. When we model a solid mechanical problem, the elements may model beams, membranes, thin plates, thick plates or shells. In this thesis, triangular shell elements were used for modelling the TM, and the rest of the structures were made of 3D tetrahedron elements. Discrete elements (springs and dashpots) were also used in the modelling.

3.3.1.4 Material properties

The relationship between stress and strain in a structure is related to the material properties. In our study, the sound pressure of 2 $Pa_{0\text{-}p}$ that was used is low enough that it will not drive the system into the non-linear range. We therefore considered linear material parameters for each structure: isotropic Young's modulus, Poisson ratio, mass density and structural damping. The Young's modulus is a property of the material that tells us how easily it can stretch and deform and is the slope of the linear part at the origin of the stress-strain curve for a material under tension or compression. The Poisson ratio is a measure of how much a material tends to expand in directions perpendicular to the direction of compression and usually varies between zero and 0.5 (for an incompressible material). Gradual dissipation of energy within the vibrating system is referred to as damping. There are different types of damping, including viscous damping and hysteretic or structural damping. Viscous damping is proportional to the frequency of the load.

Structural damping, on the other hand, is independent of the frequency of the load, and we calculate the complex stiffness matrix which includes structural damping using the following equation:

$$K' = K(1 + jH) \tag{3.6}$$

where K is the usual real stiffness matrix, H is the matrix of loss ratios η (structural damping coefficients), and $j = \sqrt{-1}$. In this study structural damping was considered and the equations of motion of the system become

$$M\ddot{w} + K'w = f \tag{3.7}$$

where M is the mass matrix, K' is the complex system stiffness matrix, $\ddot{w}$ is the nodal acceleration vector and w is the nodal displacement vector, and f is the load vector.

3.3.1.5 Boundary conditions and loads

The boundary conditions of a model define the interactions of elements with the region outside the model. The boundary conditions here can be defined by setting degrees of freedom to zero for selected nodes of the model. Here the TM was considered to be fully clamped around its periphery (i.e., the six degrees of freedom of the nodes were set to zero). For the springs that represented the AML and PIL, all three degrees of freedom were set to zero at the node where they would be attached to the cavity wall. The cochlear load was modelled with four dashpot elements perpendicular to the stapes footplate.

Loads are external forces applied to the elements. They may be categorized into distributed loads, when they are applied on lines, surfaces (as pressures), or volumes; and concentrated loads, when they are applied on individual nodes. In this thesis, a uniform sound pressure of 2 $Pa_{0\text{-}p}$ at the TM was defined.

3.3.2 Solver

This step includes the solution of the linear or non-linear system equation by different algorithms (e.g., transient or harmonic) for the problem specified in the preprocessor step. Transient analysis finds the response of the system to a specific time-domain input, while in harmonic analysis the system stiffness matrix contains complex numbers that depend on the frequency of a sinusoidal load.

For our FE analysis, we used Salome-Meca V2017.0.2, which provides the integration of Code_Aster solver (http://www.code-aster.org/) with Salome (https://www.salome-platform.org), a generic pre- and post-processor for numerical simulations.

3.3.3 Post-processor

Results will be displayed in a graphical form that includes nodes and elements and values (e.g., stress or displacement) at the degrees of freedom of the nodes.

Simulation results were analyzed extensively in the ParaVis module that represents the integration of ParaView (https://www.paraview.org/) into Salome-Meca. The results were analyzed graphically and also analytically via the Python shell embedded in ParaVis.

3.3.4 Model validation

Model validation is an evaluation of how close the behaviour of a model is to experimental measurements (e.g., Funnell et al. 2012, Chapter 7). Validation of middle-ear models has usually been done by comparing to average data from multiple ears. This has the risk of losing detailed information in the averaging (e.g., Motallebzadeh et al. 2017). For example, the resonance peaks at different frequencies will be washed out. Gladine and Dirckx (2018) addressed this issue by creating average response curves which preserve the typical morphology of the individual

response curve, by first aligning the typical morphological features of the response curves along the frequency axis prior to taking the average.

Even when comparing a model to individual ears, often the overall mean squared error of a frequency response is evaluated (e.g., De Greef et al. 2017). Basing the comparison on multiple data features such as frequency-response peak frequencies, as proposed by Maftoon et al. (2015), allows us to focus on specific features which are important for us.

Comparing a model with individual ears has advantages over comparing it with averaged experimental data, but the model's geometry has usually been different from that of any one of the experimental ears. Mikhael et al. (2004), on the other hand, used LDV experimental data from the same ear that their model's geometry was based on for comparison, and Wang (2019) did it with OCT vibration data.

Preface to Chapter 4

FE models were first created for animal ears (Funnell and Laszlo 1978). Since then, several groups have developed human FE middle-ear models (e.g., Wada et al. 1992; Funnell and Decraemer 1996; Beer et al. 1999; Prendergast et al. 1999; Decraemer et al. 2003; Mikhael et al. 2004; Zhao et al. 2009). FE modelling of the middle ear in combination with OCT data was introduced for the first time by our lab in collaboration with R. Adamson's group at Dalhousie University (Wang 2019). A FE model was built for one cadaver ear from microCT images, and the displacements of the model were compared to the OCT vibration measurements at a single low frequency. The material properties of the models were chosen based on previous studies. It was found that the model displacements were in good agreement with the OCT vibration measurements in terms of the displacement pattern and of the maximal displacement, which appears in the posterior region of the TM. We then had the chance to do such ear-specific model validation for multiple ears.

This chapter presents finite-element modelling of three human middle ears. Section 4.1 provides a brief introduction to FE modelling and OCT. Section 4.2 presents the methodology for building the models and explains why we use OCT data. In section 4.3, the results of the models are compared to the experimental OCT measurements, to each other, and also to the results of previous studies. Section 4.4 includes a discussion of the results, some additional findings, and future work.

Chapter 4. Finite-element modelling based on optical coherence tomography and corresponding X-ray microCT data for three human middle ears

Journal of the Association for Research in Otolaryngology 24(3): 339–363 (2023)

Abstract

Purpose

Optical coherence tomography (OCT) is an emerging imaging modality which is non-invasive, can be employed *in vivo*, and can record both anatomy and vibrations. The purpose here is to explore the application of finite-element (FE) modelling to OCT data.

Methods

We recorded vibrations for three human cadaver middle ears using OCT. We also have X-ray microCT images from the same ears. Three FE models were built based on geometries obtained from the microCT images. The material properties and boundary conditions of the models were obtained from previously reported studies.

Results

Tympanic-membrane (TM) vibration patterns were computed for the three models and compared with the patterns measured using OCT. Frequency responses were also computed for all three models for several locations in the middle ear and compared with the OCT displacements and with the literature. The three models were compared with each other in terms of geometry and function. Parameter sensitivity analyses were done and the results were compared among the models and with the literature. The simulated TM displacement patterns are qualitatively similar

to the OCT results. The simulated displacements are closer to the OCT results for 500 Hz and 1 kHz but the differences are greater at 2 kHz.

Conclusion

This study provides an initial look at the combined use of OCT measurements and FE modelling based on subject-specific anatomy. The geometries and parameters of the existing FE models could be modified for individual patients in the future to help identify abnormalities in the middle ear.

Keywords

Finite-element modelling, Optical coherence tomography, Middle ear, Human, MicroCT, Vibration measurement

4.1 Introduction

Quantitative models of the middle ear using the finite-element (FE) method can help to understand the underlying causes of hearing loss. FE middle-ear models were first created for animal ears [1]. Since then, several groups have developed human FE middle-ear models, [e.g., 2–10]. A middle-ear model definition includes material-property parameters, geometry and boundary conditions. Over the years there have been many studies of the effects of varying material properties on middle-ear sound transmission in FE models, but few modelling studies have considered how anatomical variations [e.g., 11–15] affect function. Some FE modelling studies have looked at the effects of tympanic-membrane (TM) shape [1, 16, 17]. Motallebzadeh et al. [10] and De Greef et al. [18] also investigated the effects of anatomical variability in FE models.

Optical coherence tomography (OCT) is based on low-coherence interferometry, typically with near-infrared light. A recent technical review by Ramier et al. [19] describes the history of OCT for imaging the middle ear and inner ear. Pitris et al. [20], Heerman et al. [21], Djalilian et al. [22] and Just et al. [23] were early users of OCT for middle-ear imaging, and more recently OCT has been used to measure TM thickness in normal and pathological ears [24, 25]. OCT Doppler vibrometry can be used to record motions of the middle ear along with structural imaging [26–29]. MacDougall et al. [29] were the first to do OCT measurements of middle-ear vibrations in live subjects.

There have been few studies of the full-field vibration patterns of the TM in human ears, as distinct from measurements at one or a few points. Tonndorf and Khanna [30] used time-averaged holography in human cadaver ears for the first time, and much later stroboscopic holography was used [31, 32]. Recently, Tang et al. [33] used a high-speed digital holography

system to measure both the shape and the displacements of the TM. These studies all described simple patterns of the TM surface displacement occurring at frequencies below 2 kHz, where the different parts of the TM move in-phase with one to three maxima on the TM. They reported that at frequencies above 2 kHz, the pattern of the displacement becomes more complicated; the number of local maxima increases, and the different maxima are not in phase. OCT measurements are a new way to study TM vibration patterns [29]. In addition to simultaneously imaging the anatomy of the middle ear, OCT vibrometry gives us the opportunity to noninvasively observe the displacement patterns of the whole middle ear, including both the TM and the ossicles.

The validation of computational models has usually been done based on data from different ears than the ones on which the models' geometry were based. Mikhael et al. [6], on the other hand, used experimental data measured by means of laser Doppler vibrometry for the validation of a model whose geometry was built from high-resolution microCT data for the same specimen. Model validation with OCT is potentially powerful because we can evaluate the behaviour of multiple parts of the same middle ear using both geometry and vibration from the OCT data.

FE modelling of a cadaver ear using microCT data in combination with both anatomy and vibration OCT data was introduced by our McGill University and Dalhousie University groups [34]. In this paper we present that model and two new models, and the simulated vibrations of the models are compared to the corresponding OCT vibration measurements. We present a parameter sensitivity analysis and compare the behaviours of the three models.

4.2 Methods

4.2.1 Data

Specimens were the right cadaver ear of a 76-year-old Caucasian male and the right and left ears of a 66-year-old Caucasian male. We have both microCT and OCT data for these cadaver ears. Data were recorded in 2016 Feb (ear 2016-1) and 2017 Jun (ears 2017-1 and 2017-2) at Dalhousie University. The OCT data include B-mode (brightness) structural images and D-mode (Doppler) vibration images. B-mode images are generated at a nominal frame-rate of 20 frames per second (FPS) and the system was configured for 128×128×330-voxel 3D B-mode imaging at about 0.15 volumes per second. A full 3D D-mode volume containing 128 slices of 128×330 images was collected and processed over a total acquisition time of 70 min. Our OCT system consists of a Vernier-tuned distributed Bragg-reflector akinetic swept laser (Insight Photonics Solutions, Model SLE-101, central wavelength λ = 1550 nm, tuning bandwidth = 40 nm, nominal repetition rate f_s = 100 kHz, nominal power P_0 = 20 mW). This system has a fast sweeping rate and a long coherence length, l_c > 200 mm, which gives the possibility of imaging the full depth of the human middle ear. The ear canal was partially drilled away to aid alignment of the system for imaging. The field of view of the laser was designed to be 10×10 mm. During the OCT recording, a sound stimulus of 100 dB SPL (2 Pa_{rms}) was applied to the TM through a tube speaker (Etymotic Research, ER3A) and a speculum (Figure 4.1). The stimulus was

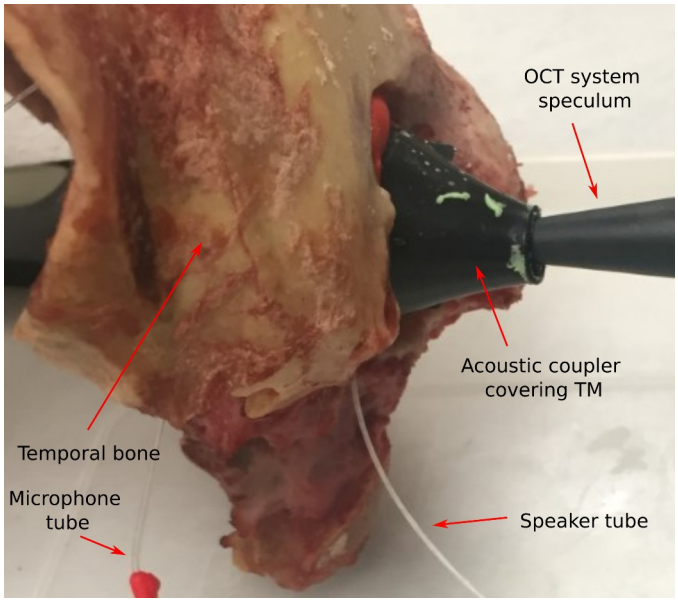

Figure 4.1. Setup for OCT measurement in temporal bones.

delivered through a tube located within 3 mm of the TM and near to the annulus to keep the sound tube out of the OCT field of view. The wavelengths at the frequencies involved here are so long that the sound-pressure field will be practically uniform across the TM and between the tip of the sound-delivery tube and the TM. The sound pressure level was monitored using a calibrated tube microphone (Etymotic Research, ER7C Series B). This system was previously described by MacDougall et al. [29].

The OCT data for each ear include peak-to-peak displacements for three frequencies: 500 Hz, 1 kHz and 2 kHz for ears 2017-1 and 2017-2, and only 500 Hz for ear 2016-1. For each frequency there are two volumes of static B-mode images (before and after Doppler OCT recording) and a volume of D-mode images. The microCT images were acquired using a Triumph II PET/SPECT/CT scanner (TriFoil Imaging, Chatsworth, California). The X-ray energy was set to 75 kVp. The microCT images for each ear contain 512 sections of 512×512 pixels each. The isotropic voxel size is 81 μm.

4.2.2 Software

OCT animation software (Animator) was developed by the Dalhousie group and uses a GPU and CUDA (Nvidia). The software uses a ray-casting approach to volume rendering of the OCT data [35] to create 3D volumetric images (Figure 4.2). The software can also produce 3D visualizations that fuse B-mode and D-mode data to show the harmonic response of the tissues in response to sound as an animated, exaggerated displacement, moving during a harmonic excitation. This can be used to qualitatively analyze the displacement results from the OCT measurements.

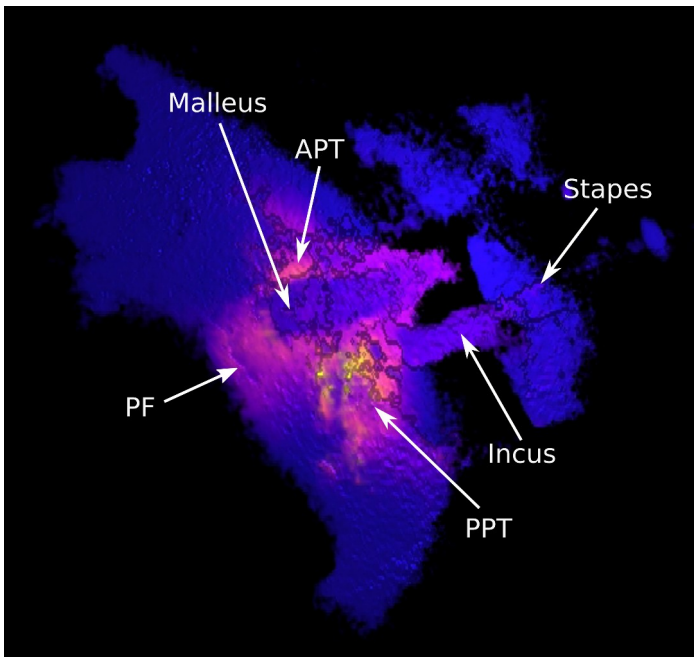

Figure 4.2. Volume rendering of OCT measurement of ear 2017-2 at 2 kHz. PPT = posterior pars tensa, APT = anterior pars tensa, PF = pars flaccida.

The Fie program (developed in our lab along with Tr3 and Fad (http://audilab.bme.mcgill.ca/sw/) was used to perform image segmentation and to specify the material properties, the boundary conditions and the mechanical loads. Two complete FE models have been built based on the microCT data for ears 2017-1 and 2017-2 (Figure 4.3a, b) in addition to the one built previously [34] for ear 2016-1 (Figure 4.3c). The original format of the microCT data is individual DICOM files. This format was converted to a format that Fie can recognize (i.e., 8-bit TIFF, JPEG or PNG). The original DICOM images have 16 bits/channel, so we examined the histograms and determined a good grey-level range to reduce the pixel data down to 8 bits/channel (i.e., 8 bits/pixel for grey-level images, which have a single channel). ImageMagick (https://imagemagick.org/) was used to reduce the number of bits and to convert DICOM files to JPEG. The value of 95 for quality (which has a maximum value of 100) was used to specify the amount of lossy JPEG compression.

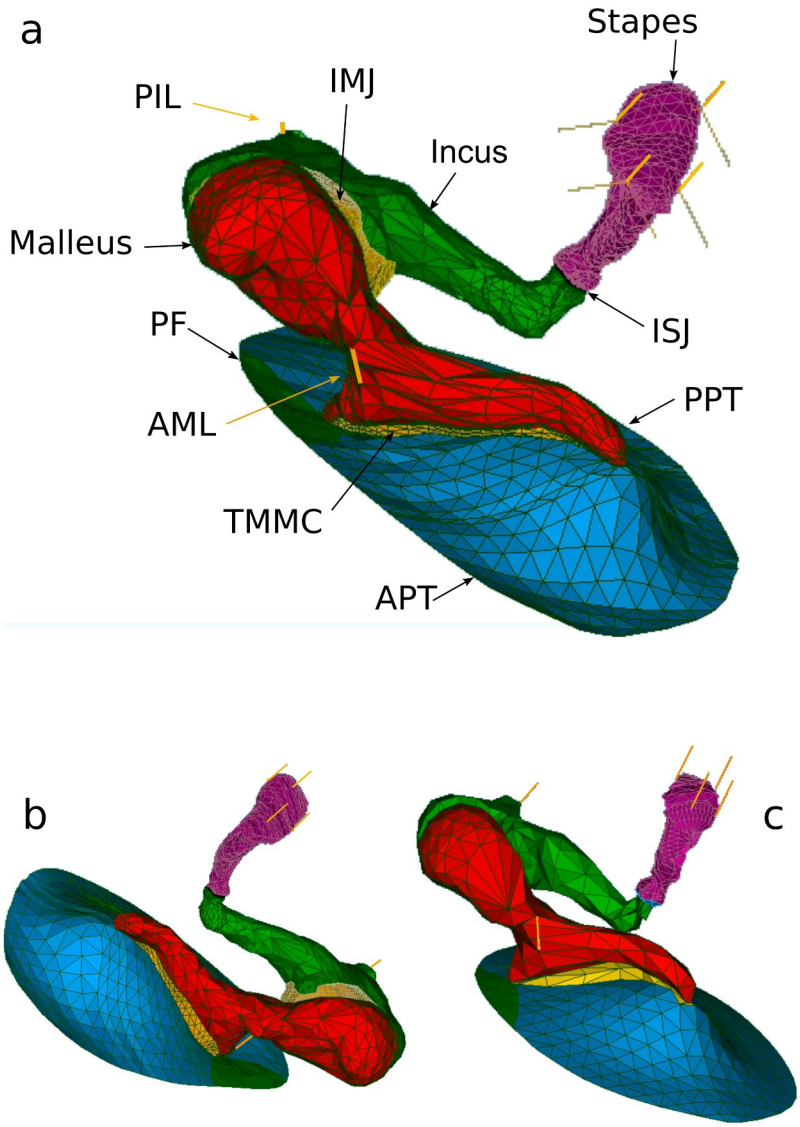

Figure 4.3. Finite-element models of three human ears. (a) ear 2017-1, (b) ear 2017-2, (c) ear 2016-1. PPT = posterior pars tensa, APT = anterior pars tensa, PF = pars flaccida, TMMC = TM-malleus connection, AML = anterior mallear ligament, IMJ = incudomallear joint, PIL = posterior incudal ligament, ISJ = incudostapedial joint

We segmented the microCT images manually in each slice. The Tr3 program was then used for the generation of triangulated surfaces, and the volume mesh generation was done with Gmsh [36]. Fad was used to join the different structures to produce a final mesh representing all parts of the model. The models contained the following separate structures: pars tensa (PT) of the TM, pars flaccida (PF) of the TM, TM-malleus connection (TMMC), malleus, incus, stapes,

incudomallear joint (IMJ), and incudostapedial joint (ISJ) (Figure 4.3[1]). The IMJ was included only in the models for ears 2017-1 and 2017-2. Histological images of human ears were used as a supplement during modelling because the soft-tissue contrast of the microCT images was inadequate for image segmentation of soft-tissue structures.

For FE analysis we used Salome-Meca V2017.0.2, which integrates Code_Aster 13.4 and astk 2017.0 (http://www.code-aster.org/). We used this old version because newer versions could not be used remotely. The astk tool is used to run Python command files and link all input and output files together to run simulations. Salome-Meca provides integration of the Code_Aster solver with Salome (https://www.salome-platform.org), a generic pre- and post-processor for numerical simulations. Simulation results can be analyzed extensively in the ParaVis module that represents the integration of ParaView (https://www.paraview.org/) into Salome-Meca. The results can be analyzed graphically and also analytically via the Python shell embedded in ParaVis.

Specifying a uniform sound pressure of 2 $Pa_{0\text{-}p}$ at the TM, we computed the frequency response of the system over a frequency range of 100 Hz to 10 kHz for 500 consecutive frequencies. Harmonic analysis was also performed for the frequencies 500 Hz, 1 kHz and 2 kHz, so that we can compare the simulation results with the OCT measurements, which were made at those three frequencies and at that sound pressure level. Simulations were done on an Intel Core i7-4790 CPU with 8 GB RAM and Ubuntu Linux 18.04. Each simulation for the calculation of the frequency response of the model, with one set of parameters, takes between 0.8 and 8.5 min, depending on the model. Sensitivity analysis (coded in Python) was performed on the same system.

1 In the published article, this reference was incorrectly changed from Figure 3 to Figure 2.

4.2.3 Specifications of FE models

The TM was represented by a single layer of shell elements, with uniform thickness within the PT and within the PF. The TM boundary was assumed to be fully clamped. The ear canal was not modelled. The anterior mallear ligament and the posterior incudal ligament were also not modelled. Instead, three very stiff orthogonal springs, each having a stiffness of 1000 N/m, were attached to a node at each of those ligaments' locations, effectively fixing those nodes for translation but not for rotation. The annular ligament of the stapes was modelled with springs located at four different nodes on the stapes footplate and approximately perpendicular to the footplate. The baseline stiffness of each of the springs was set to 50 N/m. This is based on the experimental measurement of the stiffness of the annular ligament by Kwacz et al. [37]. They used atomic force microscopy to measure the elastic properties of the annular ligaments in two cadavers. The cochlear load was modelled with four dashpot elements perpendicular to the stapes footplate. The baseline damping coefficient was taken to be 0.2 Ns/m [7, 10] divided among the four dashpots. As displacements occurring in the middle ear in response to a 2-Pa sound pressure are small, linear material properties (isotropic Young's modulus and Poisson ratio) were defined for each structure of the middle ear separately. Linear (first-order) elements were used in the FE modelling. For the TM, triangle shell elements were used, and the rest of the model was made of 3D tetrahedron elements, except for the springs and the dashpots which were modelled as discrete elements. Each unconstrained node of a shell element has six DOFs: three translational (x, y and z) and three rotational (around x, y and z). In contrast, each unconstrained node in a 3-D solid element has only three DOFs, all of them translational.

Table 4.1 shows the base material properties we used for different structures of the middle ear [18]. The third column of the table shows other sources that had used these same values before De Greef et al. [18]. The Young's moduli of the PT and PF were decreased for 2017-1 and

2017-2, but not for 2016-1, from the base value to half that value because otherwise the TM was too stiff. For all structures we considered uniform material properties. For the ossicles, a loss ratio of 0.01 was used. For the PT, PF, TMMC and the joints, a loss ratio of 0.2 [38] was used. A Poisson ratio = 0.3 was used for the ossicles and a value of 0.49 was used for the soft tissues.

Table 4.1. Baseline material properties

Structures	Baseline values	Sources
Eardrum		
Mass density (kg/m^3)	1200	[54]
Young's modulus (MPa)		
PT	20	
PF	6.7	
Malleus		
Mass density (kg/m^3)	2550	[55 pp. 87-94]
Young's modulus (GPa)	1.41	[56]
Incus		
Mass density (kg/m^3)	2360	[55 pp. 87-94]
Young's modulus (GPa)	1.41	[56]
Stapes		
Mass density (kg/m^3)	2200	[55 pp. 87-94]
Young's modulus (GPa)	1.41	[56]
ISJ		
Mass density (kg/m^3)	1200	[43]
Young's modulus (MPa)	6	[41]
IMJ		
Mass density (kg/m^3)	1200	[43]
Young's modulus (MPa)	7	[57]
TMMC		
Mass density (kg/m^3)	1200	[43]
Young's modulus (MPa)	2	

4.2.4 Mesh convergence analysis

A coarse FE mesh is computationally less expensive than a fine mesh, but the results may not be accurate enough. A systematic mesh convergence analysis should be done to choose an

appropriate mesh resolution. We performed mesh convergence tests using the Homard tool in Salome-Meca. We bisected the elements of the soft structures (TM, IMJ, ISJ, TMMC) from the initial mesh three times and calculated the percentage difference between the displacement results for three specific nodes in the model: one node on the posterior PT (PPT) of the TM, one node at the umbo and one node at the middle of the stapes footplate. We plotted the displacement magnitudes of the frequency response after each model refinement. We considered the low-frequency displacement magnitude and the first and second resonance frequencies and concluded that the results had converged if the changes were less than 5%. Based on this criterion, we used the model with no refinement of the TM, with the IMJ and the TMMC being refined once and with the ISJ being refined twice. The model definitions can be found on-line [39].

4.2.5 Parameter sensitivity analysis

After assigning baseline material properties of the models, the material parameters were increased and decreased, one parameter at a time, by factors of 1.5 and 3 from their baseline values. We chose two factors because we wanted to check a wide range of parameter values and we also wanted to know if the changes are linear or not. We simulated the model behaviour and calculated the frequency responses of the models as the parameters changed, and then we quantified the changes between the frequency-response results for each scenario.

4.2.6 Comparison of OCT and model results

For the TM spatial vibration pattern, quantitative comparison of the simulation results and the OCT vibration measurements was done by comparing the presence of maximum displacements in three parts of the TM: PF, PPT and anterior PT (APT). Both relative magnitudes and the numbers of maxima were considered during the comparison. For the models we used the displacement maps and considered a point to be a local maximum if its displacement was at least twice as high as the displacements of the points at the nearest minima. The OCT data are very

noisy and we needed to watch the vibration animations (produced by the Animator software) from different angles to locate the manubrium and different parts of the TM, incus and stapes and to find the maximum displacements and the phases on the TM. After locating the maxima, we marked them on the screenshots of the vibration maps of the TM using Inkscape (https://inkscape.org/). These marked-up images of the TM vibration patterns can be compared with the corresponding simulated displacement magnitude patterns of the TM. The displacement magnitudes of five points (one on the PPT, one on the APT, one at the umbo, one on the long process of the incus and one on the stapes) were also compared one by one between the OCT measurements and the models for different frequencies.

4.3 Results

4.3.1 Frequency responses

Figure 4.4 shows frequency responses from our three FE models, for the umbo (panel a) and stapes footplate (panel b), along with both model results and experimental data from the literature. The experimental data include those of Gyo et al. [40] (one ear, as reported by Koike et al. [41]), Gan et al. [7] (ranges reported for ten ears) and Cheng et al. [42] (four individual ears), all measured in cadaveric temporal bones. The results obtained by FE analysis are from Sun et al. [43], Koike et al. [41] and Gan et al. [7]. The models are different from one another by up to a factor of 20. The results of the models from previous studies shown in Figure 4.4 lacked peaks and valleys over the frequency range, which may have been due to low frequency resolution or heavy damping or both. The experimental data show more peaks and valleys and they are very different between individual bones and between the groups. For the umbo, the displacements for our models fall within the range of the previous experimental and modelling results at frequencies lower than about 2 kHz but are lower at higher frequencies. For the stapes,

the displacements of our models are higher than the experimental data below 1 kHz but they are still within the range of the values of the previous models. Our models have differences among themselves of up to a factor of 2 at lower frequencies and even more at higher frequencies.

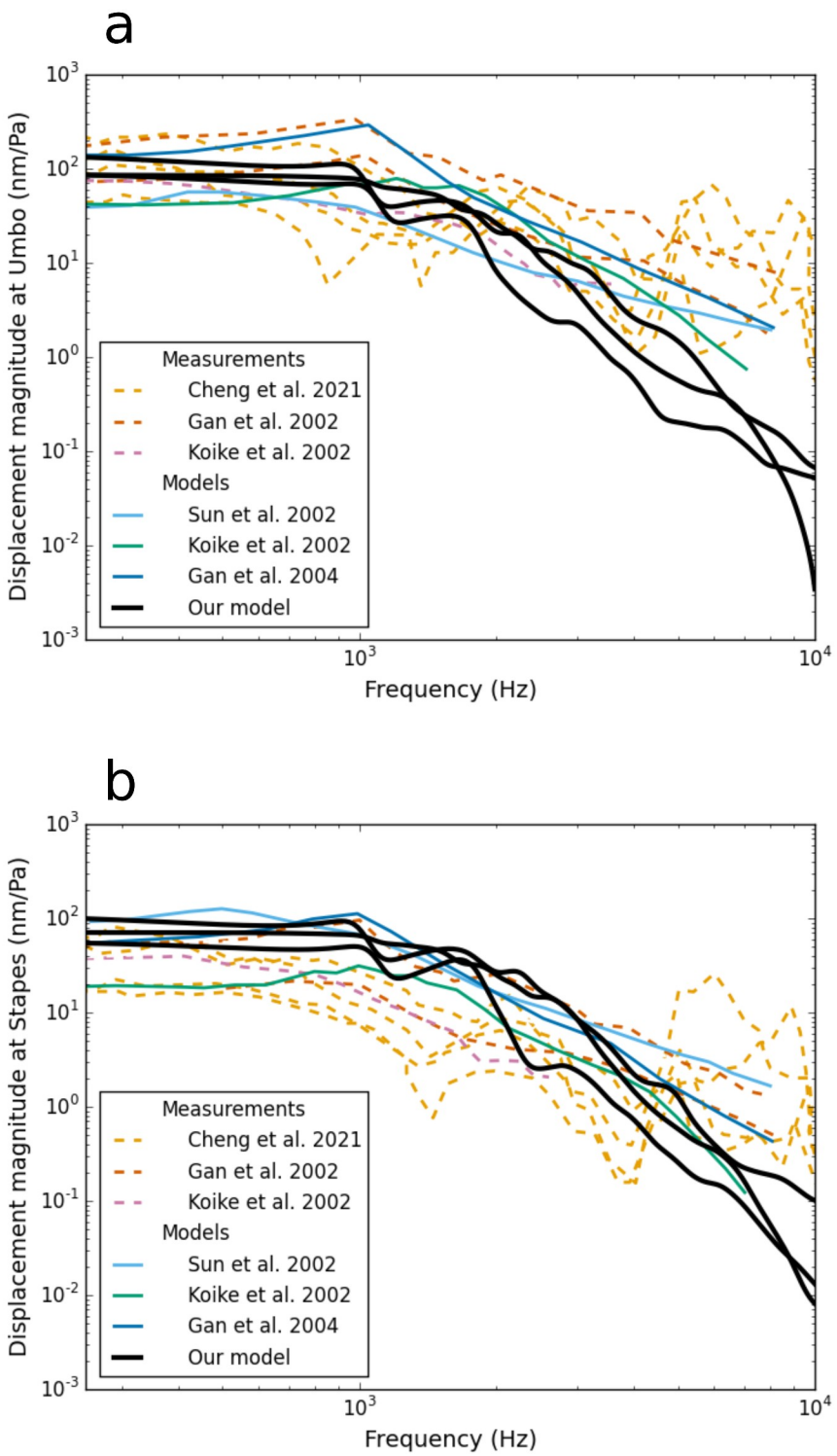

Figure 4.4. Comparison of frequency responses of FE models from this study with published experimental data and previous models. (a) at umbo, (b) at stapes.

4.3.2 Comparison of OCT measurements and simulation results

In Figures 4.5, 4.6 and 4.7 the left panels show the TM vibration patterns extracted from the experimental OCT measurements for frequencies of 500 Hz, 1 kHz and 2 kHz, and the right panels show the simulation results for the base models for the three ears at the same frequencies. The orange line on an OCT image represents the canal wall while the cyan line represents the TM boundary, with a dashed line indicating the part that is hidden by the canal wall. There was a smaller field-of-view during the recording for ear 2016-1, which results in seeing only a portion of the TM. Maxima are shown by black closed lines. The phases of the vibrations of the ears were estimated from the animations of these data (see example animation on-line [39]). If the phase of a local maximum is different from the phase of the global PT maximum by about 180°, it is shown with a dashed line. If the phase is different by about 90° it is shown with a dotted-dashed line. Locations that in the animations appear to correspond to travelling waves are shown by dotted lines. We see artifacts (with the centres of two maxima on the PT being blue instead of yellow) in the OCT data of ear 2017-1 at 1 kHz, because the TM vibration levels in those regions exceeded one half of the optical wavelength of 1550 nm, causing the phase-unwrapping algorithm to break down.

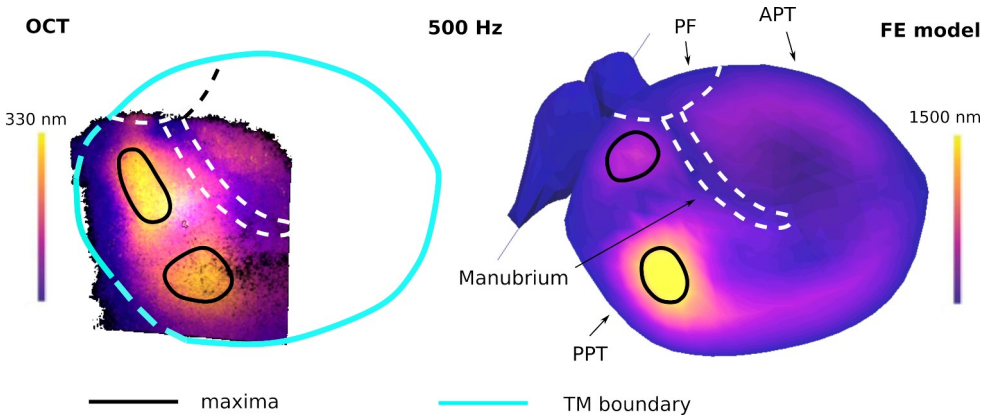

Figure 4.5. Vibration displacement maps from OCT measurements and FE simulations at 500 Hz for ear 2016-1. PPT = Posterior pars tensa (PT), APT = anterior pars tensa (APT), PF = pars flaccida (PF)

For all three bones at 500 Hz, the simulated vibration pattern has a global maximum on the PPT and a broad maximum on the APT, and the displacements in different parts of the TM are all in phase. In the OCT data also we see the global maximum on the PPT. For the OCT data of ears 2017-1 and 2017-2 we see three maxima, including the global maximum and two smaller maxima on the PPT. For the OCT data of 2017-1 and 2017-2 there is one local maximum on the APT with a magnitude of about half of the global maximum. For the OCT data of ear 2016-1, only a small part of the APT was recorded because the field of view was limited, but there was a low broad maximum that can be seen in the superior part of the APT.

At 1 kHz there are one large maximum and two smaller maxima on the PPT in the models for both 2017-1 and 2017-2. For the OCT data of 2017-1 we see two maxima on the PPT which have similar magnitudes but different phases. For the OCT data of 2017-2 there is one global maximum on the PPT and three smaller local maxima that have different phases. The OCT data for both ears show a relatively low-amplitude local maximum on the APT which is not seen in the simulation results, where the displacements on the APT are very small, with no evident maximum.

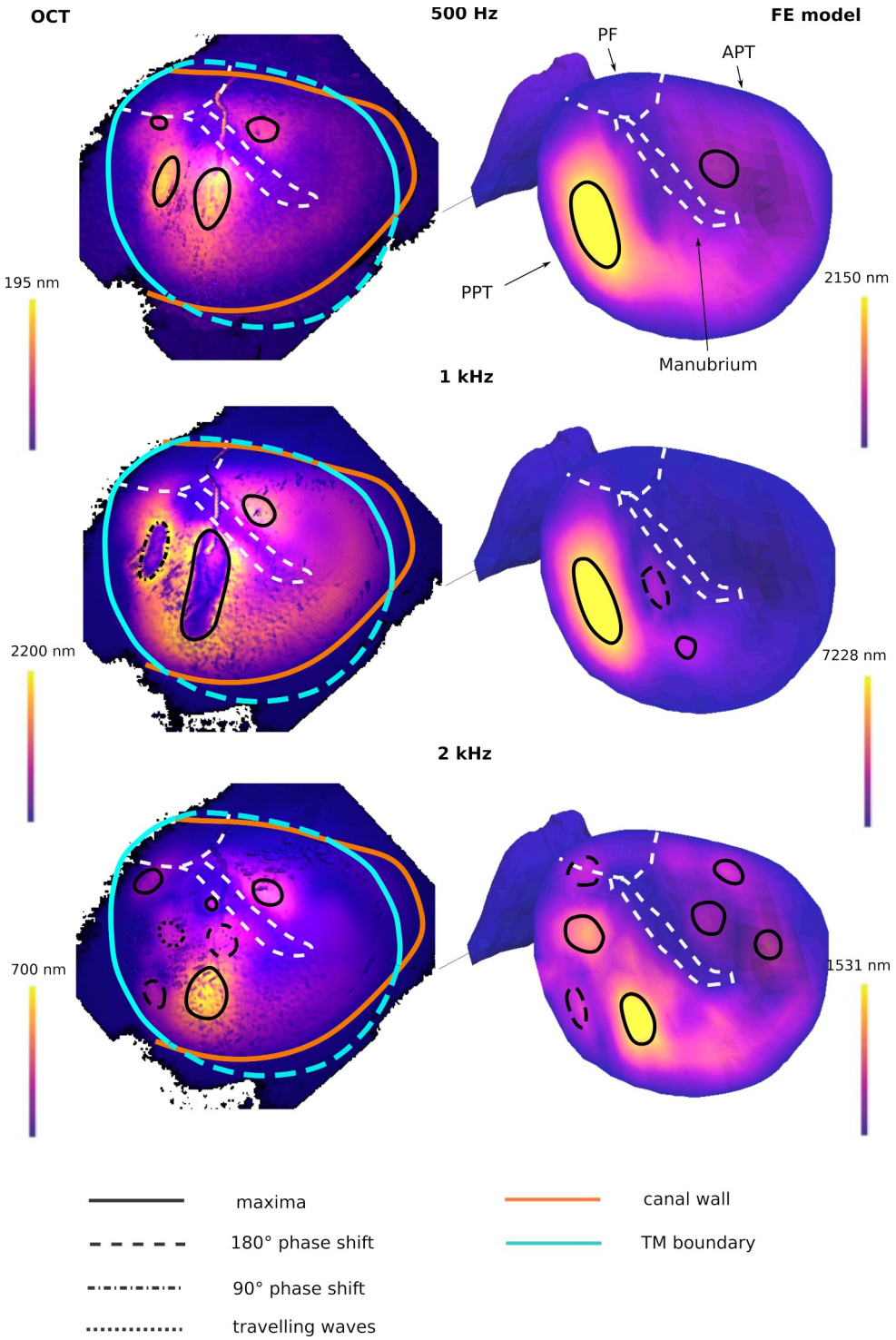

Figure 4.6. Vibration displacement maps from OCT measurements and FE simulations at 500 Hz, 1 kHz and 2 kHz for ear 2017-1. PPT = Posterior pars tensa, APT = anterior pars tensa, PF = pars flaccida.

At 2 kHz there are three local maxima on the PPT of the 2017-1 model, and the 2017-2 model has four maxima. There are three local maxima on the APT of the 2017-1 model while 2017-2

has four maxima. Both the 2017-1 and 2017-2 models show one maximum on the PF. The magnitudes of the APT and PPT maxima of ear 2017-2 are close in value, for both the model and the OCT, but for ear 2017-1 the maxima on the PPT have higher magnitudes, for both the model and the OCT.

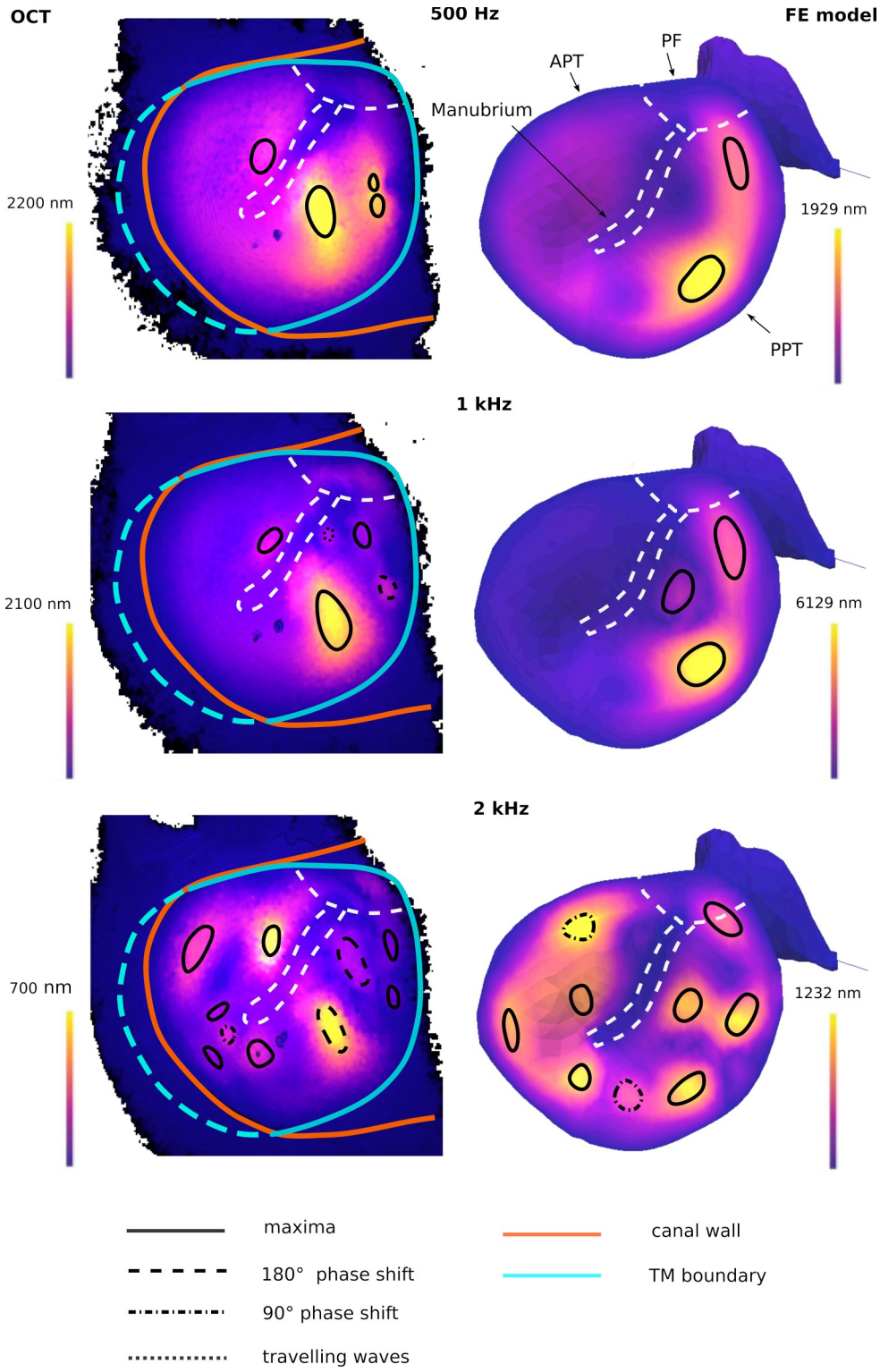

Figure 4.7. Vibration displacement maps from OCT measurements and FE simulations at 500 Hz, 1 kHz and 2 kHz for ear 2017-2. PPT = Posterior pars tensa, APT = anterior pars tensa, PF = pars flaccida.

In Figure 4.8, panels a, b and c show the displacement magnitudes for five locations estimated from the OCT measurements for all three ears, along with the displacement magnitudes for the models at the same frequencies. For the OCT data we selected the locations that show the maximum displacements in the PPT and in the APT. In addition, we considered the umbo, long process of incus, and stapes, whose locations were estimated as described in Methods. For the model, we chose four fixed nodes (in the middle of the APT, at the umbo, on the long process of the incus, and on the stapes head) that correspond to the OCT locations at which we measured. (The displacements are about 2% higher at the stapes head than at the footplate for frequencies below 2 kHz.) For the PPT, however, since the models all had distinct maxima but at different locations, we selected the model node with the maximum displacement rather than using a fixed node. The experimental measurements at different frequencies were done separately and there was uncertainty about the sound pressure value at the TM in some cases, possibly because of leaks in the sound system. Therefore, for this figure, at each frequency the OCT measurements for the umbo were scaled so that they had the same displacement magnitude as in the model, and then the OCT measurements for the other locations were adjusted by the same scale factor. In Figure 4.8, some of the differences between the model displacements and the corresponding OCT displacements are quite large, especially for the PPT. We scaled the OCT results based only on the umbo displacements because the OCT results are less noisy at the umbo than at the deeper locations. If we instead scaled the OCT curves to give the best overall match to the model results at all locations, the differences between the OCT and model results would appear smaller. Either way, most of the differences seen here are probably smaller than the displacement changes that are caused by some pathological middle-ear conditions. Figure 4.8 shows that the displacements for PPT, incus and stapes are always larger in the model. The results for the models have maximum differences from the scaled OCT results of between 1.2 dB and 3.6 dB for different

ears on the PPT for frequencies of 500 Hz and 1 kHz and the differences become as large as 11.6 dB at 2 kHz in ear 2017-2. The incus and stapes have similar magnitudes for both OCT and the models except for the OCT data for ear 2017-2, where the stapes displacements are smaller. The umbo-to-incus magnitude ratio is mostly about twice as high for OCT but at 2 kHz for ear 2017-2 the ratio is about five times as high for OCT. The magnitude of the APT displacement is sometimes estimated well by the model but in some cases there is a difference of about a factor of 10 between the model and OCT.

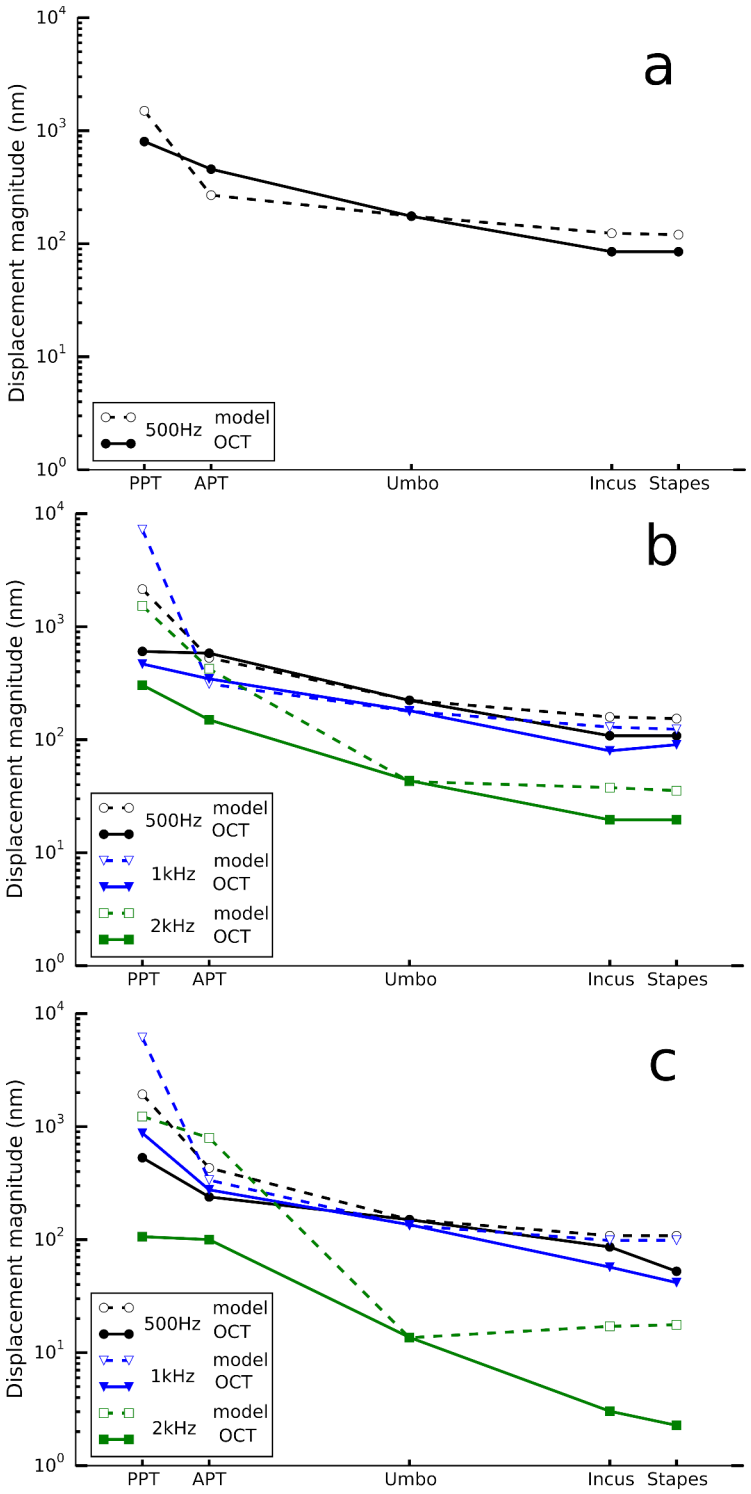

Figure 4.8. Displacements for five locations of the middle ear. (a) ear 2016-1, (b) ear 2017-1, (c) ear 2017-2. Dashed lines are for simulated results, solid lines are for experimental OCT data scaled as described in the text.

4.3.3 Parameter sensitivity analysis

A parameter sensitivity analysis was done to see how changing parameter values affects the model behaviour. This helps us to understand which model parameters are most responsible for various features of a model's output, and can give hints on how to improve the model by adjusting the parameters. Figure 4.9 shows the results of increasing and decreasing the parameters for the model of ear 2017-2 by factors of 1.5 and 3. Panels a to c represent changes of low-frequency displacement magnitude for the PT, umbo and stapes, and panel d shows changes of the PT resonance frequency. The horizontal positions of the different values for each parameter are located at the values 0.33, 0.67, 1, 1.5 and 3 on locally linear scales, where 1 corresponds to the base value of the parameter and the other values represent the scaling of the parameter. The results were qualitatively and quantitatively similar for the other ears. From Figure 4.9 we see that the thickness and Young's modulus of the PT have significant effects on the low-frequency displacement values of the middle ear on the TM and ossicles. Displacements on the ossicles are also affected by the stiffness of the annular ligament and the cochlear impedance. The Young's modulus of the TMMC and IMJ have negligible effects and the Young's modulus of the ISJ changes the results only for the ossicles. The changes of the displacement magnitude and resonance frequency were not always linear when parameter values were changed. Details of the non-linearities are discussed below for some parameters.

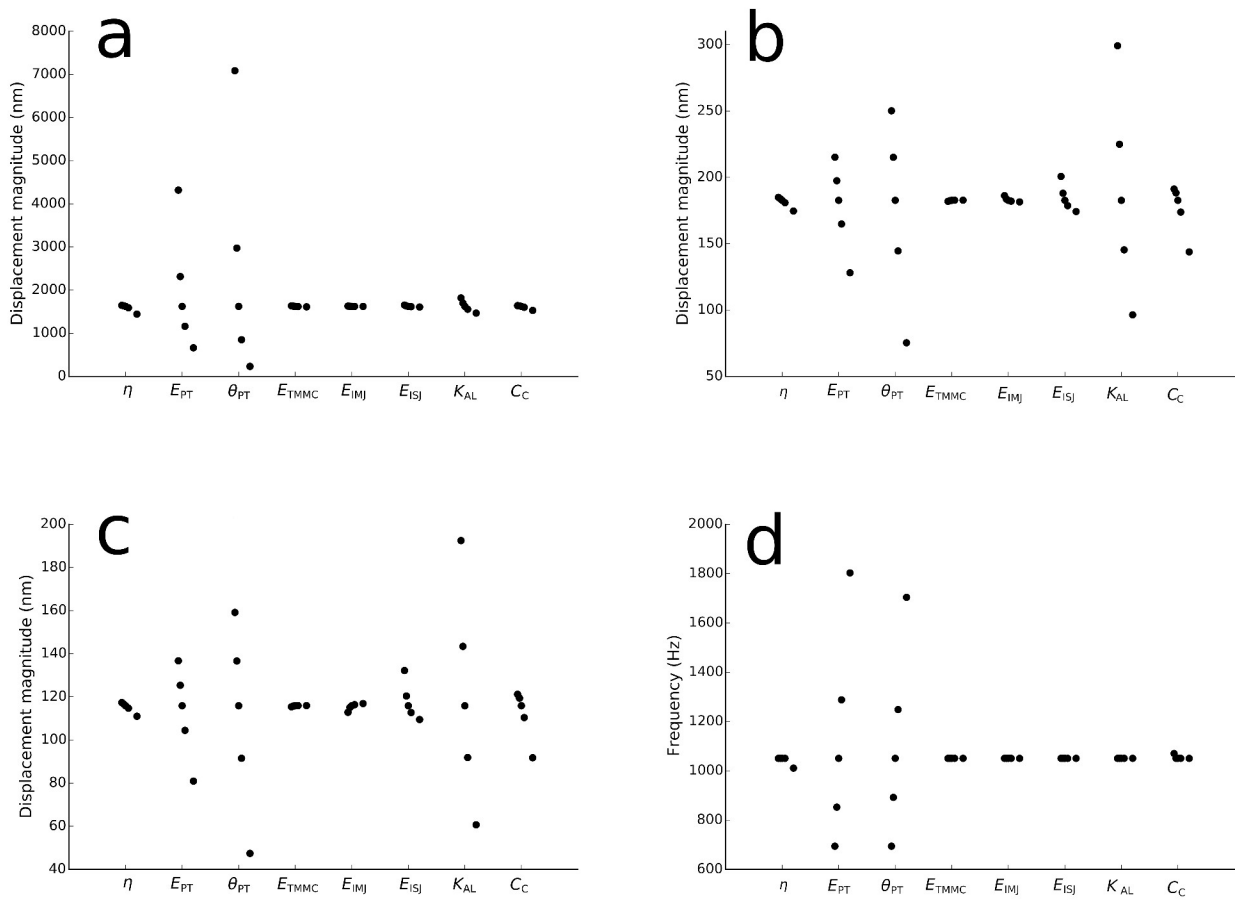

Figure 4.9. Parameter sensitivity analysis. (a) maximum displacement magnitude on PT, (b) displacement magnitude at umbo, (c) displacement magnitude on stapes, (d) resonance frequency of PT. The horizontal line indicates different parameter values. θ_{PT} *= thickness of pars tensa,* E_{PT} *= Young's modulus of pars tensa,* C_C*= cochlear damping,* E_{IMJ} *= Young's modulus of incudomallear joint,* E_{ISJ} *= Young's modulus of incudostapedial joint,* E_{TMMC} *= Young's modulus of TM-malleus connection,* K_{AL} *= stiffness of stapedial annular ligament,* η *= loss ratio.*

Further details of Figure 4.9 will be discussed below in the context of Figures 4.10 to 4.17, which show the complete frequency responses for parameter increases and decreases. The results are again qualitatively and quantitatively similar among the ears so we only present the figures for ear 2017-2. In the following sections we discuss the results for different parameters. The displacements ($nm_{0\text{-}p}$) correspond to an applied pressure of 2 $Pa_{0\text{-}p}$.

4.3.4 Thickness and Young's modulus of pars tensa

In Figures 4.10 and 4.11 we see that the frequency response curves for the umbo and stapes shift downward for increasing PT thickness and Young's modulus for frequencies below about 1 kHz. The curves also shift to higher frequencies as both the PT thickness and Young's modulus increase, causing displacement increases for frequencies above about 1 kHz. Figure 4.9 shows that increasing the thickness of the PT by a factor of 1.5 will decrease the low-frequency displacement magnitude of the PT by about 50%, and decreasing it by the same factor will increase the displacement by about 100%. This is true for all three ears. The effects are smaller at the ossicles. The umbo and stapes displacement magnitudes change by about 40% for ear 2016-1 and by about 20% for ears 2017-1 and 2017-2. The PT displacement changes are larger when the PT thickness decreases, while the displacement magnitudes of the ossicles change more when the PT thickness increases. If the thickness of PT is increased by a factor of 1.5 it will increase the main resonance frequency of the middle ear by about 20%, and if it is decreased by a factor of 1.5 it will decrease the resonance frequency by about the same amount. Figure 4.10 shows that the troughs of the frequency response of the PT change dramatically when the PT thickness is changed. We see, from smallest to largest thickness, that the first trough is very rounded, then somewhat rounded, then very sharp, then quite round, and then very sharp again. Presumably this is because of interactions with resonances at other locations on the PT. The number of troughs is greater when the thickness is lower, and when there are more troughs some of them are rounder.

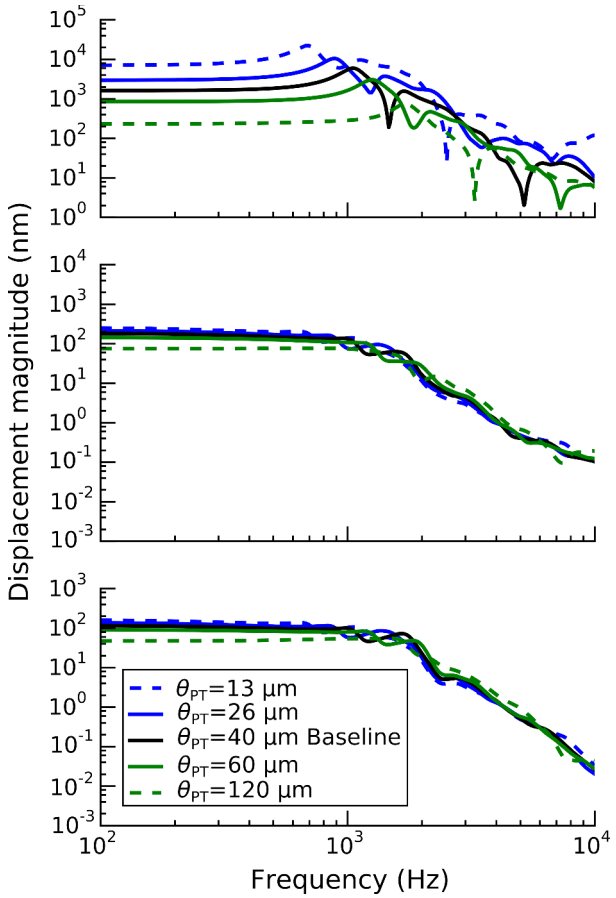

Figure 4.10. Effects of θ_{PT} (thickness of pars tensa) on frequency response of FE model for ear 2017-2. Top set of curves is for PT, middle set is for umbo, bottom set is for stapes

Figure 4.9 shows that increasing the Young's modulus of the PT by a factor of 1.5 will decrease the low-frequency displacement magnitude of the PT by 30%, and decreasing it by the same factor will increase the displacement by about 50%. Figure 4.11 shows that increasing the Young's modulus of the PT by a factor of 1.5 shifts the frequency of peaks and valleys to higher frequencies by about 20% for the PT, umbo and stapes. Again, this is true for all three ears. The displacement magnitude changes for the umbo and stapes at lower frequencies are about 20% for ear 2016-1 and 10% for ears 2017-1 and 2017-2. The Young's modulus of the PT has larger effects on the displacement magnitude at higher frequencies on the ossicles while changes due to the PT thickness are more constant across frequencies. When the Young's modulus of the PT is

changed, the damping of the PT will also change because we have a constant loss ratio, and this will increase the effect on the displacements at higher frequencies. Changes of the PT thickness have stronger effects on the displacements than changes of the Young's modulus of the PT do.

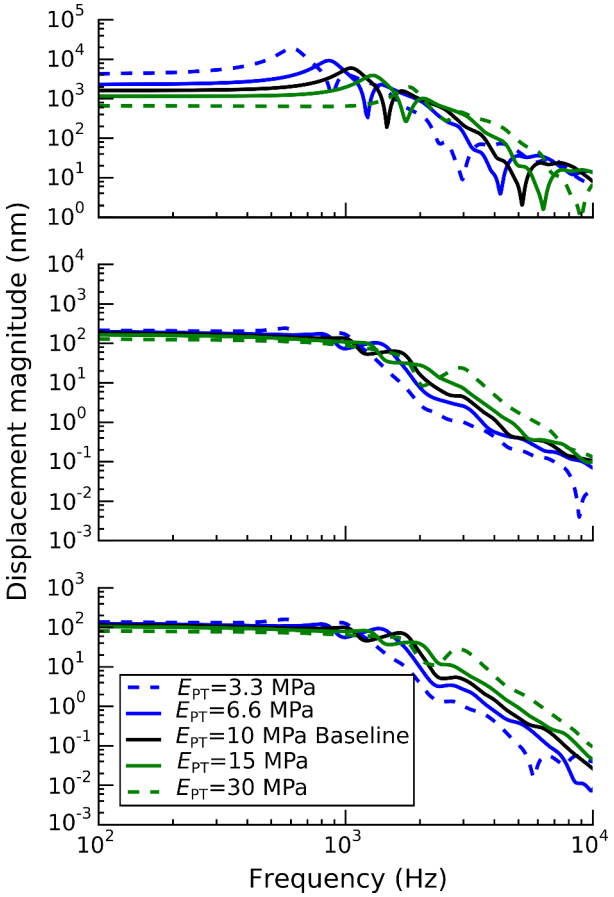

Figure 4.11. Effects of E_{PT} *(Young's modulus of pars tensa) on frequency response of FE model for ear 2017-2. Top set of curves is for PT, middle set is for umbo, bottom set is for stapes.*

4.3.5 Cochlear damping

Figure 4.12 shows the results for different cochlear damping values, again for ear 2017-2.

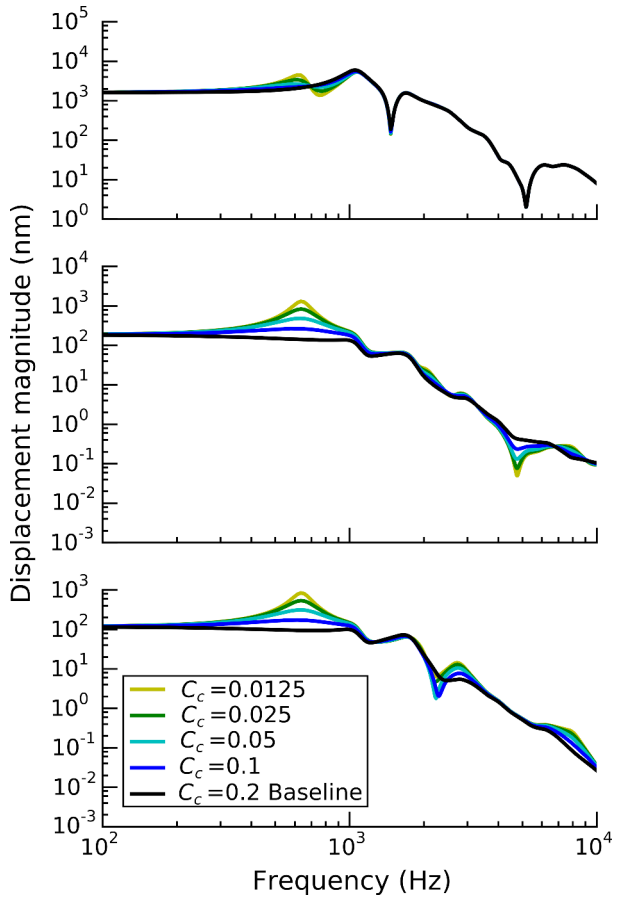

Figure 4.12. Effects of C_C *(cochlear damping) on frequency response of FE model for ear 2017-2. Top set of curves is for PT, middle set is for umbo, bottom set is for stapes.*

Increasing the cochlear damping beyond the baseline value had practically no effect, but we tested a wider than usual range of values lower than baseline. The motivation was to see whether cochlear damping might be obscuring some resonances of the middle ear. The maximum of the frequency response for the TM is at 1 kHz regardless of the cochlear damping values. At the lowest damping value tested, 0.0125, we see a shoulder or an extremely low peak on the umbo and stapes at 1 kHz for 2017-1 and 2017-2, which presumably reflects the TM peak. We also see a maximum in the umbo and stapes frequency responses at ~ 600 Hz for ears 2017-1 and 2017-2. For those ears the TM has a small peak close to this ossicular maximum, and there is a minimum

in between that and the main maximum, at around 750 Hz. In the model for 2016-1, this ossicular resonance frequency is at ~ 900 Hz, closer to the main resonance of the PT at 1 kHz, and it is not visible in the PT frequency response even at the lowest level of damping. As the values of the cochlear damping were increased, the first peak became smaller until it disappeared by 0.1. This suggests that some part of the ossicular chain in this model has a resonance frequency at less than 1 kHz which is heavily damped by the cochlear impedance. At frequencies higher than 1 kHz, the TM frequency response does not change with changes in the cochlear damping, while minima and maxima in the frequency responses of the umbo and stapes become sharper with the decreased cochlear damping.

4.3.6 Joints and TM-malleus connection

In Figures 4.13 and 4.14 we see that the Young's moduli of the IMJ and ISJ do not have any noticeable effect on the TM frequency response and they have small effects on the umbo and stapes frequency responses. For the IMJ, the resonance frequency and the displacement magnitude at frequencies below 2 kHz change by less than 5%, but we see larger changes in the magnitude at higher frequencies. The Young's modulus of the ISJ changes the frequency response between 1 and 4 kHz at the umbo and stapes and at other frequencies the effect is less than 5%. A trough on the stapes frequency response shifts from about 2 kHz to about 3.4 kHz when the Young's modulus of the ISJ is increased and the trough also becomes deeper.

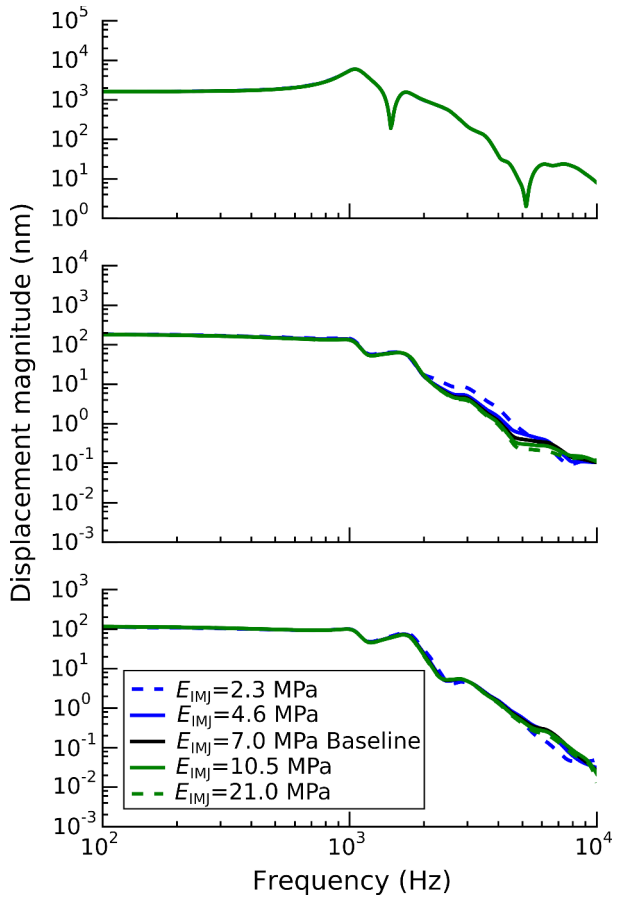

Figure 4.13. Effects of E_{IMJ} *(Young's modulus of incudomallear joint) on frequency response of FE model for ear 2017-2. Top set of curves is for PT, middle set is for umbo, bottom set is for stapes.*

Figure 4.15 shows the effects of damping of the ISJ on the models. The figures contain two situations: the baseline loss ratio of 0.2 and a lightly damped ISJ with a loss ratio of 0.01. We see that when the damping is very light a sharp peak and one or two sharp valleys appear between 3 and 5 kHz for both umbo and stapes. The features essentially disappear for the baseline value of damping. There is a similar pattern for ear 2016-1 but the model for ear 2017-1 does not have these features. The stapes is tilted with respect to the TM in ear 2017-1 and the footplate is displaced in the oval window, which may be why these features are not present in this ear. As

mentioned above, ear 2017-1 is also more sensitive to decreases of the Young's modulus of the IMJ.

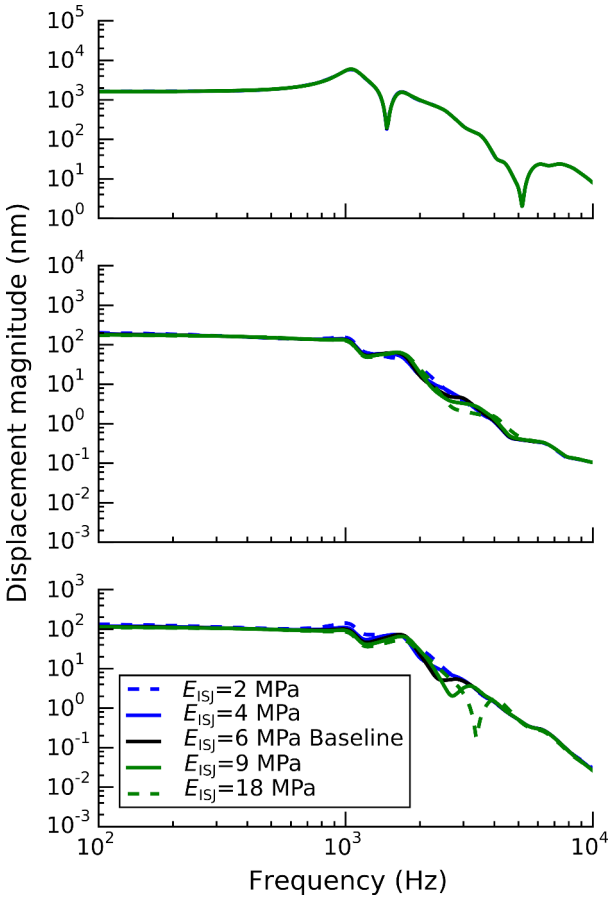

Figure 4.14. Effects of E_{ISJ} *(Young's modulus of incudostapedial joint) on frequency response of FE model for ear 2017-2. Top set of curves is for PT, middle set is for umbo, bottom set is for stapes.*

Varying the Young's modulus of the TMMC over the range of 0.66 to 6 MPa caused changes of less than 2% in the TM, umbo and stapes displacements.

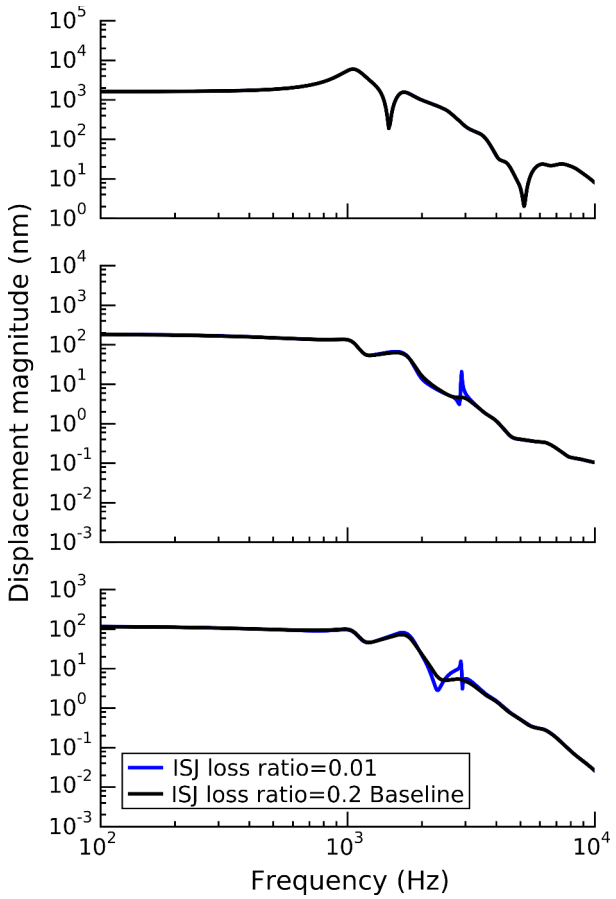

Figure 4.15. Effects of ISJ loss ratio on frequency response of FE model for ear 2017-2. Top set of curves is for PT, middle set is for umbo, bottom set is for stapes.

4.3.7 Stiffness of stapedial annular ligament

Figure 4.16 shows that the stiffness of the stapedial annular ligament changes the PT displacements by less than 3% in ear 2017-2, and the same is true in the other two ears. Changes in the frequency response of the umbo and stapes for a change by factor of 1.5 are about 10% for ear 2016-1 and about 20% for ears 2017-1 and 2017-2.

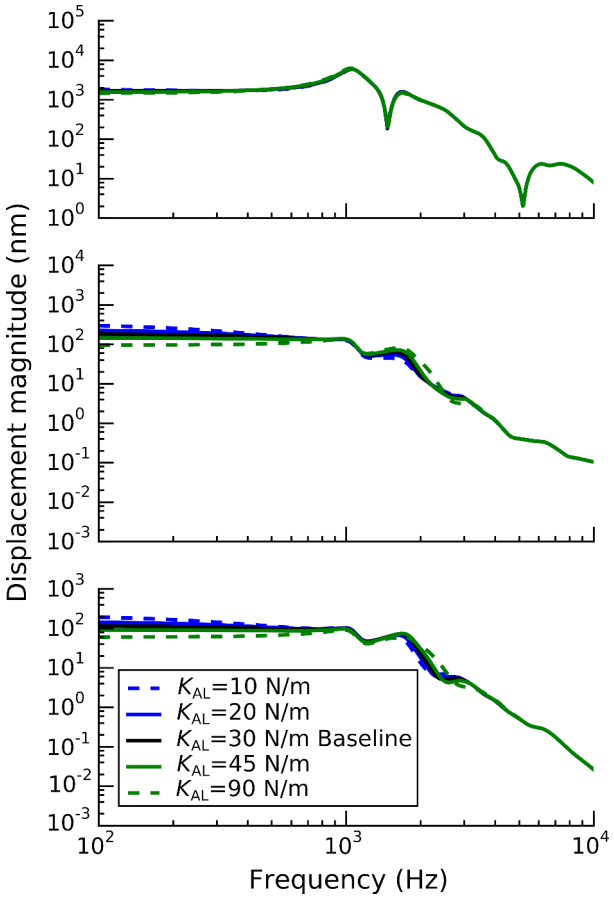

Figure 4.16. Effects of K_{AL} *(stiffness of stapedial annular ligament) on frequency response of FE model for ear 2017-2. Top set of curves is for PT, middle set is for umbo, bottom set is for stapes.*

4.3.8 Loss ratio

Figure 4.17 shows that increasing the loss ratio will decrease the magnitudes of the peaks of the frequency response of the PT and ossicles. Note, however, that minima for the PT are deepest at the baseline value of damping and either increasing or decreasing the loss ratio makes the minima less deep. Changing the damping did not noticeably shift the resonance frequency.

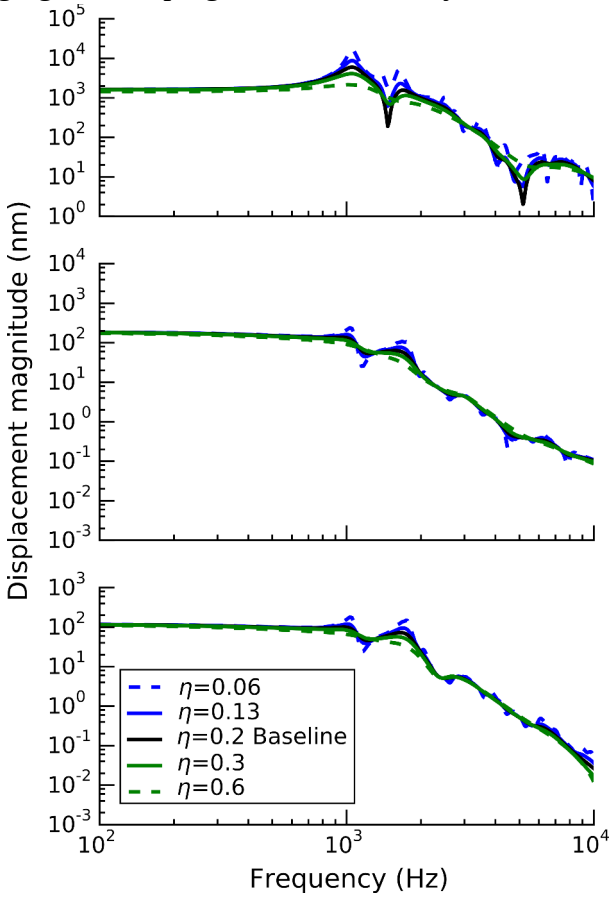

Figure 4.17. Effects of η *(loss ratio) on frequency response of FE model for ear 2017-2. Top set of curves is for PT, middle set is for umbo, bottom set is for stapes.*

4.4 Discussion

In this study we modelled three cadaveric human middle ears. We were able to compare the models to the OCT measurements in terms of the TM displacement patterns and also the displacement values extracted from the OCT data for the umbo, incus and stapes. The TM displacement patterns from the simulations are qualitatively similar to the OCT measurement data for the three ears, as described for Figures 4.5, 4.6, and 4.7. Figure 4.8 shows the measured

and simulated displacement magnitudes for the different locations in each ear. The figure shows that, for the locations considered, the displacement values of the models are closest to the OCT measurements at 500 Hz and the difference is greatest at 2 kHz. As in all middle-ear modelling, at around 1 kHz significant discrepancies between experimental and model responses can arise from relatively small differences in the main middle-ear resonance frequency, and at higher frequencies significant discrepancies can arise from small differences in the complex spatial patterns.

As described in Methods, ears 2017-1 and 2017-2 were the left and right ears of the same individual. These ears were similar in size but the orientation of the stapes with respect to the TM was different between the two ears. Because the middle ear space was not violated during the dissection, we believe that the difference in stapes location was most likely due to a pathological condition or a congenital abnormality of the ear rather than being an artefact of its preparation. In general there is considerable variability among ears [e.g., 11–13, 15], especially in the stapes [e.g., 44]. Ear 2016-1 was about 10% larger in size in all directions than ears 2017-1 and 2017-2. Ear 2016-1 belonged to a person 170 cm in height while ears 2017-1 and 2017-2 belonged to a person 183 cm in height. The ear size was not proportionate to the height of the individual, which is not surprising given the variability between people not only in size but in shape and proportions.

Having multiple models helped us in evaluating the relationship between the shape and behaviour of the models. The models have different frequency responses that vary by up to a factor of 2 at low frequencies and they are more different at higher frequencies (Figure 4.4). The baseline material properties were the same except for the Young's modulus of the TM, which was made twice as high in the 2016-1 model as discussed in Methods. As described in Results,

the three models respond similarly to changes of the parameters. Based on the geometries of the three ears we had, the results of the parameter sensitivity analysis are very similar among the three ears. Only the sensitivity to ISJ damping was different from the others in ear 2017-1, in which the stapes had a different orientation. If we want to make general claims about how geometry and size of different parts of the middle ear will affect the model behaviour, we will need to have more samples. We did not test the sensitivity of the models to changes of the shapes and dimensions of the structures, but this has been done in a few previous studies. Funnell and Laszlo [1] looked at the effects of the TM shape by varying geometric parameters in a cat eardrum model and they concluded that the curvature and conical shape of the TM are important. Moiré shape measurement was used by Funnell and Decraemer [16] to build individualized FE models for four different animal ears, and the effects of the variability were examined. They also scaled the TM boundary by 5%, which changed the TM displacements by 4–15%. Koike et al. [17] analyzed three models with different depths of the TM and found that the transmission factor changed by about 5 dB if the depth was changed by a factor of 2. Motallebzadeh et al. [10] provided an estimate of the effects of anatomical variability by varying the size of their model by ± 5% and ± 10% in the x, y and z directions separately and also in all three directions simultaneously, which changed the results by up to 50% for 10% changes. De Greef et al. [18] concluded that the influence of different shapes of the TMMC (whether narrow or wide) was limited to 2.3 dB.

From the parameter sensitivity analysis we found that the parameters of the model that affected its behaviour the most were the PT thickness and the Young's modulus of the PT. This is in agreement with previous studies [e.g., 6, 7, 10]. The influence of the value of the annular-ligament stiffness was large, which is also in agreement with previous studies [e.g., 6, 18]. The

fact that the results are sensitive to such parameters suggests that ear-specific modelling may be required for each patient. While material properties would be difficult to measure for each ear and may require parameter fitting, TM thickness may be determined from OCT [24, 25, 45]. As previous studies have also found, the damping coefficients of the TM and soft tissues are also important [e.g., 10, 18, 41]. Values of the viscous cochlear damping had a large effect on the stapes displacements, which is in agreement with previous studies [e.g., 7, 18]. We found that it also has an effect on the number of resonances seen on the TM if the value for the damping is unrealistically low (Figure 4.12), as described in Results, which could give some insight into the individual resonating structures in the middle ear, whose resonances are usually indistinguishable.

There were various assumptions in our modelling. The PT thickness was considered uniform, but in reality the PT has a non-uniform thickness as was measured in previous studies [e.g., 24, 46, 47]. Some studies have modelled a nonuniform thickness for the human TM [4, 18, 41, 43], but most have assumed a uniform thickness, even if this parameter is considered to have a strong effect on the model results [e.g., 48]. Isotropy was considered here for the TM because there is no strong direct evidence for functional anisotropy [e.g., 49]. De Greef et al. [18] used both isotropic and orthotropic material properties for the TM in their models and concluded that the results had differences of less than 3.3 dB over the frequency range of 0.1 to 10 kHz, and the vibration patterns of the TM were similar for the two types of model.

The IMJ was not considered in the creation of the model for ear 2016-1 and therefore the model had about 10 times fewer elements and was computationally much less expensive (about 10 times faster). The IMJ is wide and thin and its shape is such that we need to have many elements to have an acceptable aspect ratio for the elements. In our parameter sensitivity analysis it was

found that the IMJ Young's modulus changed the resonance frequency and the displacement magnitude for frequencies up to 2 kHz by less than 5 percent. Increasing the IMJ Young's modulus to that of bone had negligible effects, and decreasing it by a factor of ten below baseline changed the displacement magnitudes up to 2 kHz by only about a factor of 4 or less. Considering the fact that modelling the IMJ is very time consuming because of its rather complex saddle shape and the great uncertainty of its boundaries in the microCT images, we suggest that, at least for frequencies up to 2 kHz, the ear can be modelled without the IMJ and with the incus and malleus having a shared surface, to have a less computationally expensive model. Hoffstetter et al. [50] also reported that the Young's modulus of the IMJ did not significantly change the results of their FE model of the human middle ear, but there are some contradictory experimental data [51, 52]. The coupling between the incus and the stapes, on the other hand, can be expected to be important because it converts the largely rotational movements of the malleus and incus to the largely piston-like movements of the stapes. In our parameter sensitivity analysis the Young's modulus and damping of the ISJ both changed the shape of the frequency response, mostly between 1 and 4 kHz (Figures 4.14 and 4.15), and this is in agreement with previous studies [e.g., 4, 7, 17, 18]. The Young's modulus of the TMMC was reported to be influential by Hoffstetter et al. [50] and De Greef et al. [18] but we found it to have an effect of less than 2%, which is in agreement with Koike et al. [41].

Although we have computed frequency responses up to 10 kHz for the three models, the frequency of the OCT data here is limited to 500 Hz, 1 kHz and 2 kHz. We can use 500-Hz OCT data to represent frequencies lower than that because the frequency response is rather flat at such frequencies. The middle ear's main resonance frequency is close to 1 kHz, which is a disadvantage of using 1 kHz to characterize an ear because the displacement magnitudes will be

affected by any shift of the resonance. The TM is reported to start having complex vibration patterns at 2 kHz [e.g., 32], which makes 2 kHz useful for checking whether we see the same trend or not.

A drawback of the OCT volume measurement is the long time needed for each data recording. For this reason OCT measurements were made at a limited number of frequencies. If we used point measurements, they could be obtained at a much faster rate and having more frequencies would be feasible. If a FE model could be validated using OCT data for more frequencies, we could better infer how the ear was functioning at other frequencies.

Our OCT data for the incus and stapes are limited for the purpose of investigating their motions because we only see the vibrations of the long process of the incus and part of the stapes, and only the vibration component in the direction of the laser beam (which is approximately parallel to the axis of the ear canal and to the piston direction of the stapes) is measured. The model displacements here were measured in the same direction.

Figure 4.4 shows that the frequency responses of our models fall faster at high frequencies than the experimental data do. We think this might be because of the way energy dissipation is modelled and/or because of modelling the TM as isotropic [53], and/or because of not modelling the suspensory ligaments. Because our models were compared to OCT measurements that were only up to 2 kHz, we did not attempt to address this issue.

In this study three FE models were validated with their own OCT vibration data at three different frequencies. Parameter sensitivity analysis results were compared among the models and with the literature. In the future it will also be possible to build models in which pathological conditions are simulated, such as stapes fixation and ISJ interruption. MicroCT imaging of

patients would not be possible and, while real-time volumetric OCT B-mode acquisition has already been demonstrated in patients [29], further advances in middle-ear OCT technology will be needed to enable acquisition of volumetric Doppler OCT data in a clinically feasible acquisition time. The geometries of the existing FE models could be modified for the new patients based on clinical CT images. The OCT values at the measured points could be compared with the simulation results of the new model. Parameters of the new model could be adjusted to fit the measurements and might be able to identify abnormalities in the middle ear.

4.5 References

1. Funnell WRJ, Laszlo CA (1978) Modeling of the cat eardrum as a thin shell using the finite-element method. J Acoust Soc Am 63:1461–1467. https://doi.org/10.1121/1.381892

2. Wada H, Metoki T, Kobayashi T (1992) Analysis of dynamic behavior of human middle ear using a finite-element method. J Acoust Soc Am 92:3157–3168. https://doi.org/10.1121/1.404211

3. Beer HJ, Bornitz M, Hardtke HJ, Schmidt R, Hofmann G, Vogel U, Zahnert T, Hüttenbrink KB (1999) Modelling of components of the human middle ear and simulation of their dynamic behaviour. Audiol Neurootol 4:156–162. https://doi.org/10.1159/000013835

4. Prendergast PJ, Ferris P, Rice HJ, Blayney AW (1999) Vibro-acoustic modelling of the outer and middle ear using the finite-element method. Audiol Neurotol 4:185–191. https://doi.org/10.1159/000013839

5. Daniel SJ, Funnell WR, Zeitouni AG, Schloss MD, Rappaport J (2001) Clinical applications of a finite-element model of the human middle ear. J Otolaryngol 30:340–346. https://doi.org/10.2310/7070.2001.19393

6. Mikhael CS, Funnell WRJ, Bance M (2004) Middle-ear finite-element modelling with realistic geometry and apriori material- property estimates. Proc 28th Ann Conf Can Med Biol Eng Soc

7. Gan RZ, Feng B, Sun Q (2004) Three-dimensional finite element modeling of human ear for sound transmission. Ann Biomed Eng 32:847–859. https://doi.org/10.1023/B:ABME.0000030260.22737.53

8. Zhao F, Koike T, Wang J, Sienz H, Meredith R (2009) Finite element analysis of the middle ear transfer functions and related pathologies. Med Eng Phys 31:907–916. https://doi.org/10.1016/j.medengphy.2009.06.009

9. Zhang X, Guan X, Nakmali D, Palan V, Pineda M, Gan RZ (2014) Experimental and modeling study of human tympanic membrane motion in the presence of middle ear liquid. J Assoc Res Otolaryngol JARO 15:867–881. https://doi.org/10.1007/s10162-014-0482-8

10. Motallebzadeh H, Maftoon N, Pitaro J, Funnell WRJ, Daniel SJ (2017) Finite-element modelling of the acoustic input admittance of the newborn ear canal and middle ear. J Assoc Res Otolaryngol JARO 18:25–48. https://doi.org/10.1007/s10162-016-0587-3

11. Todd NW (2005) Orientation of the manubrium mallei: inexplicably widely variable. Laryngoscope 115:1548–1552. https://doi.org/10.1097/01.mlg.0000173171.32899.4e

12. Todd NW (2007) Pars flaccida retraction and mastoid size: relationship in clinically normal specimens. J Laryngol Otol 121:1020–1024. https://doi.org/10.1017/S0022215107006305

13. Todd NW (2008) The malleus-stapes offset. Laryngoscope 118:110–115. https://doi.org/10.1097/MLG.0b013e318155a299

14. Bradshaw AP, Curthoys IS, Todd MJ, Magnussen JS, Taubman DS, Aw ST, Halmagyi GM (2010) A mathematical model of human semicircular canal geometry: a new basis for interpreting vestibular physiology. J Assoc Res Otolaryngol JARO 11:145–159. https://doi.org/10.1007/s10162-009-0195-6

15. Todd NW, Daraei P (2014) Morphologic variations of clinically normal mallei and incudes. Ann Otol Rhinol Laryngol 123:461–467. https://doi.org/10.1177/0003489414527228

16. Funnell WRJ, Decraemer WF (1996) On the incorporation of moiré shape measurements in finite-element models of the cat eardrum. J Acoust Soc Am 100:925–932. https://doi.org/10.1121/1.416252

17. Koike T, Wada H, Kobayashi T (2001) Effect of depth of conical-shaped tympanic membrane on middle-ear sound transmission. JSME Int J Ser C-Mech Syst Mach Elem Manuf. https://doi.org/10.1299/JSMEC.44.1097

18. De Greef D, Pires F, Dirckx JJJ (2017) Effects of model definitions and parameter values in finite element modeling of human middle ear mechanics. Hear Res 344:195–206. https://doi.org/10.1016/j.heares.2016.11.011

19. Ramier A, Rosowski J, Yun S-H (2018) Optical coherence tomography for imaging the middle and inner ears: A technical review. AIP Conference Proceedings 1965(1):id.020001

20. Pitris C, Saunders KT, Fujimoto JG, Brezinski ME (2001) High-resolution imaging of the middle ear with optical coherence tomography: a feasibility study. Arch Otolaryngol Head Neck Surg 127:637–642. https://doi.org/10.1001/archotol.127.6.637

21. Heermann R, Hauger C, Issing PR, Lenarz T (2002) Erste Anwendungen der optischen Kohärenztomographie (OCT) in der Mittelohrchirurgie. Laryngo-Rhino-Otol 81:400–405. https://doi.org/10.1055/s-2002-32213

22. Djalilian HR, Ridgway J, Tam M, Sepehr A, Chen Z, Wong BJF (2008) Imaging the human tympanic membrane using optical coherence tomography in vivo. Otol Neurotol 29:1091–1094. https://doi.org/10.1097/MAO.0b013e31818a08ce

23. Just T, Lankenau E, Hüttmann G, Pau HW (2009) Optische Kohärenztomographie in der Mittelohrchirurgie. HNO 57:421–427. https://doi.org/10.1007/s00106-009-1907-2

24. Van der Jeught S, Dirckx JJJ, Aerts JRM, Bradu A, Podoleanu AG, Buytaert JAN (2013) Full-field thickness distribution of human tympanic membrane obtained with optical coherence tomography. JARO 14:483–494. https://doi.org/10.1007/s10162-013-0394-z

25. Hubler Z, Shemonski ND, Shelton RL, Monroy GL, Nolan RM, Boppart SA (2015) Real-time automated thickness measurement of the in vivo human tympanic membrane using optical coherence tomography. Quant Imaging Med Surg 5:69–77. https://doi.org/10.3978/j.issn.2223-4292.2014.11.32

26. Subhash HM, Wang RK (2013) Optical coherence tomography: Technical aspects. In: Liang R (ed) Biomedical optical imaging technologies: biological and medical physics, biomedical engineering. Springer-Verlag Berlin Heidelberg, pp 163–212

27. Chang EW, Cheng JT, Röösli C, Kobler JB, Rosowski JJ, Yun SH (2013) Simultaneous 3D imaging of sound-induced motions of the tympanic membrane and middle ear ossicles. Hear Res 304:49–56. https://doi.org/10.1016/j.heares.2013.06.006

28. Park J, Carbajal EF, Chen X, Oghalai JS, Applegate BE (2014) Phase-sensitive optical coherence tomography using an Vernier-tuned distributed Bragg reflector swept laser in the mouse middle ear. Opt Lett 39:6233. https://doi.org/10.1364/OL.39.006233

29. MacDougall D, Farrell J, Brown J, Bance M, Adamson R (2016) Long-range, wide-field swept-source optical coherence tomography with GPU accelerated digital lock-in Doppler vibrography for real-time, in vivo middle ear diagnostics. Biomed Opt Express 7:4621. https://doi.org/10.1364/BOE.7.004621

30. Tonndorf J, Khanna SM (1972) Tympanic-membrane vibrations in human cadaver ears studied by time-averaged holography. J Acoust Soc Am 52:1221–1233. https://doi.org/10.1121/1.1913236

31. Cheng JT, Aarnisalo AA, Harrington E, Hernandez-Montes MDS, Furlong C, Merchant SN, Rosowski JJ (2010) Motion of the surface of the human tympanic membrane measured with stroboscopic holography. Hear Res 263:66–77. https://doi.org/10.1016/j.heares.2009.12.024

32. Rosowski J, Cheng J, Merchant S, Harrington E, Furlong C (2011) New data on the motion of the normal and reconstructed tympanic membrane. Otol Neurotol 32:1559–1567. https://doi.org/10.1097/MAO.0b013e31822e94f3

33. Tang H, Psota P, Rosowski JJ, Furlong C, Cheng JT (2021) Analyses of the tympanic membrane impulse response measured with high-speed holography. Hear Res 410:108335. https://doi.org/10.1016/j.heares.2021.108335

34. Wang X (2019) Finite-element modelling of the human middle ear based on X-ray micro-computed tomography and Doppler optical coherence tomography in the same ear. McGill University, Master’s

35. Klein T, Huber R (2017) High-speed OCT light sources and systems. Biomed Opt Express 8:828–859. https://doi.org/10.1364/BOE.8.000828

36. Geuzaine C, Remacle J-F (2009) Gmsh: A 3-D finite element mesh generator with built-in pre- and post-processing facilities. Int J Numer Methods Eng 79:1309–1331. https://doi.org/10.1002/nme.2579

37. Kwacz M, Rymuza Z, Michałowski M, Wysocki J (2015) Elastic properties of the annular ligament of the human stapes–AFM measurement. J Assoc Res Otolaryngol JARO 16:433–446. https://doi.org/10.1007/s10162-015-0525-9

38. Homma K, Du Y, Shimizu Y, Puria S (2009) Ossicular resonance modes of the human middle ear for bone and air conduction. J Acoust Soc Am 125:968–979. https://doi.org/10.1121/1.3056564

39. Funnell WRJ, Golabbakhsh M (2022) Supplementary files for Golabbakhsh et al. (2023). https://doi.org/10.5683/SP3/8BEY4N. Accessed 31 Dec 2022

40. Gyo K, Aritomo H, Goode RL (1987) Measurement of the ossicular vibration ratio in human temporal bones by use of a video measuring system. Acta Otolaryngol (Stockh) 103:87–95. https://doi.org/10.3109/00016488709134702

41. Koike T, Wada H, Kobayashi T (2002) Modeling of the human middle ear using the finite-element method. J Acoust Soc Am 111:1306–1317

42. Cheng JT, Ghanad I, Remenschneider A, Rosowski J (2021) The onset of nonlinear growth of middle-ear responses to high intensity sounds. Hear Res 405:108242. https://doi.org/10.1016/j.heares.2021.108242

43. Sun Q, Gan RZ, Chang K-H, Dormer KJ (2002) Computer-integrated finite element modeling of human middle ear. Biomech Model Mechanobiol 1:109–122. https://doi.org/10.1007/s10237-002-0014-z

44. Coker NJ (1993) Surgical anatomy of the temporal bone. Head&Neck 15:586–587

45. Monroy GL, Shelton RL, Nolan RM, Nguyen CT, Novak MA, Hill MC, McCormick DT, Boppart SA (2015) Noninvasive depth-resolved optical measurements of the tympanic membrane and middle ear for differentiating otitis media. Laryngoscope 125:E276–E282. https://doi.org/10.1002/lary.25141

46. Kuypers LC, Decraemer WF, Dirckx JJJ (2006) Thickness distribution of fresh and preserved human eardrums measured with confocal microscopy. Otol Neurotol 27:256–264. https://doi.org/10.1097/01.mao.0000187044.73791.92

47. De Greef D, Aernouts J, Aerts J, Cheng JT, Horwitz R, Rosowski JJ, Dirckx JJJ (2014) Viscoelastic properties of the human tympanic membrane studied with stroboscopic holography and finite element modeling. Hear Res 312:69–80. https://doi.org/10.1016/j.heares.2014.03.002

48. Volandri G, Di Puccio F, Forte P, Carmignani C (2011) Biomechanics of the tympanic membrane. J Biomech 44:1219–1236. https://doi.org/10.1016/j.jbiomech.2010.12.023

49. Elkhouri N, Liu H, Funnell WRJ (2006) Low-frequency finite-element modeling of the gerbil middle ear. JARO 7:399–411. https://doi.org/10.1007/s10162-006-0055-6

50. Hoffstetter M, Schardt F, Lenarz T, Wacker S, Wintermantel E (2010) Parameter study on a finite element model of the middle ear. Biomed Tech 55:19–26. https://doi.org/10.1515/bmt.2010.006

51. Willi UB, Ferrazzini MA, Huber AM (2002) The incudo-malleolar joint and sound transmission losses. Hear Res 174:32–44. https://doi.org/10.1016/s0378-5955(02)00632-9

52. Willi UB, Ferrazzini MA, Huber AM (2003) Corrigendum to ‘The incudo-malleolar joint and sound transmission losses’. Hear Res 177:123.

53. Motallebzadeh H, Puria S (2021) Mouse middle-ear forward and reverse acoustics. J Acoust Soc Am 149:2711–2731. https://doi.org/10.1121/10.0004218

54. Wada H, Kobayashi T (1990) Dynamical behavior of middle ear: Theoretical study corresponding to measurement results obtained by a newly developed measuring apparatus. J Acoust Soc Am 87:237–245. https://doi.org/10.1121/1.399290

55. Kirikae I (1960) The structure and function of the middle ear. University of Tokyo Press, Tokyo

56. Speirs AD, Hotz MA, Oxland TR, Häusler R, Nolte LP (1999) Biomechanical properties of sterilized human auditory ossicles. J Biomech 32:485–491. https://doi.org/10.1016/s0021-9290(99)00012-3

57. Homma K, Shimizu Y, Kim N, Du Y, Puria S (2010) Effects of ear-canal pressurization on middle-ear bone- and air-conduction responses. Hear Res 263:204–215. https://doi.org/10.1016/j.heares.2009.11.013

Preface to Chapter 5

This chapter describes the finite-element modelling of human ears with pathology as well as normal ears. One of the models in Chapter 4 was used as the base model and was updated according to each pathological condition, and the simulation results were classified. We generated large sets of data by changing eight parameters of the FE models to simulate inter-ear variability. We changed parameters that had the largest effects on the model behaviour according to the parameter sensitivity analysis in Chapter 4.

This chapter suggests a classification method to distinguish normal ears from pathological ears. Section 4.1 provides an introduction to OCT and computational modelling of pathological ears. Section 4.2 presents the methods for building pathological models, creating large sets of data, and classifying the simulation results. In section 4.3, the results of the models are compared to the experimental measurements from previous studies. Section 4.3 also includes the results of the classification of normal and pathological ears. Section 4.4 includes a discussion of the results, some additional findings, and future work.

Chapter 5. Use of simulated data to explore the application of optical coherence tomography for classifying middle-ear pathologies

Journal of the Acoustical Society of America 154 (5): 2790–2799 (2023)

Abstract

Optical coherence tomography (OCT) vibrometry is a non-invasive tool for functional imaging of the middle ear. It provides spatially resolved vibrational responses and also anatomical images of the same ear. Our objective here was to explore the potential of OCT vibration measurements at the incus, as well as at the umbo, to distinguish among middle-ear disorders. Our approach was to build finite-element models of normal and pathological ears, generate large amounts of synthetic data, and then classify the simulated data into normal and pathological groups using a decision tree based on features extracted from simulated vibration magnitudes. We could distinguish between normal ears and ears with incudomallear joint (IMJ) disarticulation or stapes fixation, with the sensitivity and specificity both being 1.0; distinguish between stapes fixation and IMJ disarticulation with a sensitivity of 0.900 and a specificity of 0.889; and distinguish ears with ISJ disarticulation from normal ears with a sensitivity of 0.784 and a specificity of 0.872. Less extreme pathologies were also simulated. The results suggest that the vibration measurements within the middle ear that can be provided by OCT (e.g., at the incus) may be very valuable for diagnosis.

5.1 Introduction

Hearing loss is very prevalent, affecting more than 1.5×10^9 people globally, including almost two-thirds of persons over the age of 60 years (World Health Organization, 2021). Unaddressed hearing loss has many negative effects, and leads to high costs for health-care systems. New technologies that improve diagnostic accuracy and efficacy are sought.

Optical coherence tomography (OCT) vibrometry is a promising tool for functional imaging of the middle ear. It is based on low-coherence interferometry, typically with near-infrared light. It is a non-invasive means of obtaining spatially resolved vibrational responses and also anatomical images. Such information can potentially improve diagnostic sensitivity and specificity as compared to current approaches. A recent technical review by Ramier et al. (2018) describes the history of OCT for imaging the middle ear and inner ear. Most middle-ear disorders involve fixations or discontinuities at specific locations within the ossicular chain (e.g., Park et al., 2014) and the ability to measure both function and anatomy will help in finding the precise location of the pathology.

A computational model can simulate how different parts of the middle ear behave mechanically under different loads. Such models can be used to simulate pathological conditions and to assess how the pathologies will affect middle-ear function. In finite-element (FE) models in particular (e.g., Daniel et al., 2001; Huber et al., 2003; Dai et al., 2007), pathologies can be simulated by changing the material properties and boundary conditions of the model in ways that are directly related to the nature of the pathology. For example, increasing the stiffness parameter of the stapedial annular ligament (SAL) can be used to simulate stapes fixation. We can also add or remove material or otherwise modify parts of the models.

Pathologies at different locations can best be characterized by considering vibrations at multiple points in the ossicular chain. While laser Doppler vibrometry (LDV) measurements can be made at middle-ear locations behind the tympanic membrane (TM) in cadaver temporal bones, in patients, they can only be made at the level of the TM, and not deeper. Recently, OCT Doppler vibrometry (OCT-DV) has been able to provide deep vibration measurements in temporal bones and patients. For example, MacDougall et al. (2019) used OCT vibration measurements in patients to distinguish patients with stapes fixation from normal controls and they concluded that "OCT-DV alone can achieve sensitivity and specificity higher than combined audiometry and LDV." [Another issue with LDV is its dependence on the presence of a naturally reflective bright spot on the TM, the light reflex, which is missing in some patients because of normal anatomical differences (Merchant, 2014, p. 49).]

In a previous study (Golabbakhsh et al., 2023), we reported three FE models that were built based on geometries obtained from micro-scale X-ray computed tomography (microCT) images of normal middle ears and validated against OCT vibration measurements in the same ears. Our objective here is to use one of those models to explore the feasibility of using OCT vibration measurements at the umbo and incus to distinguish among various disorders. We do this by modifying the model to represent pathological ears; randomly generating large amounts of normal and pathological synthetic data; and then using a decision tree to classify the synthetic data into groups of normal ears and ears with different disorders.

5.2 Methods

One of the three FE middle-ear models (2017-2) of Golabbakhsh et al. (2023) was used in this study (see Funnell and Golabbakhsh, 2022 for the model definition). We had microCT and OCT data for the same ear, recorded at Dalhousie University in Halifax, Canada. As described in

Golabbakhsh et al. (2023), the microCT images were segmented manually using locally developed software (audilab.bme.mcgill.ca/sw), which was also used to specify the material properties, boundary conditions, and acoustic loads, and for the generation of triangulated surfaces. The volume mesh generation was done with Gmsh (Geuzaine and Remacle, 2009). The model (Fig. 5.1) included the following separate structures: pars tensa (PT) and pars flaccida (PF) of the TM, TM-malleus connection (TMMC), malleus, incus, stapes, incudomallear joint (IMJ), and incudostapedial joint (ISJ). The SAL was represented by discrete springs. The value of the stiffness of the SAL was taken from Kwacz et al. (2015). Given that the highest frequency of interest was 3 kHz, the anterior mallear ligament (AML) and posterior incudal ligament (PIL) were not modelled. Instead, we implemented a practically fixed axis of rotation by using very stiff springs. Experiments have shown that the axis of rotation is almost fixed at low frequencies (Gundersen and Høgmoen 1976) so the results up to 3 kHz are not expected to change much. Since the contrast of the microCT images was inadequate for segmentation of soft-tissue structures, histological images of human ears were used as a supplement. Detailed specifications of the FE model were given in Golabbakhsh et al. (2023).

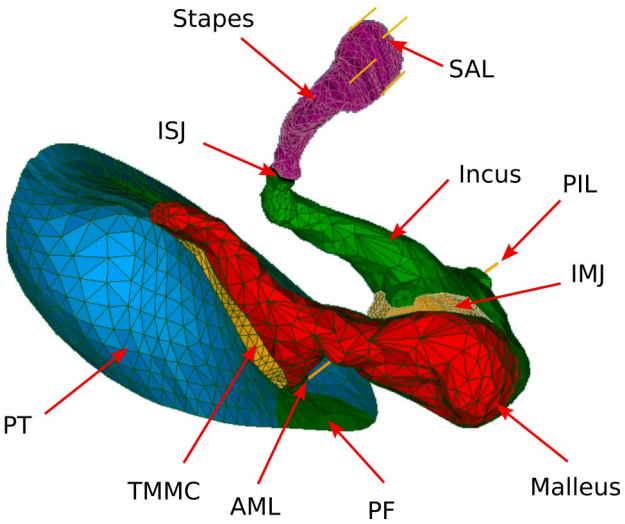

Figure 5.1. (Color online) Finite-element model of the human ear. PT, pars tensa; PF, pars flaccida; TMMC, TM-malleus connection; IMJ, incudomallear joint; ISJ, incudostapedial joint; SAL, stapedial annular ligament; AML, anterior mallear ligament; PIL=posterior, incudal ligament. Straight yellow lines indicate the attachment points of the ASL, AML and PIL.

Code_Aster 14.6 (code-aster.org) was used for FE analysis. We used the high-performance computing resources of the Digital Research Alliance of Canada. In particular, we used Narval, a heterogeneous multi-purpose cluster consisting of a mix of AMD EPYC Rome and Milan processors (Advanced Micro Devices, Inc., Santa Clara, CA) connected by a Mellanox HDR InfiniBand network (NVIDIA, Santa Clara, CA) (https://docs.alliancecan.ca/wiki/Narval/en). Each 64-core Rome processor can theoretically perform up to about 2.5×10^{12} double-precision floating-point operations (FLOPs) per second. [However, interpreting the performance of modern processors in terms of FLOP/s is not straightforward (e.g., Dolbeau, 2018).] We ran multiple simulations in Code_Aster simultaneously using Slurm (www.schedmd.com) job arrays, each containing 1000 jobs, the maximum number allowed for one job array on Narval. Each job in the job array ran the simulation for one combination of model parameters. We specified a

maximum of 20 min for each job array, one central processing unit (CPU) per task, and 1 GB of memory per CPU. Each job takes about 20 to 30 s of wallclock time.

The previous FE model of a normal ear was altered by changing the material properties and boundary conditions linked to the causes of three different middle-ear pathologies: stapes fixation, disarticulation of the ISJ, and disarticulation of the IMJ. We took the parameters related to each pathology from Sackmann et al. (2022). For the simulation of stapes fixation, the baseline stiffness of the SAL was set to 1000 times the value for the normal case. For the simulation of disarticulation of each of the joints (IMJ and ISJ), the stiffness and the loss ratio of the joint were both set to zero.

We created synthetic data incorporating inter-ear variability by varying eight parameters of the model for the normal case and the pathological cases: thickness and Young's modulus of PT, Young's modulus of IMJ and ISJ, stiffness of SAL, loss ratio of soft tissues, and cochlear damping. For the loss ratio and cochlear damping, we randomly took either the baseline value or a value that was multiplied or divided by a factor of 1.5 or 1.2. To set the other parameters for each simulation, we used the same method but factors of 3 and 1.5 were used. Table 5.1 shows the baseline values of the parameters for the normal and pathological cases.

The OCT vibration measurements in Golabbakhsh et al. (2023) were made only at 500, 1000, and 2000 Hz. In this study, however, we explored more frequencies, calculating simulated displacement magnitudes at 11 frequencies with an equal interval of 250 Hz, from 500 to 3000 Hz.

Table 5.1. Model material properties. (Values in parenthesis refer to less extreme versions of the pathologies, as discussed in the text.)

Parameter	Baseline model	IMJ diasarticulation	ISJ diasarticulation	Stapes fixation
PT Young's modulus	10 MPa	—	—	—
PT thickness	40 μm	—	—	—
IMJ Young's modulus	7 MPa	0 (7 kPa)	—	—
IMJ loss ratio	0.2	0	—	—
ISJ Young's modulus	6 MPa	—	0	—
ISJ loss ratio	0.2	—	0	—
TMMC Young's modulus	2 MPa	—	—	—
SAL stiffness	120 N/m	—	—	120,000 N/m (12000)
Loss ratio	0.2	—	—	—
Cochlear damping	0.05	—	—	—

5.3 Results

Figure 5.2 shows violin plots of the displacement magnitude at the umbo at frequencies from 500 Hz to 3 kHz, for normal ears and for the three different disorders, along with values of displacement magnitude at the umbo from previous *in vivo* studies (Rosowski et al., 2012; Merchant, 2014; Farahmand et al., 2016; Masud, 2020) and from the temporal-bone study of Cheng et al. (2021), which all included frequencies from 300 to 6000 Hz. The curves for baseline models are presented on top of the violin plots. The baseline models have parameter values in the middles of their ranges of variation but their displacements are not always in the middles of the violin plots, reflecting the bias noted by Ebrahimian et al. (2023b). In addition, the plots are not unimodal, which suggests that there are parameter interactions in the model. The parameters vary independently and any interactions among the parameters will be reflected in the distributions of the simulated data. We can see that the magnitudes are higher for the *in vivo* measurements than

for our simulation results, possibly because our normal model was validated against OCT measurements in temporal bones. The normal temporal-bone measurements of Cheng et al. (2021) that are presented in Figure 5.2(a) are consistent with our baseline model results. The plot shows that the frequency responses of our baseline model fall faster at high frequencies compared with the experimental data. As discussed in Golabbakhsh et al. (2023), we think this might be because we have not modelled the suspensory ligaments and instead have a fixed axis of rotation.

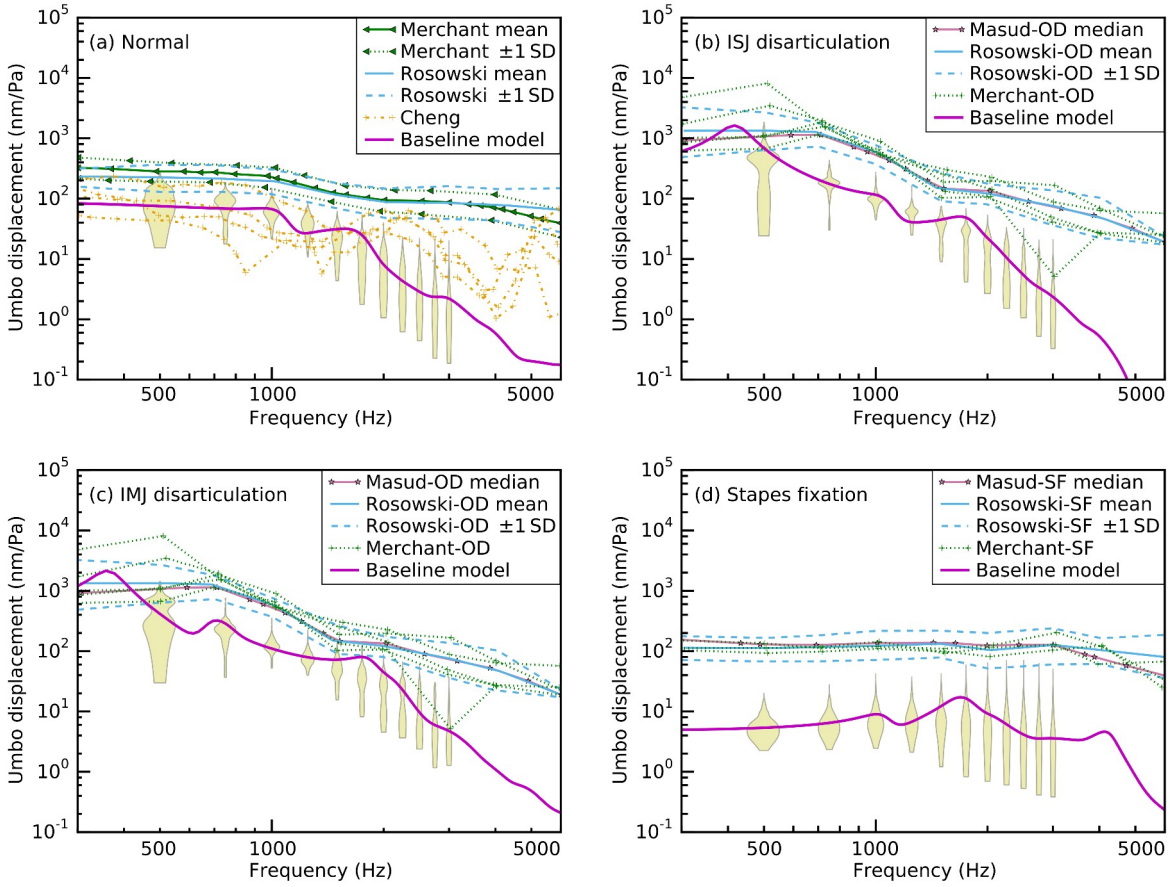

Figure 5.2. Violin plots for the umbo displacement magnitudes (nm/Pa) for sets of 1000 simulations and curves for baseline models and from previous in vivo *studies (Rosowski et al. 2012; Merchant 2014; Masud 2020) and from the temporal-bone study of Cheng et al. (2021). (a) Normal, (b) ISJ disarticulation, (c) IMJ disarticulation, (d) Stapes fixation.*

In spite of the differences in the displacements themselves, the displacement changes due to the simulated pathologies in our results are in qualitative agreement with experimentally measured

changes in normal subjects and patients. For ossicular discontinuity, Merchant (2014, Figure 2.8a) reported an increase in the umbo displacement magnitude below 1 kHz by factors of about 2 to about 15 in five of six patient ears, but a decrease by a factor of about 2.5 for the one ear that had a "round-shaped tympanogram, consistent with a middle-ear system stiffer than normal." Farahmand et al. [2016, Fig. 2(b)] reported that 21 of 29 patients with ossicular discontinuity showed values larger than normal by a factor of between 3 and 4 at frequencies below 1 kHz. In our simulated data, we see an increase by more than a factor of 5 below 1 kHz for both ISJ and IMJ disarticulation [Figure 5.2(b) and 5.2(c)], but there is little change at higher frequencies. For stapes fixation, Merchant (2014, Figure 2.7a) reported a decrease by a factor of 5 to 8 for the displacement magnitude at frequencies below 1 kHz in four of five patient ears, but an increase by a factor of around 4 for the remaining ear (which had a normal tympanogram). We see a decrease by factors of about 10 for our models of stapes fixation below 2 kHz [Figure 5.2(d)].

Figure 5.3 shows plots of umbo vibration magnitudes against the vibration magnitudes of the long process of the incus at six different frequencies (500 Hz, 750 Hz, 1 kHz, 1.5 kHz, 2 kHz, 3 kHz) for 1000 simulations for normal ears and 1000 simulations for each category of pathological ears, to give an overview of the simulation results. Each panel shows 4000 simulation results (1000 simulations for each middle-ear case). (At 500 and 750 Hz for stapes fixation, the umbo and incus displacements were both very small for all of the simulations; therefore, the results overlap substantially, which is why there seem to be only a few stars.) The incus-vs-umbo displacement plots for different pathological conditions appear as roughly linear for each condition, with a different slope in each case. We see that when the frequency increases, the categories become more scattered but are still separable to some extent. As discussed below, the variability at the higher frequencies is probably a result of the increasing complexity of the

three-dimensional (3D) motions of the middle ear and the increasing irregularity of the responses in the frequency domain (e.g., Decraemer and Khanna, 2004; Maftoon et al., 2015). We concluded from these plots that there was potentially useful diagnostic information in the ratio of the displacement magnitude at the incus to that at the umbo.

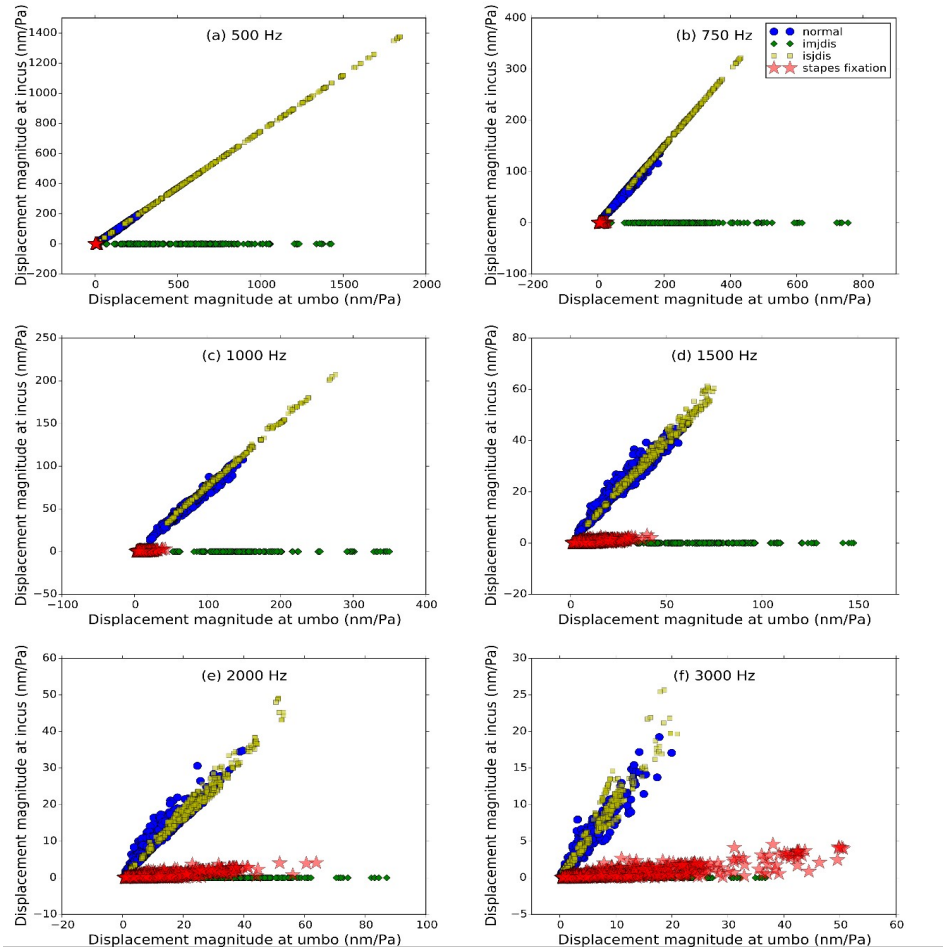

Figure 5.3. (Color online) Incus vibration magnitudes vs umbo vibration magnitudes for simulated normal ears. Each panel shows 4000 simulation results (1000 simulations for each middle-ear case).

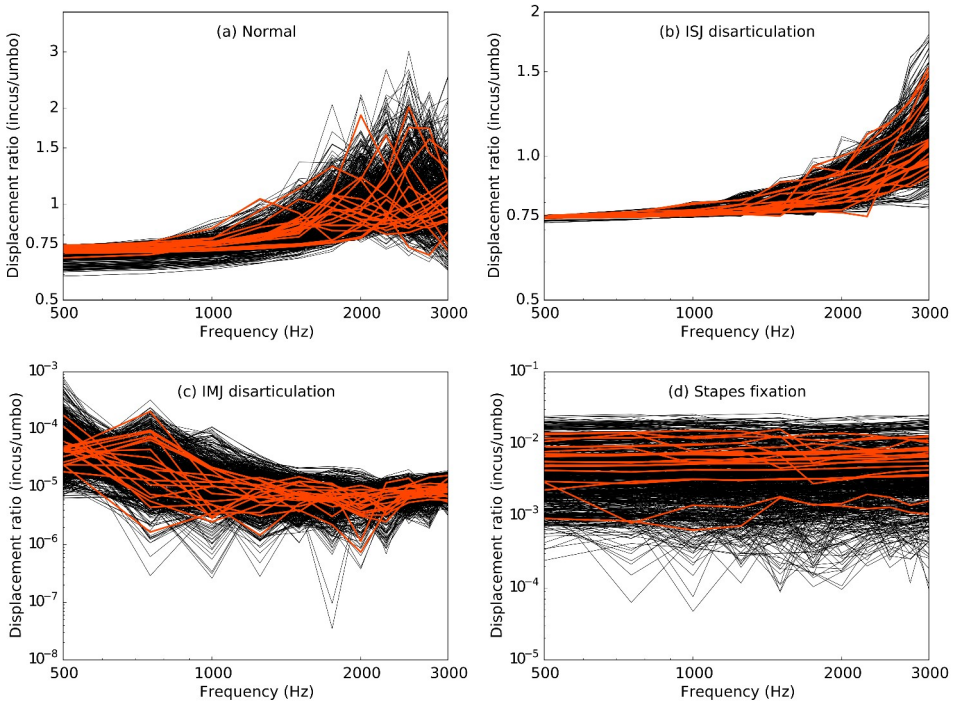

Figure 5.4. (Color online) Ratio of displacement magnitude at the incus to that at the umbo, vs frequency, for the simulations of Figure 3.

Figure 5.4 shows the ratios of the vibration magnitudes at the incus to those at the umbo as functions of frequency for the initial set of 1000 simulations. Each curve corresponds to an individual simulation with different model parameter values. To clearly show the shapes of some individual curves, the lighter curves (red online) show 20 randomly selected curves. The rest of the 1000 curves are shown in black. Note that the vertical scales are different from panel to panel. We see that, in the normal and ISJ disarticulation cases, the frequency response is fairly constant at lower frequencies but increases at higher frequencies, while in the IMJ disarticulation cases there is the opposite trend. In the stapes fixation cases, the curves are more flat and more or less independent of frequency. The ratio of incus displacement to umbo displacement was always less than 1 in the normal-ear OCT measurements of Golabbakhsh et al. (2023). However, we see in Figure 5.4(a) that sometimes the simulated ratio is greater than 1. This is relatively rare for frequencies up to 2000, which was the highest frequency of the normal-ear OCT measurements

in Golabbakhsh et al. (2023), but it happens more often at higher frequencies as the ossicular motions become more complicated (e.g., Decraemer and Khanna, 2004).

Figure 5.5 shows violin plots for the results in Figure 5.4. We see that the value of the ratio is below 0.3 for the stapes fixation simulations at all frequencies and is always below 0.01 for the IMJ disarticulation simulations, while the ratio is always higher than 0.5 for the normal simulations and higher than 0.6 for the ISJ disarticulation simulations. We have used this fact in the first branch of the decision tree (Figure 5.6), adopting a threshold value of 0.5, which classifies all of the samples correctly.

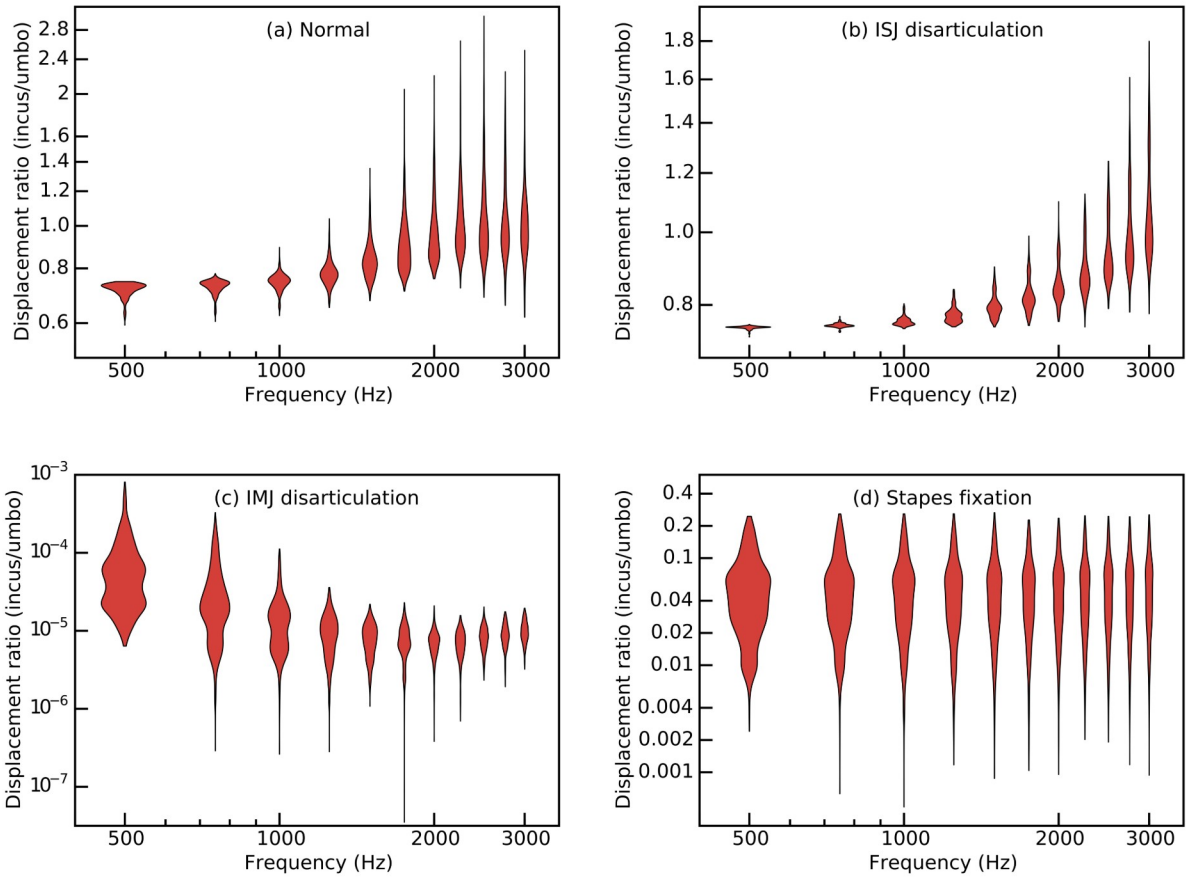

Figure 5.5. (Color online) Violin plots of ratio of displacement magnitude at the incus to that at the umbo, at multiple frequencies, for the simulations of Figure 4. (a) Normal, (b) ISJ disarticulation, (c) IMJ disarticulation, (d) stapes fixation.

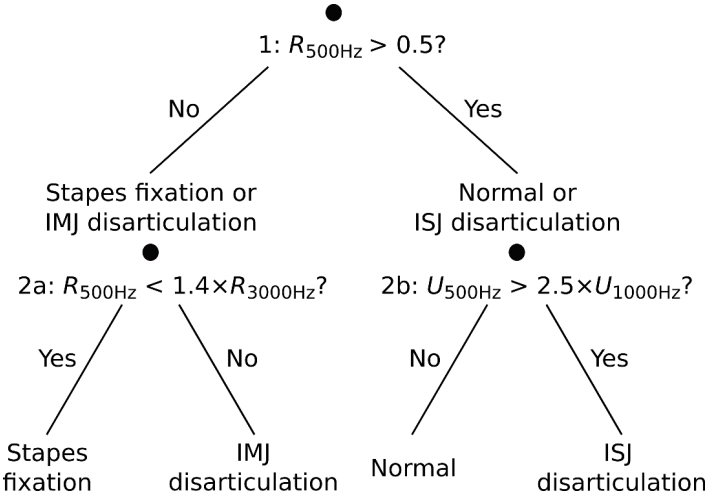

Figure 5.6. Decision tree to distinguish between normal and pathological middle ears, R*, ratio of displacement magnitude at the incus to that at the umbo;* U*, umbo displacement magnitude.*

For distinguishing IMJ disarticulation from stapes fixation, we considered how the value of the ratio changes with frequency in the two cases. In the IMJ disarticulation simulations, the ratio is higher at lower frequencies (500 and 750 Hz) for about 85% of the curves, while in the stapes fixation simulations there was no definite trend across frequencies. Therefore, branch 2a of the decision tree was based on whether the ratio at 500 Hz is less than k_1 times the ratio at 3 kHz.

For distinguishing ISJ disarticulation from normal, we considered how the value of the umbo displacement changes with frequency in the two cases. In the ISJ disarticulation simulations, the umbo displacement was higher at 500 Hz than at 1 kHz while in normal simulations we did not find this trend. Therefore, branch 2b of the decision tree was based on whether the umbo displacement at 500 Hz is more than k_2 times the umbo displacement at 1 kHz.

A receiver operating characteristic (ROC) curve is a plot of a true positive rate (sensitivity) against a false positive rate (1 − specificity). It shows the performance of a binary classifier as its discrimination threshold is varied. Figure 5.7 shows the ROC curves for branches 2a and 2b of

the decision tree, with triangles indicating selected values of k_1 between 0.8 and 10 and squares showing selected values of k_2 between 1.5 and 4. We defined the optimal point as the point minimizing the Euclidean distance between the ROC curve and the point (0,1) of the diagram. A value of k_1 =1.4 was chosen, which gives a sensitivity of 0.904 and a specificity of 0.886 for branch 2a, and a value of k_2 =2.5 was chosen, which gives a sensitivity of 0.787 and a specificity of 0.836 for branch 2b. We investigated the phase values and they did not appear to add information that would help to discriminate the conditions.

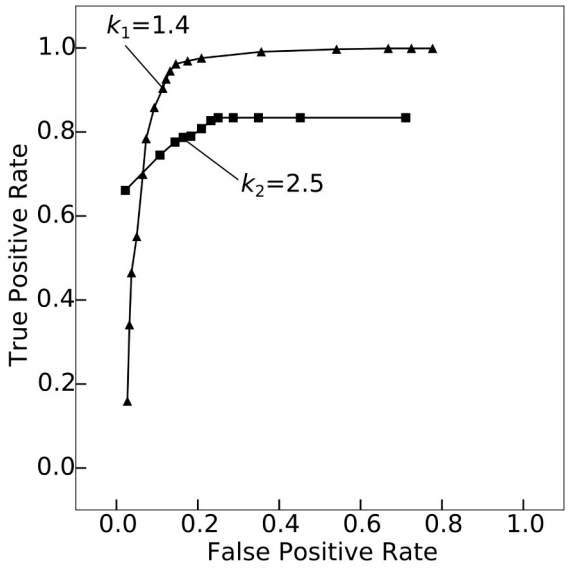

Figure 5.7. Receiver operating characteristic (ROC) curves for the k_1 *and* k_2 *thresholds at the second level of the decision tree.*

To validate the decision tree, we generated four more sets of 1000 simulations for each of the four conditions. We found that the sensitivity and specificity remained the same within ±0.04 among the five sets, so we concluded that the decision tree could be based on the first set of 1000 simulations for each of the four conditions.

We tested the classifier for a set of 5000 additional simulations for each of the four conditions. The first branch of the decision tree again had a sensitivity and a specificity of 1, and we obtained a sensitivity = 0.900 and a specificity = 0.889 when distinguishing IMJ disarticulation from stapes fixation (Table 5.2), within 0.004 of the initial results. We obtained a sensitivity = 0.784 and a specificity = 0.872 when distinguishing ISJ disarticulation from normal, within 0.04 of the initial results.

Table 5.2. Classification results for different conditions

Condition	**Sensitivity**	**Specificity**
Extreme, branch 1	1.000	1.000
Extreme, branch 2a	0.900	0.889
Extreme, branch 2b	0.784	0.872
Partial IMJ disarticulation, branch1	1.000	0.926
Partial IMJ disarticulation, branch 2a	0.904	0.733
Partial stapes fixation, branch 1	1.000	0.932
Partial stapes fixation, branch 2a	0.996	0.886

For the results so far, we have considered extreme pathological cases, with factors of zero for the joint disarticulations and 1000 for the stapes fixation. However, sometimes there may be a partial disarticulation or a partial fixation, and some patients with partial disarticulations are mistakenly diagnosed as having sensorineural hearing loss (Masud, 2020, p. 5). To see how the classifier works for a partial disarticulation of the IMJ, we simulated a set of 1000 ears with Young's modulus values different from zero for the IMJ: instead of using zero, the baseline value was divided by 1000. [By comparison, although Hirabayashi et al. (2022) did not model IMJ disarticulation, for ISJ disarticulation, they used Young's moduli for the ISJ of 5, 10, 100, and 1000 times smaller than the value for the normal ear.] The same multipliers as for the extreme pathological cases (1.5 and 3) were applied to produce variability. We used the same k_1 value as for the extreme simulated pathologies to evaluate the performance of the classifier when there

are different degrees of pathology that are not known *a priori*. Figure 5.8(b) shows the violin plots for the ratio of the vibration magnitude at the incus to that at the umbo for this set of 1000 simulations. For comparison, Figure 5.8(a) shows the corresponding plots with the IMJ Young's modulus set to zero. Note that the range of the displacement scale in panel b is 500 times larger than that of panel a. While the heights of the violin plots get smaller with increasing frequency in panel a, the pattern is not so regular in panel b. Between 750 and 1250[2] Hz there are more cases higher than 0.5, but most of the cases are still below 0.5. The first level of the decision tree now gives a sensitivity of 1 and a specificity of 0.926 (compared to 1 and 1 when the IMJ Young's modulus = 0), while the second level now gives a sensitivity of 0.904 and a specificity of 0.733 (compared to 0.900 and 0.889 when the IMJ Young's modulus = 0).

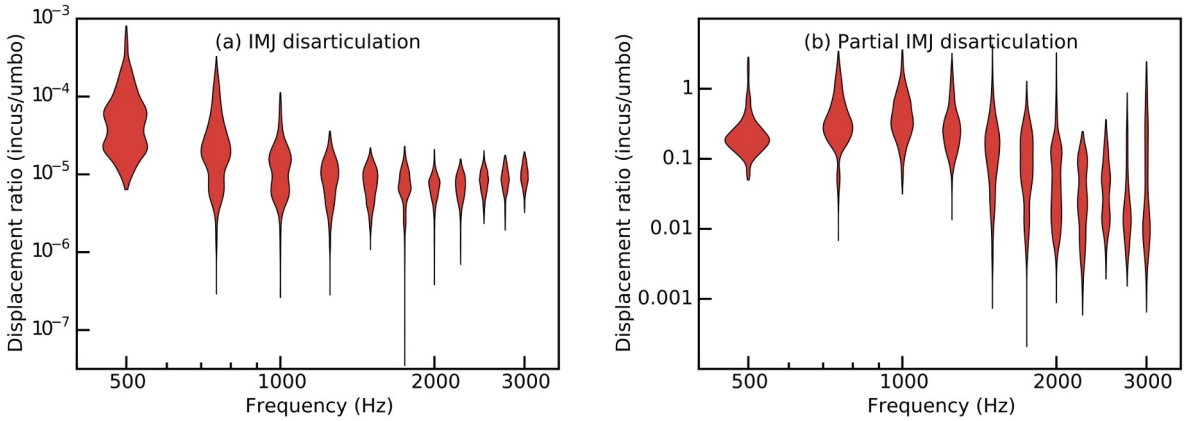

Figure 5.8. (Color online) Violin plots of ratio of displacement magnitude at the incus to that at the umbo, at multiple frequencies. (a) Extreme IMJ disarticulation, (b) partial IMJ disarticulation.

We also simulated a set of ears with a less extreme stapes fixation, with the SAL stiffness taken to be 100 times that of the normal case, rather than 1000 times as was done above. [By comparison, for simulating stapes fixation, Hirabayashi et al. (2022) used Young's moduli for the SAL of 5, 10, 100 and 1000 times the value for the normal ear.] Figure 5.9b shows the violin

2 1250 was incorrectly changed to 250 in the published paper.

plots for this case and we can see that the incus/umbo displacement ratio is larger than the previous results [Figure 5.9(a)] by a factor of about 6. As the frequency increases, the displacement magnitudes increase and there are fewer outliers. The first level of the decision tree now gives a sensitivity of 1 and a specificity of 0.932 (compared with 1 and 1 before) while the second level gives a sensitivity of 0.996 and specificity of 0.886 (compared with 0.900 and 0.889 before).

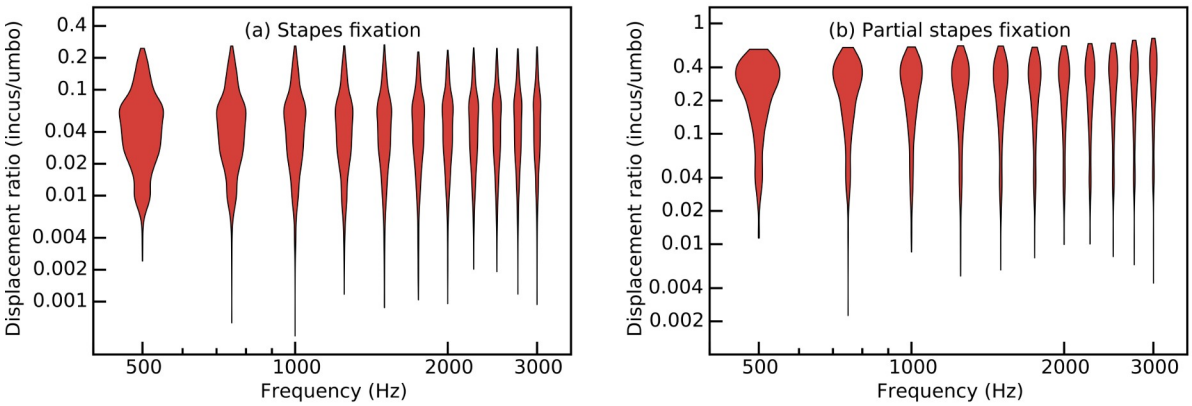

Figure 5.9. (Color online) Violin plots of ratio of displacement magnitude at the incus to that at the umbo, at multiple frequencies. (a) Extreme stapes fixation, (b) Partial stapes fixation.

We did not simulate ears with partial ISJ disarticulation, because the sensitivity and specificity values for distinguishing between extreme ISJ disarticulation and the normal case were already below 0.9.

For the partial IMJ disarticulation and the partial stapes fixation, for the second level of the decision tree, the specificity decreases by 0.156 and 0.003, respectively. The sensitivity, however, increases, by only about 0.004 for partial IMJ disarticulation but by 0.096 for stapes fixation. The relatively higher sensitivity for partial stapes fixation is because the frequency response of the partial stapes fixation rises at higher frequencies and better fits our decision criterion that the ratio at 500 Hz is smaller than $k_1 = 1.4$ times the ratio at 3000 Hz.

5.4 Discussion

We have explored using simulations of OCT vibration measurements at the umbo and incus in a decision tree to aid in distinguishing among normal and pathological conditions in the middle ear. In general, we aimed for a minimal set of features for classification. For one thing, we wanted to reduce the data-acquisition requirements and the computational cost if the classifier was used clinically. For another thing, we wanted a method that is easy to explain to clinicians, to encourage its use in clinical decision making. Decision trees provide a simple and transparent model and are not computationally expensive. They can analyze a large amount of data quickly and help in efficient and accurate clinical decision making. In a previous application to the middle ear, Masud (2020, Chap. 4) used a decision tree to classify normal, ossicular discontinuity and stapes fixation based on measurements of wideband acoustic immitance and the air-bone gap (ABG) in patients.

We found potential discriminants for the purpose of distinguishing among simulated normal ears and ears with simulated stapes fixation and ossicular joint disarticulation. Finding the best discriminants based on simulation results will help future experimental and clinical researchers to decide what might be the most important measurement quantities, locations and frequencies. Since only a limited number of frequencies can be tested clinically using OCT due to time limitations, in this work we wanted to identify a few frequencies that could best discriminate among the different conditions. Based on our results so far, we suggest that recording of the umbo and incus vibrations be done at both low and mid frequencies (e.g., 500 Hz and 3 kHz) in order to distinguish among the disorders considered here. We have presented simulation results up to 6 kHz in Figure 5.2 but we have focused on frequencies only up to 3 kHz because our existing OCT data were limited to low frequencies. This limitation was a result of noise from fans in the laser unit in the current design, and we expect that subsequent designs will be able to

reach much higher frequencies, as has been done by other groups (e.g., Kim et al., 2019). The use of higher frequencies should provide additional information to aid in diagnosis, complicated by the fact that the 3D motions of the ossicles become more complex at high frequencies and OCT currently measures only the vibration component in the direction of the laser beam (which is approximately parallel to the axis of the ear canal and to the piston direction of the stapes).

So far, we have not considered the actual prevalences of the clinical pathologies in calculating the sensitivity and specificity. In addition, we have assigned the same relative cost to false positives and false negatives when choosing the threshold based on the ROC curve.

Our models were based on OCT measurements in cadaver ears, while clinical OCT measurements will obviously be performed *in vivo*. The TM and the middle ear as a whole are known to get stiffer *post mortem* as they dry (e.g., Kirikae, 1960, p. 47; Ellaham, 2007, p. 29). On the other hand, Rosowski et al. (1990, Table 1 and Fig. 10) found that, for 12 of their 15 cadaver ears, the acoustic input impedance varied by a factor of 2.6 and the range was almost the same as in earlier measurements in living ears. (In the other three cadaver ears, the impedance was beyond that range by a factor of about 2.). Their 15 temporal bones were extracted “from refrigerated (3°C) human cadavers within 48 hours after death” and were either used “immediately” or “wrapped in wet gauze and stored in a freezer at −10°C to −15°C”; during measurements, the middle ears were kept “moist” by “periodic” rinsing of the ear canal with saline and then using “gentle suction … to remove all excess fluid”; and the middle-ear air pressure was kept at ambient pressure. Also, Goode et al. (1993) reported seeing similar umbo displacements in cadaver ears and living ears: at 500 Hz, the displacements varied by factors of about 7 and 6, respectively, and the ranges were almost the same. Their 15 “fresh” temporal bones were extracted “within 48 hours after death”, kept in a merthiolate solution at 5°C, and

used “within 6 days after death” (Goode et al., 1993). The temporal bones used in our study were fresh frozen, and Rosowski et al. (1990) found that freezing and thawing in three ears had an effect of generally less than 40% on the impedance below 1 kHz and up to a factor of about 5 at frequencies beyond 1 kHz in two ears; the other ear had small changes at all frequencies.

Merchant (2014) and Masud (2020) did not separate ISJ and IMJ disarticulations, and instead just used ossicular discontinuity as a single category. It is important to distinguish them because the treatments will be different (e.g., what kind of implant will be used) and we analyzed them separately. To improve the classification results, it may be necessary to include data from clinical tests like the ABG, and possibly data from the medical history, along with the vibration measurements. It might also be useful to use the improvement of hearing after the Valsalva manoeuvre, which has been reported to be related to ISJ disarticulation (Sim et al., 2013). Synthetic clinical data could be generated to supplement the synthetic vibration data to test this approach, as done by Hirabayashi et al. (2022) for the ABG, for example.

Masud (2020, Chap. 5) used the random-forest method to detect superior canal dehiscence. They suggested that the method could reach a higher sensitivity and specificity than Merchant et al. (2015) had obtained using a decision tree for detecting this disorder. This was because Merchant et al. also[3] had a problem with overfitting and the random-forest method helps to avoid overfitting by combining the predictions of an ensemble of decision trees. Supervised learning methods, such as *k*-nearest neighbours, support vector machines and neural networks, which work more automatically, can also be investigated. The discriminants identified by these more sophisticated methods may not have a straightforward physiological relevance to a pathology, and they thus may make discussions about differences among the disorders difficult. However, they might help with improving our performance in detecting ISJ disarticulation. If *in vivo*

3 The word ‘also’ appeared here in the published paper but is incorrect.

human OCT measurements can provide stapes displacements in the future, this would be helpful in better distinguishing ISJ disarticulation from the normal case. For example, in a study on cadaver chinchillas, Chang et al. (2013) were able to distinguish ISJ disarticulation from the normal case using OCT measurements of umbo, incus, and stapes.

It is difficult to know what values of stiffness to use for the IMJ, ISJ, and SAL to represent ears with hearing disorders. We initially selected the parameters related to each pathology following Sackmann et al. (2022), and then also looked at the effects of using less extreme values. The ranges of normal values for the stiffnesses of the ligaments are uncertain. For example, SAL stiffness values have varied by a factor of 10 across different studies, as discussed by Motallebzadeh et al. (2017). Our choice of values is supported by the fact that the umbo displacement changes for our simulated pathologies matched the experimentally measured changes. Hirabayashi et al. (2022) used values of 5, 10, 100, and 1000 times the normal case for the SAL, and showed that stiffnesses of 100 and 1000 times normal gave ABG results similar to measurements from patients [their Figure 4(a)], consistent with our values. If OCT vibrometry were used to gather umbo and incus displacement measurements from subjects with different degrees of hearing loss and surgically confirmed diagnoses, it would be possible to use parameter fitting to build pathological models (e.g., using a pattern-search algorithm like that of Sackmann et al., 2022) to match those data. Then, it would be possible to develop a classifier based on the models with those fitted parameters. In Golabbakhsh et al. (2023), we performed a typical one-at-a-time parameter-sensitivity analysis, but a global sensitivity analysis (e.g., Ebrahimian et al., 2023a) would give additional insight into which parameters would most need to be included in the computationally expensive parameter fitting.

We have not considered modelling two pathologies present at the same time. It might be interesting to investigate that in the future. There are also additional pathologies that could be simulated, such as malleus fixation, incus fixation, ossicular erosion, and sclerosis of the ossicular ligaments (e.g., Daniel et al., 2001).

In this work, we have used computational models to simulate the utilization of incus vibration measurements to classify the behaviour of normal and pathological middle ears. The results suggest that the vibration measurements beyond the TM that can be provided by OCT may provide a diagnostic method that is less invasive, less costly, and faster than surgery; and that is more accurate than just using immittance or LDV measurements, since neither one can measure incus vibrations in patients, while OCT can.

5.5 Acknowledgements

This work was supported in part by the Canadian Institutes of Health Research, the Natural Sciences and Engineering Research Council of Canada, and the Faculty of Medicine and Health Sciences of McGill University. We are grateful for the help in using Narval that was provided by Calcul Québec and the Digital Research Alliance of Canada.

5.6 Author declarations

The authors have no conflicts to disclose.

5.7 Data availability

The data that support the findings of this study are openly available in Borealis at https://doi.org/10.5683/SP3/8BEY4N (Funnell and Golabbakhsh 2022).

5.8 References

Chang EW, Cheng JT, Röösli C, Kobler JB, Rosowski JJ, Yun SH (2013) Simultaneous 3D imaging of sound-induced motions of the tympanic membrane and middle ear ossicles. Hear Res 304:49–56. https://doi.org/10.1016/j.heares.2013.06.006

Cheng JT, Ghanad I, Remenschneider A, Rosowski JJ (2021) The onset of nonlinear growth of middle-ear responses to high intensity sounds. Hear Res 405:108242, 13 pp. https://doi.org/10.1016/j.heares.2021.108242

Dai C, Cheng T, Wood MW, Gan RZ (2007) Fixation and detachment of superior and anterior malleolar ligaments in human middle ear: experiment and modeling. Hear Res 230:24–33. https://doi.org/10.1016/j.heares.2007.03.006

Daniel SJ, Funnell WRJ, Zeitouni AG, Schloss MD, Rappaport J (2001) Clinical applications of a finite-element model of the human middle ear. J Otolaryngol 30:340–346

Decraemer WF, Khanna SM (2004) Measurement, visualization and quantitative analysis of complete three-dimensional kinematical data sets of human and cat middle ear. pp 3–10

Dolbeau R (2018) Theoretical peak FLOPS per instruction set: a tutorial. J Supercomput 74:1341–1377. https://doi.org/10.1007/s11227-017-2177-5

Ebrahimian A, Mohammadi H, Maftoon N (2023a) Relative importance and interactions of parameters of finite-element models of human middle ear. J Acoust Soc Am 154:619–634. https://doi.org/10.1121/10.0020273

Ebrahimian A, Mohammadi H, Rosowski JJ, Cheng JT, Maftoon N (2023b) Inaccuracies of deterministic finite-element models of human middle ear revealed by stochastic modelling. Sci Rep 13:7329. https://doi.org/10.1038/s41598-023-34018-w

Ellaham N (2007) An experimental study of middle-ear vibrations in gerbils. M.Eng. thesis, McGill University

Farahmand RB, Merchant GR, Lookabaugh SA, Röösli C, Ulku CH, McKenna MJ, de Venecia RK, Halpin CF, Rosowski JJ, Nakajima HH (2016) The audiometric and mechanical effects of partial ossicular discontinuity. Ear Hear 37:206–215. https://doi.org/10.1097/AUD.0000000000000239

Funnell WRJ, Golabbakhsh M (2022) Supplementary files for Golabbakhsh et al. (2023). https://borealisdata.ca/dataset.xhtml?persistentId=doi:10.5683/SP3/8BEY4N. Accessed 31 Dec 2022

Geuzaine C, Remacle J-F (2009) Gmsh: A 3-D finite element mesh generator with built-in pre- and post-processing facilities. Int J Numer Methods Eng 79:1309–1331. https://doi.org/10.1002/nme.2579

Golabbakhsh M, Wang X, MacDougall D, Farrell J, Landry T, Funnell WRJ, Adamson RBA (2023) Finite-element modelling based on optical coherence tomography and corresponding x-ray microCT data for three human middle ears. J Assoc Res Otolaryngol 24:339–363. https://doi.org/10.1007/s10162-023-00899-x

Goode RL, Ball G, Nishihara S (1993) Measurement of umbo vibration in human subjects-method and possible clinical applications. Am J Otol 14:247–251. https://doi.org/PMID: 8372921

Gundersen T, Høgmoen K (1976) Holographic vibration analysis of the ossicular chain. Acta Otolaryngol (Stockh) 82:16–25. https://doi.org/10.3109/00016487609120858

Hirabayashi M, Kurihara S, Ito R, Kurashina Y, Motegi M, Okano HJ, Yamamoto Y, Kojima H, Asakura T (2022) Combined analysis of finite element model and audiometry provides insights into the pathogenesis of conductive hearing loss. Front Bioeng Biotechnol 10:1541, 15 pp. https://doi.org/10.3389/fbioe.2022.967475

Huber A, Koike T, Wada H, Nandapalan V, Fisch U (2003) Fixation of the anterior mallear ligament: diagnosis and consequences for hearing results in stapes surgery. Ann Otol Rhinol Laryngol 112:348–355. https://doi.org/10.1177/000348940311200409

Kim W, Kim S, Huang S, Oghalai JS, Applegate BE (2019) Picometer scale vibrometry in the human middle ear using a surgical microscope based optical coherence tomography and vibrometry system. Biomed Opt Express 10:4395–4410. https://doi.org/10.1364/BOE.10.004395

Kirikae I (1960) The structure and function of the middle ear. Univ. of Tokyo Press, Tokyo

Kwacz M, Rymuza Z, Michałowski M, Wysocki J (2015) Elastic properties of the annular ligament of the human stapes--AFM measurement. J Assoc Res Otolaryngol 16:433–446. https://doi.org/10.1007/s10162-015-0525-9

MacDougall D, Morrison L, Morrison C, Morris DP, Bance M, Adamson RBA (2019) Optical coherence tomography doppler vibrometry measurement of stapes vibration in patients with stapes fixation and normal controls. Otol Neurotol 40:e349–e355. https://doi.org/10.1097/MAO.0000000000002193

Maftoon N, Funnell WRJ, Daniel SJ, Decraemer WF (2015) Finite-element modelling of the response of the gerbil middle ear to sound. J Assoc Res Otolaryngol JARO 16:547–567. https://doi.org/10.1007/s10162-015-0531-y

Masud SF (2020) Diagnosis of mechanical ear pathologies using structure-based modeling and machine learning techniques. Ph.D. thesis, Harvard University

Merchant GR (2014) Functional measurements of ear pathology in patients and cadaveric preparations. Ph.D. thesis, Massachusetts Institute of Technology

Merchant GR, Röösli C, Niesten MEF, Hamade MA, Lee DJ, McKinnon ML, Ulku CH, Rosowski JJ, Merchant SN, Nakajima HH (2015) Power reflectance as a screening tool

for the diagnosis of superior semicircular canal dehiscence. Otol Neurotol 36:172–177. https://doi.org/10.1097/MAO.0000000000000294

Motallebzadeh H, Maftoon N, Pitaro J, Funnell WRJ, Daniel SJ (2017) Finite-element modelling of the acoustic input admittance of the newborn ear canal and middle ear. J Assoc Res Otolaryngol JARO 18:25–48. https://doi.org/10.1007/s10162-016-0587-3

Park J, Carbajal EF, Chen X, Oghalai JS, Applegate BE (2014) Phase-sensitive optical coherence tomography using an Vernier-tuned distributed Bragg reflector swept laser in the mouse middle ear. Opt Lett 39:6233–6236. https://doi.org/10.1364/OL.39.006233

Ramier A, Rosowski JJ, Yun S-H (2018) Optical coherence tomography for imaging the middle and inner ears: A technical review. In: 13th Mechanics of Hearing Workshop: To the Ear and Back Again - Advances in Auditory Biophysics. St Catharines, Canada, p 020001

Rosowski JJ, Davis PJ, Merchant SN, Donahue KM, Coltrera MD (1990) Cadaver middle ears as models for living ears: comparisons of middle ear input immittance. Ann Otol Rhinol Laryngol 99:403–412. https://doi.org/10.1177/000348949009900515

Rosowski JJ, Nakajima HH, Hamade MA, Mahfoud L, Merchant GR, Halpin CF, Merchant SN (2012) Ear-canal reflectance, umbo velocity, and tympanometry in normal-hearing adults. Ear Hear 33:19–34. https://doi.org/10.1097/AUD.0b013e31822ccb76

Sackmann B, Eberhard P, Lauxmann M (2022) Parameter identification from normal and pathological middle ears using a tailored parameter identification algorithm. J Biomech Eng 144:. https://doi.org/10.1115/1.4052371

Sim JH, Huber AM, Häfliger M, de Trey LA, Eiber A, Röösli C (2013) Can an incomplete ossicular discontinuity be predicted by audiometric and clinical findings? Otol Neurotol 34:699–704. https://doi.org/10.1097/MAO.0b013e31828864a7

World Health Organization (2021) World report on hearing. https://www.who.int/publications-detail-redirect/9789240020481

Chapter 6. Discussion

6.1 Summary

In this work, for the first time, FE models of multiple human middle ears were built based on geometries obtained from microCT images and simulation results were compared with OCT vibration measurements in the same ears (Chapter 4). We created FE models of three cadaveric human middle ears based on microCT images and validated them against OCT vibration measurements at 500 Hz, 1 kHz and 2 kHz from the same ears. We conducted parameter sensitivity analyses and compared the results among the models and with the existing literature. The results of the parameter sensitivity analysis were similar across all three ears, except for one ear where the sensitivity to ISJ damping differed, presumably due to the stapes having a different orientation. Our parameter sensitivity analysis revealed that variations in the Young's modulus of the IMJ had small effects on the resonance frequency and displacement magnitude for frequencies up to 2 kHz. This suggests that, at least for frequencies up to 2 kHz, it may be unnecessary to include the IMJ in middle-ear models. A study of unrealistically low values of viscous cochlear damping increased the number of resonances seen on the TM, umbo and stapes, presumably corresponding to individual substructure resonances that are normally hidden.

The outputs of the FE models were compared to the experimental OCT measurements based on TM vibration maps and displacement magnitudes at several locations. The simulated TM vibration patterns were qualitatively similar to the OCT measurement data. At 2 kHz there were displacements with the appearance of travelling waves in both simulated and measured data. Our models had differences among themselves of up to a factor of 2 between individuals at lower frequencies and more at higher frequencies. The two models from the same individual had more similar frequency-response patterns at the umbo and stapes at frequencies of 1 to 8 kHz

compared to the third ear. They both had resonances at 1 kHz and another peak at around 1800 Hz but the frequency response of the third ear had no clear peaks and just descended gradually above 1 kHz. Frequency responses were computed for all three models at five locations (PPT, APT, umbo, incus and stapes). The displacement values of the models were closest to the OCT measurements at 500 Hz and the difference was greatest at 2 kHz. The umbo-to-incus magnitude ratio was always higher in the OCT results than in the models.

To model pathologies, we modified the parameters related to each pathological condition. We created large sets of synthetic data for models of normal ears and pathological ears (stapes fixation, IMJ disarticulation and ISJ disarticulation), with inter-ear variability incorporated by changing the model parameters randomly (Chapter 5). We used features extracted from simulated vibration magnitudes at different frequencies to classify the data into groups of normal ears and pathological ears. The changes due to the pathologies in our results were in agreement with those in experimental LDV measurements from normal subjects and patients. There was a decrease of umbo displacement magnitude at low frequencies compared to normal when the stapes was fixed, and an increase of umbo displacement magnitude below 1 kHz in both ISJ and IMJ disarticulation. A simple decision tree was designed based on the displacement magnitudes at the incus (as can be measured using OCT) and at the umbo. It could distinguish normal ears from IMJ disarticulation or stapes fixation with sensitivity and specificity of 1. It could distinguish between stapes fixation and IMJ disarticulation with a sensitivity of 0.904 and a specificity of 0.886 and between normal and ISJ disarticulation with a sensitivity of 0.787 and a specificity of 0.836. For a new test dataset, the performance was very similar: for the distinction of normal ears from IMJ disarticulation or stapes fixation we again had a sensitivity and specificity of 1; for the distinction between stapes fixation and IMJ disarticulation, the sensitivity was 0.900 and the

specificity was 0.889, and for the distinction between normal and ISJ disarticulation, the sensitivity was 0.784 and the specificity was 0.872. Partial pathologies were also simulated by considering a lower SAL Young's modulus and a higher IMJ Young's modulus than in the extreme conditions. In both cases, specificity of the decision tree decreased while sensitivity increased.

6.2 Future work

6.2.1 Introduction

We modelled the geometries of only three different ears. To make general claims about how the geometries and sizes of different parts of the middle ear will affect the model behaviour, it would be necessary to compare more samples from data of new patients and/or cadaver ears. Height and weight were not correlated with the size of the middle ear here. This is consistent with the conclusions of Arensburg et al. (1981), based on measurements in prehistoric, historic and recent populations, that there is 'a striking similarity and stability in their [ossicular] morphological and metric traits, contrary to other parts of their anatomy', including 'the width of the skull [and] the stature of the individual'.

In the rest of this section we will talk about possible further improvements in image segmentation, modelling and experimental measurements. We will also discuss how simulation and classification of pathologies can be improved.

6.2.2 Image segmentation

We manually performed image segmentation on stacks of microCT images by identifying contours of various structures. However, due to the complexity of the task with three ears, it was both challenging and time-consuming. There is a need for more efficient and accurate automatic or semi-automatic segmentation methods in the future. One potential solution is to train neural

networks for this purpose. However, the image quality of conventional microCT images is not good enough to show soft tissues well and it will affect the feasibility of image segmentation methods, unless we use some alternative image modalities such as microCT with staining (De Greef et al. 2015), nanoCT (Feizollah 2019) or synchrotron radiation phase-contrast imaging (Elfarnawany et al. 2017), which can be used in cadaver ear measurements for research. For *in vivo* clinical measurements, microCT images would not be available due to the size of the human head and the radiation risks, but non-rigid image-registration techniques (Hill et al. 2001) could be used to register CT and OCT patient measurements with the microCT images corresponding to existing middle-ear models (e.g., our FE models). The existing models could then be warped to fit the new patient data.

6.2.3 Model improvement

There are possible ways to improve the current FE models. For example, TM thickness has a great effect on the displacement results (e.g., Gan et al. 2007; Maftoon et al. 2015; De Greef et al. 2017). Although we considered a uniform thickness for the PT, there are FE models that consider a nonuniform thickness (e.g., Maftoon et al. 2015; Motallebzadeh et al. 2017). Also, we considered the TM material to be isotropic, but, because the TM contains layers of radially and circumferentially oriented collagen fibres, it is treated as an orthotropic material in some models (e.g., Funnell and Laszlo 1978; Gan et al. 2007; O'Connor et al. 2017). (We did not consider the shear modulus explicitly, as O'Connor et al. did, because it is directly determined by the Young's modulus and Poisson ratio for isotropic materials.)

Fay (2006) incorporated a detailed representation of the fibrous layers and reported that the resulting asymmetric TM achieves optimal transmission at high frequencies by creating a multitude of resonances. In Tuck-Lee et al. (2008), the confocal microscopic observations of cat

eardrum thickness of Kuypers et al. (2006) were projected onto radial spline geometries and the microstructural observations by Lim (1968) were used to construct the radial and circumferential fibrous layers of the TM.

We did not model the AML and the PIL. Instead, we used very stiff springs attached to a node at each of those ligaments' locations, effectively fixing those nodes for translation but not for rotation. However, at high frequencies the 3D vibration is complex and it is important to consider more degrees of freedom for the ligaments (Decraemer and Khanna 2004). Modelling with functional springs would be possible but it is difficult to estimate reasonable stiffnesses for the springs, especially for the rotational stiffness about the axis of rotation. Modelling the ligaments with 3D elements, even if they are only approximate shapes like cylinders or hexahedra (since the actual shapes are difficult to image) will provide more realistic translational and rotational behaviour for the ligaments (Gan et al. 2007; Motallebzadeh et al. 2017; De Greef et al. 2017).

Different boundary conditions, including simply supported or fully clamped, or with springs as used by Wada and Kobayashi (1990), have been considered for the TM. Van Wijhe (2001) modelled the fibrocartilaginous ring with a reasonable Young's modulus and concluded that it was effectively rigid, suggesting that a simply-supported or fully-clamped boundary condition should be applied on the boundary between the TM and the ring. Gea et al. (2010) and O'Connor et al. (2017) further explored the question experimentally for the static case.

We have not modelled the middle-ear air cavity, but it has an effect on the input admittance of the middle ear as discussed in Chapter 2 and it could be considered in future to create a more realistic FE model for situations where the cavity is closed.

Our FE models exhibit a faster drop in the frequency response at higher frequencies than is seen in the experimental data, which is probably because of these simplifications that we have made.

As our study of unrealistically low values of viscous cochlear damping increased the number of resonances seen at the TM, umbo and stapes, in the future we could investigate which individual substructure resonances are hidden. The fact that ear 2016-1 had no peaks in the frequency response, while ears 2017-1 and 2017-2 did have peaks, could also be investigated.

6.2.4 Experimental work

We have only considered modelling and classification of stapes fixation and ossicular discontinuity so far, but it is possible to model other pathological conditions such as malleus fixation, incus head fixation and superior semi-circular canal dehiscence, and further research can be conducted to investigate how to discriminate among these conditions. Malleus fixation and incus head fixation have been investigated in patient measurements by Rosowski (2008) and in cadaveric human temporal-bone preparations that simulate these disorders by Nakajima (2005). They measured and compared the results with normal ears. More recently, superior semi-circular canal dehiscence was measured in patients (Nakajima et al. 2012). Merchant (2014) used a decision tree and Masud (2020) used the random-forest method to detect superior semi-circular canal dehiscence based on measurements in patients and cadaver ears.

Our consideration of joint disarticulation and stapes fixation was primarily based on a preclinical study by Adamson's group at Dalhousie University (personal communication) where they alter cadaver ears to simulate pathologies. For ISJ disarticulation, they use a scalpel to cut through the incudostapedial joint via the facial recess. Once the joint is completely separated, the two crura of the stapes are cut and the stapes superstructure is removed from the ear so that the incus is fully disconnected from the stapes. For IMJ disarticulation, they use a scalpel to cut through the

IMJ and the PIL via a posterior atticotomy. The incus is removed via the facial recess. For stapes fixation, glass ionomer luting cement is placed in the oval window niche through the facial recess to fully cover the stapes footplate while leaving the crura of the stapes exposed. The cement is allowed to cure for a minimum of 5 minutes.

It is challenging to determine appropriate stiffness values for those structures in ears with hearing disorders. The experimental measurements of mechanical properties of the structures could be done on cadaver ears with diagnosed pathological conditions. However, cadaver ears are available only in limited numbers and those with both specific pathologies and well-defined diagnoses are even rarer.

In this thesis, we employed a decision tree and a limited number of features, namely the vibration magnitudes at the umbo and the incus, at a few different frequencies, to classify normal and pathological ears. However, future studies could explore other classification methods, such as random forests, or other supervised learning methods such as support vector machines (SVM) and k-nearest neighbours (kNN) (Hastie et al. 2009). SVM is often less computationally costly than kNN and is easier to interpret, but it can determine only a limited set of patterns, while kNN can find very complex patterns (Bzdok et al. 2018).

Yet another approach is simulation-based inference using a neural network (Cranmer et al. 2020). After being trained on simulated data, and possibly retrained on measured data, the neural network can be used to infer probability distributions of model parameter values based on new data. This method has been used for training a neural network for differential diagnosis of conductive hearing loss (Motallebzadeh 2022; Sackmann et al. 2022) and could be used for OCT data.

In future studies, OCT measurements could be improved so that they provide displacements at the stapes. This might be helpful in distinguishing ISJ disarticulation from normal. In a study by (Chang et al. 2013) on cadaver chinchillas, they were able to classify ISJ disarticulation from normal using OCT measurements at the umbo, incus and stapes.

In future studies of pathological conditions, one could include medical history, data from clinical tests such as the air-bone gap (ABG), or hearing improvement following the Valsalva manoeuvre (Sim et al. 2013), along with the vibration measurements. Synthetic clinical data could be generated to supplement the synthetic vibration data, as Hirabayashi et al. (2022) did for ABG data.

6.3 Significance

This is the first time that the responses of multiple human middle ears to sound have been validated against Doppler OCT vibration measurements from the same ears, and the first time that the classification of normal and pathological models based on umbo and incus displacement magnitudes has been studied. The results of our study provide insight into the features present in OCT measurements and their possible diagnostic applications. Our results suggest that the vibration measurements within the middle ear that can be provided by OCT (e.g., at the incus) may be very valuable for diagnosis, and that umbo and incus vibrations should be measured at both low and high frequencies (e.g., 500 Hz and 3 kHz) in order to distinguish among the disorders considered here.

Using OCT can help to find a non-invasive way to diagnose hearing disorders and eventually in actual human patients. Our results on the classification of simulated pathological middle ears suggest that the vibration measurements within the middle ear that can be provided by OCT can provide a diagnostic method that is less invasive, less costly and more accurate than using

immittance or LDV measurements. This could help patients with conductive hearing loss to be diagnosed earlier and get appropriate and timely treatment. It could help clinicians by making them more prepared before the surgery, and could also help in monitoring patients after surgery.

References

Aibara R, Welsh JT, Puria S, Goode RL (2001) Human middle-ear sound transfer function and cochlear input impedance. Hear Res 152:100–109. https://doi.org/10.1016/S0378-5955(00)00240-9

Anson BJ, Donaldson JA (1981) Surgical anatomy of the temporal bone, 3rd edn. Saunders, Philadelphia

Applegate BE, Shelton RL, Gao SS, Oghalai JS (2011) Imaging high-frequency periodic motion in the mouse ear with coherently interleaved optical coherence tomography. Opt Lett 36:4716. https://doi.org/10.1364/OL.36.004716

Arensburg B, Harell M, Nathan H (1981) The human middle ear ossicles: Morphometry, and taxonomic implications. Journal of Human Evolution 10:199–205. https://doi.org/10.1016/S0047-2484(81)80018-8

Beer HJ, Bornitz M, Hardtke HJ, Schmidt R, Hofmann G, Vogel U, Zahnert T, Hüttenbrink KB (1999) Modelling of components of the human middle ear and simulation of their dynamic behaviour. Audiol Neurootol 4:156–162. https://doi.org/10.1159/000013835

Békésy G (1941) Über die Messung der Schwingungsamplitude der Gehörknöcheln mittels einer kapazitiven Sonde

Bonesi M, Minneman MP, Ensher J, Zabihian B, Sattmann H, Boschert P, Hoover E, Leitgeb RA, Crawford M, Drexler W (2014) Akinetic all-semiconductor programmable swept-source at 1550 nm and 1310 nm with centimeters coherence length. Opt Express 22:2632. https://doi.org/10.1364/OE.22.002632

Burkhardt A, Kirsten L, Bornitz M, Zahnert T, Koch E (2014) Investigation of the human tympanic membrane oscillation ex vivo by Doppler optical coherence tomography. J Biophotonics 7:434–441. https://doi.org/10.1002/jbio.201200186

Buytaert JAN, Dirckx JJJ (2009) Tomographic imaging of macroscopic biomedical objects in high resolution and three dimensions using orthogonal-plane fluorescence optical sectioning. Appl Opt, AO 48:941–948. https://doi.org/10.1364/AO.48.000941

Bzdok D, Krzywinski M, Altman N (2018) Machine learning: supervised methods. Nature Methods 15:5–6. https://doi.org/10.1038/nmeth.4551

Chang EW, Cheng JT, Röösli C, Kobler JB, Rosowski JJ, Yun SH (2013) Simultaneous 3D imaging of sound-induced motions of the tympanic membrane and middle ear ossicles. Hear Res 304:49–56. https://doi.org/10.1016/j.heares.2013.06.006

Cheng JT, Aarnisalo AA, Harrington E, Hernandez-Montes MDS, Furlong C, Merchant SN, Rosowski JJ (2010) Motion of the surface of the human tympanic membrane measured with stroboscopic holography. Hear Res 263:66–77. https://doi.org/10.1016/j.heares.2009.12.024

Cheng JT, Ghanad I, Remenschneider A, Rosowski JJ (2021) The onset of nonlinear growth of middle-ear responses to high intensity sounds. Hear Res 405:108242, 13 pp. https://doi.org/10.1016/j.heares.2021.108242

Cranmer K, Brehmer J, Louppe G (2020) The frontier of simulation-based inference. Proceedings of the National Academy of Sciences 117:30055–30062. https://doi.org/10.1073/pnas.1912789117

Daniel SJ, Funnell WRJ, Zeitouni AG, Schloss MD, Rappaport J (2001) Clinical applications of a finite-element model of the human middle ear. J Otolaryngol 30:340–346

De Greef D, Buytaert JAN, Aerts JRM, Van Hoorebeke L, Dierick M, Dirckx J (2015) Details of human middle ear morphology based on micro-CT imaging of phosphotungstic acid stained samples. J Morphol 276:1025–1046. https://doi.org/10.1002/jmor.20392

De Greef D, Pires F, Dirckx JJJ (2017) Effects of model definitions and parameter values in finite element modeling of human middle ear mechanics. Hear Res 344:195–206. https://doi.org/10.1016/j.heares.2016.11.011

Decraemer WF, Dirckx JJJ, Funnell WRJ (2003) Three-dimensional modelling of the middle-ear ossicular chain using a commercial high-resolution x-ray ct scanner. JARO 4:250–263. https://doi.org/10.1007/s10162-002-3030-x

Decraemer WF, Khanna SM (2004) Measurement, visualization and quantitative analysis of complete three-dimensional kinematical data sets of human and cat middle ear. In: Middle Ear Mechanics in Research and Otology. pp 3–10

Djalilian HR, Ridgway J, Tam M, Sepehr A, Chen Z, Wong BJF (2008) Imaging the human tympanic membrane using optical coherence tomography in vivo: Otology & Neurotology 29:1091–1094. https://doi.org/10.1097/MAO.0b013e31818a08ce

Eiber A, Freitag H-G, Hocke T (2000) On the relationship between multifrequency tympanogram pattern and the dynamic behavior of the middle ear

Elfarnawany M, Rohani SA, Ghomashchi S, Allen DG, Zhu N, Agrawal SK, Ladak HM (2017) Improved middle-ear soft-tissue visualization using synchrotron radiation phase-contrast imaging. Hear Res 354:1–8. https://doi.org/10.1016/j.heares.2017.08.001

Farrell JD, Wang J, MacDougall D, Yang X, Brewer K, Couvreur F, Shoman N, Morris DP, Adamson RBA (2023) Geometrically accurate real-time volumetric visualization of the middle ear using optical coherence tomography. Biomed Opt Express 14:3152–3171. https://doi.org/10.1364/BOE.488845

Fay JP, Puria S, Steele CR (2006) The discordant eardrum. Proc Natl Acad Sci USA 103:19743–19748. https://doi.org/10.1073/pnas.0603898104

Feizollah S (2019) Microstructure and displacements of the gerbil incudostapedial joint under static pressures. Master’s, McGill University

Funnell WR (1996) Low-frequency coupling between eardrum and manubrium in a finite-element model. JASA 99:3036–3043. https://doi.org/10.1121/1.414875

Funnell WRJ (1983) On the undamped natural frequencies and mode shapes of a finite-element model of the cat eardrum. JASA 73:1657–1661. https://doi.org/10.1121/1.389386

Funnell WRJ, Decraemer WF (1996) On the incorporation of moiré shape measurements in finite-element models of the cat eardrum. JASA 100:925–932. https://doi.org/10.1121/1.416252

Funnell WRJ, Khanna SM, Decraemer WF (1992) On the degree of rigidity of the manubrium in a finite-element model of the cat eardrum. JASA 91:2082–2090. https://doi.org/10.1121/1.403694

Funnell WRJ, Laszlo CA (1978) Modeling of the cat eardrum as a thin shell using the finite-element method. JASA 63:1461–1467. https://doi.org/10.1121/1.381892

Funnell WRJ, Maftoon N, Decraemer WF (2012) Mechanics and modelling for the middle ear

Funnell WRJ, Phelan (1981) Finite-element modeling of the middle-ear ossicles. JASA 69:S14–S14. https://doi.org/10.1121/1.386393

Funnell WRobertJ, Heng Siah T, McKee MD, Daniel SJ, Decraemer WF (2005) On the Coupling Between the Incus and the Stapes in the Cat. J Assoc Res Otolaryngol 6:9–18. https://doi.org/10.1007/s10162-004-5016-3

Gan RZ, Feng B, Sun Q (2004) Three-dimensional finite element modeling of human ear for sound transmission. Ann Biomed Eng 32:847–859. https://doi.org/10.1023/B:ABME.0000030260.22737.53

Gan RZ, Reeves BP, Wang X (2007) Modeling of sound transmission from ear canal to cochlea. Ann Biomed Eng 35:2180–2195. https://doi.org/10.1007/s10439-007-9366-y

Gea SLR, Decraemer WF, Funnell WRJ, Dirckx JJJ, Maier H (2010) Tympanic membrane boundary deformations derived from static displacements observed with computerized tomography in human and gerbil. J Assoc Res Otolaryngol 11:1–17. https://doi.org/10.1007/s10162-009-0192-9

Gladiné K, Dirckx JJJ (2018) Average middle ear frequency response curves with preservation of curve morphology characteristics. Hear Res 363:39–48. https://doi.org/10.1016/j.heares.2018.02.005

Graham MD, Reams C, Perkins R (1978) Human tympanic membrane--malleus attachment. Preliminary study. Ann Otol Rhinol Laryngol 87:426–431. https://doi.org/10.1177/000348947808700326

Gulya AJ, Schuknecht HF (1994) Anatomy of the temporal bone with surgical implications, second edition. Taylor & Francis

Gyo K, Aritomo H, Goode RL (1987) Measurement of the ossicular vibration ratio in human temporal bones by use of a video measuring system. Acta Otolaryngol 103:87–95. https://doi.org/10.3109/00016488709134702

Hastie T, Tibshirani R, Friedman J (2009) The elements of statistical learning. Springer, New York, NY

Heermann R, Hauger C, Issing PR, Lenarz T (2002) Erste anwendungen der optischen kohärenztomographie (OCT) in der mittelohrchirurgie. Laryngo- Rhino- Otol 81:400–405. https://doi.org/10.1055/s-2002-32213

Henson MM, Henson OW, Gewalt SL, Wilson JL, Johnson GA (1994) Imaging the cochlea by magnetic resonance microscopy. Hear Res 75:75–80. https://doi.org/10.1016/0378-5955(94)90058-2

Hill DLG, Batchelor PG, Holden M, Hawkes DJ (2001) Medical image registration

Hirabayashi M, Kurihara S, Ito R, Kurashina Y, Motegi M, Okano HJ, Yamamoto Y, Kojima H, Asakura T (2022) Combined analysis of finite element model and audiometry provides insights into the pathogenesis of conductive hearing loss. Front Bioeng Biotechnol 10:1541, 15 pp. https://doi.org/10.3389/fbioe.2022.967475

Huber AM, Schwab C, Linder T, Stoeckli SJ, Ferrazzini M, Dillier N, Fisch U (2001) Evaluation of eardrum laser doppler interferometry as a diagnostic tool. Laryngoscope 111:501–507. https://doi.org/10.1097/00005537-200103000-00022

Hubler Z, Shemonski ND, Shelton RL, Monroy GL, Nolan RM, Boppart SA (2015) Real-time automated thickness measurement of the in vivo human tympanic membrane using optical coherence tomography. Quant Imaging Med Surg 5:69–77. https://doi.org/10.3978/j.issn.2223-4292.2014.11.32

Huttenbrink KB, Hudde H (1994) First results of analysis of sound transmission through the reconstructed middle ear with an inner ear hydrophone. HNO 42:49–57

Jung W, Kim J, Jeon M, Chaney EJ, Stewart CN, Boppart SA (2011) Handheld optical coherence tomography scanner for primary care diagnostics. IEEE Trans Biomed Eng 58:741–744. https://doi.org/10.1109/TBME.2010.2096816

Just T, Lankenau E, Hüttmann G, Pau HW (2009) Optische kohärenztomographie in der mittelohrchirurgie. HNO 57:421–427. https://doi.org/10.1007/s00106-009-1907-2

Kessel J (1874) On the influence of the middle-ear muscles on the displacements and vibrations of the eardrum in the cadaver ear. Arch OhrenhLk 8:80–92

Kirikae I (1960) The structure and function of the middle ear. Univ. of Tokyo Press, Tokyo

Kirsten L, Baumgärtner S, Erkkilä MT, Golde J, Kemper M, Stoppe T, Bornitz M, Neudert M, Zahnert T, Koch E (2016) Doppler optical coherence tomography as a promising tool for

detecting fluid in the human middle ear. Current Directions in Biomedical Engineering 2:443–447. https://doi.org/10.1515/cdbme-2016-0098

Kirsten L, Burkhardt A, Golde J, Walther J, Walther J, Stoppe T, Bornitz M, Kemper M, Zahnert T, Koch E (2015) Imaging the tympanic membrane oscillation ex vivo with Doppler optical coherence tomography during simulated Eustachian catarrh. In: Optical Coherence Imaging Techniques and Imaging in Scattering Media (2015), paper 95410R. Optical Society of America, p 95410R

Kirsten L, Schindler M, Morgenstern J, Erkkilä MT, Golde J, Walther J, Rottmann P, Kemper M, Bornitz M, Neudert M, … Koch E (2019) Endoscopic optical coherence tomography with wide field-of-view for the morphological and functional assessment of the human tympanic membrane. J Biomed Opt 24:1. https://doi.org/10.1117/1.JBO.24.3.031017

Kobrak HG (1948) Construction material of the sound conduction system of the human ear. JASA 20:125–130. https://doi.org/10.1121/1.1906353

Kose O, Funnell WRJ, Daniel SJ (2020) Vibration measurements of the gerbil eardrum under quasi-static pressure steps. J Assoc Res Otolaryngol 21:287–302. https://doi.org/10.1007/s10162-020-00763-2

Kuypers LC, Decraemer WF, Dirckx JJJ (2006) Thickness distribution of fresh and preserved human eardrums measured with confocal microscopy. Otol Neurotol 27:256–264. https://doi.org/10.1097/01.mao.0000187044.73791.92

Lim DJ (1968) Tympanic membrane. Electron microscopic observation. I: pars tensa. Acta Otolaryngol 66:181–198. https://doi.org/10.3109/00016486809126286

MacDougall D, Farrell J, Brown J, Bance M, Adamson R (2016) Long-range, wide-field swept-source optical coherence tomography with GPU accelerated digital lock-in Doppler vibrography for real-time, in vivo middle ear diagnostics. Biomed Opt Express, BOE 7:4621–4635. https://doi.org/10.1364/BOE.7.004621

MacDougall D, Morrison L, Morrison C, Morris DP, Bance M, Adamson RBA (2019) Optical coherence tomography doppler vibrometry measurement of stapes vibration in patients with stapes fixation and normal controls. Otol Neurotol 40:e349–e355. https://doi.org/10.1097/MAO.0000000000002193

Maftoon N, Funnell WRJ, Daniel SJ, Decraemer WF (2015) Finite-element modelling of the response of the gerbil middle ear to sound. J Assoc Res Otolaryngol 16:547–567. https://doi.org/10.1007/s10162-015-0531-y

Masud SF (2020) Diagnosis of mechanical ear pathologies using structure-based modeling and machine learning techniques. Ph.D. thesis, Harvard University

Merchant GR (2014) Functional measurements of ear pathology in patients and cadaveric preparations. Ph.D. thesis, Massachusetts Institute of Technology

Merchant SN, Ravicz ME, Rosowski JJ (1996) Acoustic input impedance of the stapes and cochlea in human temporal bones. Hear Res 97:30–45

Mikhael CS, Funnell WRJ, Bance M (2004) Middle-ear finite-element modelling with realistic geometry and apriori material- property estimates. Proc 28th Ann Conf Can Med Biol Eng Soc

Monroy GL, Fitzgerald ST, Locke A, Won J, Jr DRS, Ho A, Zaki FR, Choi H, Chaney EJ, Werkhaven JA, … Boppart SA (2023) Integrated Raman spectroscopy and optical coherence tomography system for characterizing otitis media. In: Imaging, Therapeutics, and Advanced Technology in Head and Neck Surgery and Otolaryngology 2023. SPIE, p 1235404

Monroy GL, Fitzgerald ST, Locke A, Won J, Spillman DR, Ho A, Zaki FR, Choi H, Chaney EJ, Werkhaven JA (2022) Multimodal handheld probe for characterizing otitis media—integrating Raman spectroscopy and optical coherence tomography. Front Photon 3:929574

Monroy GL, Shelton RL, Nolan RM, Nguyen CT, Novak MA, Hill MC, McCormick DT, Boppart SA (2015) Noninvasive depth-resolved optical measurements of the tympanic membrane and middle ear for differentiating otitis media. Laryngoscope 125:E276–E282. https://doi.org/10.1002/lary.25141

Motallebzadeh H (2022) Training a machine-learning differential diagnostic tool for conductive hearing loss using mechanistic models. In: MEMRO 2022 : 9th international symposium on middle ear mechanics in research and otology, Boulder, CO, USA

Motallebzadeh H, Maftoon N, Pitaro J, Funnell WRJ, Daniel SJ (2017) Finite-element modelling of the acoustic input admittance of the newborn ear canal and middle ear. J Assoc Res Otolaryngol 18:25–48. https://doi.org/10.1007/s10162-016-0587-3

Nakajima HH, Pisano DV, Roosli C, Hamade MA, Merchant GR, Mahfoud L, Halpin CF, Rosowski JJ, Merchant SN (2012) Comparison of ear-canal reflectance and umbo velocity in patients with conductive hearing loss: a preliminary study. Ear Hear 33:35–43. https://doi.org/10.1097/AUD.0b013e31822ccba0

Nakajima HH, Ravicz ME, Rosowski JJ, Peake WT, Merchant SN (2005) Experimental and clinical studies of malleus fixation. Laryngoscope 115:147–154. https://doi.org/10.1097/01.mlg.0000150692.23506.b7

O'Connor KN, Cai H, Puria S (2017) The effects of varying tympanic-membrane material properties on human middle-ear sound transmission in a three-dimensional finite-element model. JASA 142:2836. https://doi.org/10.1121/1.5008741

Ohashi M, Ide S, Kimitsuki T, Komune S, Suganuma T (2006) Three-dimensional regular arrangement of the annular ligament of the rat stapediovestibular joint. Hear Res 213:11–16. https://doi.org/10.1016/j.heares.2005.11.007

Park J, Carbajal EF, Chen X, Oghalai JS, Applegate BE (2014) Phase-sensitive optical coherence tomography using an Vernier-tuned distributed Bragg reflector swept laser in the mouse middle ear. Opt Lett 39:6233–6236. https://doi.org/10.1364/OL.39.006233

Pitris C, Saunders KT, Fujimoto JG, Brezinski ME (2001) High-resolution imaging of the middle ear with optical coherence tomography: a feasibility study. AOHNS 127:637–642. https://doi.org/10.1001/archotol.127.6.637

Prendergast PJ, Ferris P, Rice HJ, Blayney AW (1999) Vibro-acoustic modelling of the outer and middle ear using the finite-element method. Audiol Neurootol 4:185–191. https://doi.org/10.1159/000013839

Puria S, Peake WT, Rosowski JJ (1997) Sound-pressure measurements in the cochlear vestibule of human-cadaver ears. JASA 101:2754–2770. https://doi.org/10.1121/1.418563

Rabbitt RD, Holmes MH (1986) A fibrous dynamic continuum model of the tympanic membrane. JASA 80:1716–1728. https://doi.org/10.1121/1.394284

Ramier A, Rosowski JJ, Yun S-H (2018) Optical coherence tomography for imaging the middle and inner ears: A technical review. In: 13th Mechanics of Hearing Workshop: To the Ear and Back Again - Advances in Auditory Biophysics. St Catharines, Canada, p 020001

Rosowski J, Cheng J, Merchant S, Harrington E, Furlong C (2011) New data on the motion of the normal and reconstructed tympanic membrane. Otol Neurotol 32:1559–1567. https://doi.org/10.1097/MAO.0b013e31822e94f3

Rosowski JJ, Nakajima HH, Merchant SN (2008) Clinical utility of laser-Doppler vibrometer measurements in live normal and pathologic human ears. Ear Hear 29:3–19. https://doi.org/10.1097/AUD.0b013e31815d63a5

Sackmann B, Lauxmann M, Burovikhin D (2022) Model-based hearing diagnosis based on Monte-Carlo parameter estimation and artificial neural networks. In: MEMRO 2022 : 9th international symposium on middle ear mechanics in research and otology, 21-25 June 2022, Boulder, CO, USA. p 38

Sim JH, Huber AM, Häfliger M, de Trey LA, Eiber A, Röösli C (2013) Can an incomplete ossicular discontinuity be predicted by audiometric and clinical findings? Otol Neurotol 34:699–704. https://doi.org/10.1097/MAO.0b013e31828864a7

Stepp CE, Voss SE (2005) Acoustics of the human middle-ear air space. JASA 118:861–871. https://doi.org/10.1121/1.1974730

Subhash HM, Jacques SL, Nguyen-Huynh AT, Nuttall AL, Wang RK, Choudhury N (2012) Feasibility of spectral-domain phase-sensitive optical coherence tomography for middle ear vibrometry. JBO 17:060505. https://doi.org/10.1117/1.JBO.17.6.060505

Tang H, Psota P, Rosowski JJ, Furlong C, Cheng JT (2021) Analyses of the tympanic membrane impulse response measured with high-speed holography. Hear Res 410:108335. https://doi.org/10.1016/j.heares.2021.108335

Thompson AC, Llacer J, Campbell Finman L, Hughes EB, Otis JN, Wilson S, Zeman HD (1984) Computed tomography using synchrotron radiation. Nucl Instrum Methods Phys Res 222:319–323. https://doi.org/10.1016/0167-5087(84)90550-7

Thompson CW, Rohani SA, Dirckx JJ, Agrawal SK, Ladak HM (2023) Finite element modelling of the human middle ear using synchrotron-radiation phase-contrast imaging. Comput Biol Med 157:106747. https://doi.org/10.1016/j.compbiomed.2023.106747

Tonndorf J, Khanna SM (1972) Tympanic-membrane vibrations in human cadaver ears studied by time-averaged holography. JASA 52:1221–1233. https://doi.org/10.1121/1.1913236

Tuck-Lee JP, Pinsky PM, Steele CR, Puria S (2008) Finite element modeling of acousto-mechanical coupling in the cat middle ear. JASA 124:348–362. https://doi.org/10.1121/1.2912438

Van der Jeught S, Dirckx JJJ, Aerts JRM, Bradu A, Podoleanu AG, Buytaert JAN (2013) Full-field thickness distribution of human tympanic membrane obtained with optical coherence tomography. JARO 14:483–494. https://doi.org/10.1007/s10162-013-0394-z

Van Wijhe RG (2001) A finite element model of the middle ear of the moustached bat. M.Eng thesis, McGill University

Van Wijhe RG, Funnell (2000) Development of a finite-element model of the middle ear of the moustached bat. Halifax, pp 20–21

Vogel U (1999) New approach for 3D imaging and geometry modeling of the human inner ear. ORL J Otorhinolaryngol Relat Spec 61:259–267. https://doi.org/10.1159/000027683

Vogel U, Schmitt T (1998) 3D visualization of middle ear structures. In: Medical Imaging 1998: Image Display. SPIE, pp 141–151

Voie (2002) Imaging the intact guinea pig tympanic bulla by orthogonal-plane fluorescence optical sectioning microscopy. Hear Res 171:119–128

Voie, Spelman (1995) Three-dimensional reconstruction of the cochlea from two-dimensional images of optical sections. Comput Med Imaging Graph 19:377–384

Wada H, Kobayashi T (1990) Dynamical behavior of middle ear: Theoretical study corresponding to measurement results obtained by a newly developed measuring apparatus. JASA 87:237–245. https://doi.org/10.1121/1.399290

Wada H, Metoki T, Kobayashi T (1992) Analysis of dynamic behavior of human middle ear using a finite-element method. JASA 92:3157–3168. https://doi.org/10.1121/1.404211

Wang X (2019) Finite-element modelling of the human middle ear based on X-ray micro-computed tomography and Doppler optical coherence tomography in the same ear. Master’s, McGill University

Wang X, Gan RZ (2018) Surface motion of tympanic membrane in a chinchilla model of acute otitis media. J Assoc Res Otolaryngol 19:619–635. https://doi.org/10.1007/s10162-018-00683-2

Wever EG, Lawrence M (1954) Physiological Acoustics. Princeton University Press

Whittemore KR, Merchant SN, Poon BB, Rosowski JJ (2004) A normative study of tympanic membrane motion in humans using a laser Doppler vibrometer (LDV). Hear Res 187:85–104. https://doi.org/10.1016/s0378-5955(03)00332-0

Wolff D, Bellucci RJ (1956) The human ossicular ligaments. Ann Otol Rhinol Laryngol 65:895–910. https://doi.org/10.1177/000348945606500401

Won J, Monroy GL, Dsouza RI, Spillman DR, McJunkin J, Porter RG, Shi J, Aksamitiene E, Sherwood M, Stiger L, Boppart SA (2021) Handheld briefcase optical coherence tomography with real-time machine learning classifier for middle ear infections. Biosensors (Basel) 11:143. https://doi.org/10.3390/bios11050143

World Health Organization (2021) World report on hearing. Geneva: World Health Organization; Accessed 23 Dec 2022

Zhao F, Koike T, Wang J, Sienz H, Meredith R (2009) Finite element analysis of the middle ear transfer functions and related pathologies. Med Eng Phys 31:907–916. https://doi.org/10.1016/j.medengphy.2009.06.009

Zienkiewicz OC, Taylor RL, Zhu JZ (eds) (2013) The finite element method: its basis and fundamentals. In: The Finite Element Method: its Basis and Fundamentals (Seventh Edition). Butterworth-Heinemann, Oxford, p iii